SPIN-POLARIZED CURRENT DRIVEN MAGNETIZATION DYNAMICS AND APPLICATIONS IN SPIN VALVE PILLARS

A thesis submitted
in partial fulfillment for the degree of

Doctor of Philosophy

by

SANID C

Department of Physics
INDIAN INSTITUTE OF SPACE SCIENCE AND TECHNOLOGY
Thiruvananthapuram - 695547

MARCH 2014

CERTIFICATE

This thesis titled **Spin-polarized Current Driven Magnetization Dynamics and Applications in Spin Valve Pillars** submitted by **Mr. Sanid C.**, for the award of the degree of **Doctor of Philosophy** in Physical Science to the Indian Institute of Space Science and Technology, Thiruvananthapuram is a record of bona fide research work carried out by him under my guidance and supervision.

The results presented in this thesis have not been submitted to any other university or institution for the award of any other degree or diploma.

Dr. S. Murugesh,
Associate professor,
Department of Physics,
Indian Institute of Space Science and Technology,
Thiruvananthapuram.

Place: Thiruvananthapuram
Date: 31 March, 2014

DECLARATION

I declare that this thesis titled **Spin-polarized Current Driven Magnetization Dynamics and Applications in Spin Valve Pillars** submitted in fulfilment of the Degree of **Doctor of Philosophy** is a record of original work carried out by me under the supervision of **Dr. S. Murugesh**, and has not formed the basis for the award of any degree, diploma, associateship, fellowship or other titles in this or any other Institution or University of higher learning. In keeping with the ethical practice in reporting scientific information, due acknowledgements have been made wherever the findings of others have been cited.

Sanid C
SC10D004

Place: Thiruvananthapuram
Date: 31 March, 2014

ACKNOWLEDGEMENTS

I take this opportunity to express my sincere gratitude to my research supervisor, Dr. S. Murugesh, although a few words cannot do justice to the pivotal role he has had in my life as a graduate student. I have greatly benefited from his in-depth subject knowledge and the free yet targeted research atmosphere he has created. I also thank him for sharing his office space with me during my four year stint at IIST. I thank the members of my doctoral committee, Dr. C. S. Narayanamurthy, Dr. Sreedhar B. Dutta, Dr. R. Sankaranarayanan, Dr. Anand Narayanan, and Dr. C. Sudheesh, for their guidance and support during annual reviews. I thank Dr. C. S. Narayanamurthy, the Head of the Department of Physics and all other faculty members of the Physics department for creating such a stimulating environment conducive for fundamental research. It is my pleasure to thank the Director, Dr. K. S. Dasgupta, the former Dean R&D, Dr. V. Adimurthy, and the present Dean R&D, Dr. Thomas Kurian, specifically for their support during my foreign travel and generally for providing a research friendly atmosphere at IIST. I thank ISRO/IIST for financially supporting me during my Ph.D candidature with a generous fellowship.

I express my overwhelming gratitude to my parents, my elder sister and my younger sister for their love and support. I thank all my close friends and trek companions outside the institute for sparing me from the abyss of boredom. Each trek rejuvenated my spirit to delve deeper into the scientific problem at hand. I also thank my colleagues and friends at IIST for their timely help and valuable discussions. Last, but not least, I thank my partner, Deepthi V. C., for putting up with my idiosyncrasies, for supporting me at each step and for being the wonderful person she is. Being an animator by profession, she did help me in creating many graphic illustrations included in the thesis and I thank her for that as well.

ABSTRACT

Moore's law, the holy grail of current semiconductor industry, anticipates an approximate doubling of transistors on integrated circuits every two years. This downscaling of IC size with concomitant increase in computational power seemed saturated about a decade ago, due to the individual transistor size approaching the size of an atom. This modifies the laws of semiconductor physics as we know it, bringing in tangible quantum mechanical effects. One of the road ahead for the semiconductor industry is to take into consideration the *spin* of the electron along with its electric charge in designing novel, energy-efficient and non-volatile memory devices and much more. The contemporary area of technology aimed at accomplishing all these came to be known as *spintronics*.

In this thesis we approach the device physics of some of the highly sought after spintronic devices using a *dynamical systems* approach, which models these devices at a semi-classical level and study them using a dynamical equation (The Landau-Lifhsitz-Gilbert-Slonczewski equation). We specifically focus on the current driven dynamics in the spin valve pillar devices, which are the basic GMR cells to be transformed into a memory cell, a logic gate, or a nano-oscillator. We derive significant results on two fronts which are potential interests to both academia and industry— magneto-logic gates, and spin-torque nano-oscillators.

We propose model magneto-logic NOR and NAND gates using a spin valve pillar, wherein the logical operation is induced by spin-polarized currents which also form the logical inputs. The operation is facilitated by the simultaneous presence of a constant controlling magnetic field. The same spin-valve assembly can also be used as a magnetic memory unit. We identify regions in the parameter space of the system where the logical operations can be effectively performed. The proposed gates retain the non-volatility of a magnetic random access memory (MRAM). We verify the functioning of the gate by numerically simulating its dynamics, governed by the appropriate Landau-Lifshitz-Gilbert equation with the spin-transfer torque term. The flipping time for the logical states is estimated to be within nano seconds. Further we show that current induced magneto-logic gates like AND, OR and NOT can be designed with the simple architecture involving a single nano spin-valve pillar, as an extension of our work on spin-torque-driven magneto-logic universal gates, NAND and NOR.

As another possible application, we propose and mathematically model a system of two coupled spin-torque nano-oscillators (STNO), one driver and another response, and demonstrate the synchronization of the response system to the frequency of the driver system. To this end we use a high-speed operational amplifier in the form of a voltage follower, which essentially isolates the drive system from the response system. We find the occurrence of $1:1$ as well as $2:1$ synchronization in the system, wherein the oscillators show limit cycle dynamics. An increase in power output is noticed when the two oscillators are locked in $1:1$ synchronization. Moreover in the crossover region between these two synchronization dynamics we show the existence of chaotic dynamics in the slave system. The coupled dynamics under periodic forcing, using a small ac input current in addition to that of the dc part, is also studied. The slave oscillator is seen to retain its qualitative identity in the parameter space in spite of being fed in, at times, a chaotic signal. Such electrically coupled STNOs will be highly useful in fabricating commercial spin-valve oscillators with high power output, when integrated with other spintronic devices.

TABLE OF CONTENTS

LIST OF TABLES

LIST OF FIGURES

ABBREVIATIONS

AP	Anti-Parallel
CIP	Current in Plane
CPP	Current Perpendicular to Plane
CIMS	Current Induced Magnetization Switching
DFT	Density Functional Theory
DW	Domain Wall
FIMS	Field Induced Magnetization Switching
GMR	Giant Magnetoresistance
IP	In Plane
LL	Landau-Lifshitz
LLG	Landau-Lifshitz-Gilbert
LLGS	Landau-Lifshitz-Gilbert-Slonczewski
LSDA	Local Spin Density Approximation
MRAM	Magnetic Random Access Memory
MTJ	Magnetic Tunnel Junction
OOP	Out Of Plane
P	Parallel
STNO	Spin Torque Nano Oscillator
STT	Spin Transfer Torque
SV	Spin Valve
VC	Vortex Core

NOTATION

A	Area of cross-section
R_c	Coupling resistance
V	Volume
j	Current density
G_L	Gibbs-Landau free energy
$\mathbf{M}(\mathbf{r}, t)$	Magnetization vector of Micromagnetic theory
$\mathbf{m}(\mathbf{r}, t)$	Normalized magnetization vector
α	Gilbert damping parameter
λ	Landau damping parameter
γ	Gyromagnetic ratio of electron
β	Parameter proportional to current density
c_p	Parameter proportional to degree of spin polarization
P	Degree of spin polarization
$\mathbf{S}$	Macro magnetization vector
$\mathbf{H}_{ext}$	External magnetic field
$\mathbf{h}_{ext}$	Normalised external magnetic field
$\mathbf{H}_{demag}$	Demagnetizing field inside ferromagnet
$\mathbf{H}_{exchange}$	Exchange field
$\mathbf{e}_p$	Pinning direction
ξ	Distance co-ordinate normal to metallic multilayer
ψ	WKB Hartree-Fock spinor wave function
$k_{\pm}$	Wave numbers
$\mathbf{k}_p$	Wave vector normal to ξ co-ordinate
a_{dc}	DC current
a_{ac}	AC current
ω	Frequency of ac current

θ	Angle between fixed and free layer magnetizations
$\mathit{\Phi}$	Pauli-spin flux
O	In-plane limit cycle
O^2	Out-of-plane limit cycle
S^2	Out-of-plane fixed points
P	Fixed point parallel the direction of pinning
AP	Fixed point anti-parallel to the direction of pinning
$\mathbf{n}$	The field in Faddeev-Skyrme model
$\mathcal{L}$	Lagrangain density
L	Thickness of disk
$\mathcal{H}$	Hamiltonian density
$\mathbf{T}_{STT}$	Spin transfer torque due to in-plane currents
μ_B	The Bohr magneton
$\mathbf{u}$	Velocity of the domain wall
e	Charge of the electron
$\mathbf{G}$	Gyrovector in Thiele's equation
$\mathbf{a}$	Co-ordinates of the center of the vortex
$\overset{\leftrightarrow}{\mathbf{D}}$	Dissipation tensor of second order
j_c	Critical current density

Subscripts

demag	Demagnetization
an	Anisotropy
transv	Transverse
eff	Effective
s	Saturated
ext	External
exchange	Exchange
c	Critical
P	Parallel
AP	Anti-parallel

CHAPTER 1

INTRODUCTION

> *“We see only what we know."*
>
> — Johann Wolfgang von Goethe

The first half of twentieth century saw major advancements in quantum mechanics which gave rise to band theory of solids and the field of electronics and semiconductor industry. By mid-twentieth century, the semiconductor industry was catapulted into unforeseeable growth by the invention of Integrated Circuits (IC). Intel co-founder Gordon E. Moore, in his 1965 paper(Moore, 1965), made the observation, which later came to known as the Moore’s law, that over the history of computing hardware, the number of transistors on ICs double approximately every two years. This law sets the bench mark for the semiconductor industry at present and as a result computers are getting smaller and smaller but their computational powers are getting better and better. It is only a matter of time before the size of the fundamental constituent of a micro processor, the transistor, approach nanometres and that of an atom where the laws of semiconductor physics cease to hold. This would set a fundamental limit to the downsize scalability of a single transistor. Moreover all the electronic devices rely on one fundamental property of electrons—electric charge. Directed motion of charges constitute an electric current which transport information in a conventional electronic circuit. This results in the problem of Joule’s heating which is the cause of major energy loss in electronic circuits.

In the year 1928 British physicist Paul A. M. Dirac wrote down a relativistic wave equation for electron in free space which underpinned the theory of the intrinsic angular momentum of the electron called *spin angular momentum*. It is surprising to note that the semiconductor industry, through all its years of glory, ignored the other fundamental attribute of electron; its quantum mechanical spin. Spintronics (spin-electronics), which tries to rectify this historical avoidance, makes uses of many spin related physical effects such as giant magnetoresistance (GMR), spin transfer torque effect (STT), spin hall effect, etc, to develop a new generation of electronic devices which are free from the limitations suffered by the conventional electronic devices. They also make use of spin currents, which is the directed motion of electron spins transporting information through a circuit. A spin current is determined by both the moving direction and the spin polarization of electrons. In conventional electronic devices the spin orientation of electrons are completely random and hence exhibit no role in the functioning of the device. Much of the interest in spin based devices was kindled by the 2007 Nobel price winning work on GMR by Albert Fert and Peter Gruñberg(Baibich et al., 1988; Binasch et al., 1989). It is a quantum mechanical effect observed in ferromagnetic multi-layers with non-magnetic layers sandwiched between them. When the magnetic moments of the ferromagnetic layers are parallel, the spin dependant scattering of the carriers is minimized, and the structure has relatively low resistance. When the moments of ferromagnetic layers are anti-aligned, the spin dependant scattering of the carriers is maximized, and the structure has a significantly high resistance. GMR effect can be effectively exploited for spintronics related applications using a spin valve structure (SV) or Magnetic Tunnel Junctions (MTJs). MTJs are based on Tunnel Magneto Resistance (TMR) which is an order of magnitude higher than GMR(Moodera et al., 1998; Ralph and Stiles, 2008). Spin valves are dedicated GMR systems, in which change in resistance is typically several 10's of percent. The nano spin valve system consists of a metallic spacer layer sandwiched between two ferromagnetic layers, one pinned using an anti ferromagnetic layer and the other free. In 1996, two papers by Slonczewski(Slonczewski, 1996, 1999) and Berger(Berger, 1996, 2001) came out reporting a reciprocal phenomenon of GMR, called Spin-Transfer-Torque (STT) effect, in which a current flowing perpendicular to the plane in a magnetic multilayer can exert a torque strong enough to reorient the magnetization in one of the layers. Information coded in the form of macrospin of the magnetic layer, considered as a monodomain, is thus amenable to manipulation using spin-polarized currents(Stiles and Miltat, 2006; Wolf et al., 2006). The extensive theoretical and experimental studies on spin valve geometries that followed brought into light two especially important phenomena relevant to magnetic storage technology and spintronics—current induced magnetization switching and self-sustained microwave oscillations in the nanopillar or MTJ devices(Myers et al., 1999; Grollier et al., 2001;

Kiselev et al., 2003; Rippard et al., 2004; Cros et al., 2005; Berkov and Miltat, 2008).

For the purpose of our theoretical and numerical investigations we rely on the spin valve structures as compared to MTJs because for SVs there exists a well tested theoretical model. We delve in detail into the aforementioned theoretical concepts in the next chapter. Here we introduce the two major research problems, formulated on free layer magnetization dynamics of the spin valve structure, which will be the focus of our study in the coming chapters. They can be categorized as follows:

- Spin current induced magnetization switching and STT MRAM/Magneto-logic gates
- Spin current induced magnetization precession and spin-torque nano-oscillators (STNOs)

Here we give some background into the existing literature in the above areas before outlining, very briefly, our proposals with regard to these two problems. First we turn our attention to the emerging area of STT MRAMs and logic gates. The aspect of *non-volatility*, fundamentally inherent in the GMR systems, and the significant reduction in power consumption had prompted the development of spin-valves as memory devices. The earlier proposals, however, were based on a field induced magnetic switching(FIMS) approach for writing data, which uses two orthogonal pulses of magnetic filed to achieve writing. Drawbacks of the FIMS scheme included higher power dissipation due to the relatively large currents needed to produce the required Oersted fields, and limits on localization of the magnetic field which hamper selective writing. Magnetic random access memory (MRAM) models based on current induced magnetic switching (CIMS), wherein STT phenomenon forms the core, have since been proposed. In November 2012, Everspin technologies (*www.everspin.com*) introduced a 64Mb DDR3 STT-MRAM in the market demonstrating the narrowing gulf between academic research and industry follow up in this particularly competitive area.

Apart from the more obvious application as plain memory storage devices, spin valve based magneto-logic devices have also been attempted in the recent past. FIMS based field programmable logic gates using GMR elements were proposed by Hassoun *et al.*(Hassoun et al., 1997), wherein the type of the logical operation to be performed can be altered by additional fields. Further models have also been suggested where the logical state of the GMR unit is manipulated using FIMS (Richter et al., 2002; Ney et al., 2003; Ney and Harris, 2005; Wang et al., 2005; Lee et al., 2007). Similar programmable models based on spin valve magneto-logic devices are also known in literature(Zhao et al., 2007; Dery et al., 2007). These later models, based on CIMS, involve additional spin-valve elements that together form a single logical unit, or more than one current carrying plate capable of generating fields in orthogonal directions. Besides, in these models, bi-polar currents were crucial in writing or manipulating data. Invariably, this requires a more complex architecture than is required for a simple magnetic memory unit.

Though not as mature as the STT MRAM, another emerging spintronics technology is that of spin-torque nano-oscillators (STNOs). The self-sustained oscillations in nano-pillar devices can be understood in terms of the balance between the torque generated by the damping forces and the spin transfer torque which acts in opposite direction to the former. These STNOs with oscillations in the microwave range (frequency in GHz) are excellent candidates for oscillators to be integrated into a spintronics motivated architecture. But their appeal is marred by the feeble output power from a single oscillator.

One way of improving the output power is to synchronize several such non-linear spin torque oscillators. Two different schemes of synchronizing the STNOs are often considered. In an experiment using electrical nano-contacts at close proximity on the same mesa, Kaka et.al. (Kaka et al., 2005) showed that a direct spin-wave coupling can synchronize two STNOs. This scheme has proven to be very fruitful and is replicated in various experiments(Mancoff et al., 2005; Pufall et al., 2006). Recently attempts have been made to theoretically explain the spin wave induced coupling, predominantly using linear spin wave theory(Rezende et al., 2007; Chen and Victora, 2009). Another effective coupling scheme uses electrically connected STNOs to get them phase locked to the ac generated by themselves. Following the experimental demonstration of injection locking of STNOs to applied ac current by Rippard et. al.(Rippard et al., 2005), it was numerically shown that an array of oscillators electrically connected in series mutually synchronize in frequency as well as in phase(Grollier et al., 2006). The coupling was due to the microwave component of the common current flowing through the oscillators. This and similar coupling schemes have been explored extensively in the literature ever since(Persson et al., 2007; Georges et al., 2008; Tiberkevich et al., 2009; Zhou et al., 2009; Urazhdin et al., 2010; Dussaux et al., 2011; Li et al., 2012). This way of augmenting power by an array of electrically connected phase coherent oscillators, once realized, may prove to be a great milestone towards a nano scale oscillator with useful power output. Analytical as well as numerical studies of the synchronization effects in STNOs subject to microwave magnetic fields also appear in the literature(Bonin et al., 2010; Subash et al., 2013).

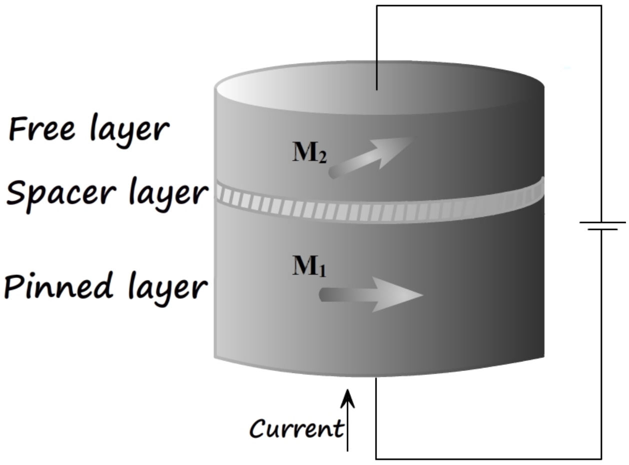

Figure 1.1: Schematic representation of the active region of a spin valve pillar in the current-perpendicular to-plane (CPP) configuration. It has a trilayer structure with a non-magnetic metallic layer (spacer) sandwiched between two ferromagnetic layers, (*pinned* layer and *free* layer.

J. C. Slonczewski in his 1996 paper estimated the torque due to transfer of spin angular momentum in now standard SV structures. This structure contains two ferromagnetic layers $\mathbf{F}_1$ and $\mathbf{F}_2$ separated by a non-ferromagnetic (NM) spacer layer1.1. The $\mathbf{F}_1$ layer is thick enough to be considered having a fixed magnetization ($\mathbf{M}_1$) which spin polarize the injected direct current through the device. On the other hand the thin free layer allows the magnetization ($\mathbf{M}_2$) to be easily movable by the current. This transfer of spin angular momentum can be treated as a torque acting of $\mathbf{M}_2$ by the spin current. Slonczewski derived an expression for this spin transfer torque (STT) in magnetic multi-layers assuming ballistic conditions and using WKB approximation(Slonczewski, 1996). The expression for time variation of free layer magnetization, $\mathbf{M}_2$, due to STT is given below(Cros et al., 2005).

$$\frac{d\mathbf{M}_2}{dt} = -P_{transv}\mathbf{M}_2 \times (\mathbf{M}_2 \times \mathbf{M}_1), \tag{1.1}$$

This term is added to the Landau-Lifshitz-Gilbert equation of magnetism to model most of the physical effects related to free layer magnetization in the GMR tri-layers (detailed account of this equation is given in chapter 2 and in appendix A). This is known as the Landau-Lifshitz-Gilbert-Slonczewski (LLGS) equation. A dimensionless form of the LLGS equation is given below:

$$\frac{\partial \mathbf{m}}{\partial t} - \alpha \mathbf{m} \times \frac{\partial \mathbf{m}}{\partial t} = -\mathbf{m} \times \mathbf{H}_{eff}, \tag{1.2}$$

where

$$\mathbf{H}_{eff} = \left(\mathbf{h}_{eff} - \beta \frac{\mathbf{m} \times \mathbf{e}_p}{1 + c_p \mathbf{m} \cdot \mathbf{e}_p} \right).$$

The free-layer magnetization **m** and the effective field $\mathbf{h}_{eff}$ are normalized by the saturation magnetization M_s. Time is measured in units of $(\gamma M_s)^{-1}$, where γ is the gyromagnetic ratio. The constant α is the damping factor and unit vector $\mathbf{e}_p$ is the direction of pinning. The other constant c_p $(1/3 \leq c_p \leq 1)$ is a function of degree of spin polarization. Refer to section 2.7 for a detailed discussion on LLGS equation and the types of dynamics admitted by it.

We use the dynamical systems approach which abstracts the free layer magnetization dynamics of the SVs using the LLGS equation. We expect very rich and interesting dynamics from such a system including limit cycles, quasi periodicity and dynamical chaos. While the research in the materials science front focusses on improving the properties of existing magnetic materials used in spintronics devices, and condensed matter theory on studying various spin system models, we focus on applying generic ideas and tools of non-linear science into the nano-spin system represented by the LLGS equation.

Here we outline the major results obtained from our studies pertaining to the two broad spintronics areas mentioned above. Regarding the STT based logic gates, we have proposed a new model magneto-logic design and numerically verified its functionality. To this end we studied in detail the control space dynamics of the LLGS equation and identified several dynamical regimes of potential interest. We studied the geometry of fixed points and how certain exchange of stability bifurcations can be effectively utilized for designing a spin logic gate. The work can be divided into two segments.

1. We propose model magneto-logic universal gates (NOR and NAND) using a spin valve pillar, wherein the logical operation is induced by spin-polarized currents which also form the logical inputs. The operation is facilitated by the simultaneous presence of a constant *controlling* magnetic field. The same spin-valve assembly can also be used as an STT MRAM(Sanid and Murugesh, 2012).
2. We show that current induced non-universal magneto-logic gates like AND, OR and NOT can be designed with the simple architecture involving a single nano spin-valve pillar(Sanid and Murugesh, 2013). This work rectifies a *redefinition* problem in the earlier work of universal gates which could have created some fabrication problems.

The new model of STT based logic gates have the following noteworthy features:

1. The MRAM/Magneto-logic gates are *non-volatile*.
2. The architecture is simple compared to other proposed models, requiring only a single GMR element for its operation.
3. The logic is programmable. For example a NOR gate can be turned into a NAND gate by reversing the polarities of the control field as well as the spin current.
4. Switching time of the logic states is within a nano second.
5. Same spin-valve can act as a STT MRAM and STT logic gate in our model.
6. Model is shown to be robust with respect to some key parameters.

Turning to the second major area of exploration, the spin-torque nano-oscillators (STNOs), we successfully applied many ideas from the theory of synchronization of non-linear oscillators producing important and far reaching results. The work again can be divided into two segments.

1. We propose and mathematically model a system of two coupled STNOs, one driver and another response, and demonstrate the synchronization of the response system to the frequency of the driver system. To this end we use a high speed operational amplifier in the form of a voltage follower which essentially isolates the drive system from the response system. We find the occurrence of 1:1 as well as 2:1 synchronization in the system, wherein the oscillators show limit cycle dynamics. An increase in power output is noticed when the two oscillators are locked in 1:1 synchronization. Moreover in the crossover region between these two synchronization dynamics we show the existence of chaotic dynamics in the slave system(Sanid and Murugesh, 2014).
2. We study the coupled dynamics under periodic forcing, using a small ac input current in addition to that of the dc part, in the master-slave scenario and demonstrate a prominent shift of the chaos regions towards low spin-current side due to coupling, and controlled by a load resistor. The slave oscillator is seen to retain its qualitative identity in the parameter space in spite of being fed in, at times, a chaotic signal. We also demonstrate the little or no effect of time delay in the coupled dynamics(Sanid and Murugesh, 2014).

Such electrically coupled STNOs will be highly useful in fabricating commercial spin-valve oscillators with high power output, when integrated with other spintronic devices.

An outline of the contents of the rest of the thesis is given below:

Chapter 2 is devoted to introducing various concepts in the area of magnetism and spintronics, needed to follow the core work of the thesis—Spin logic gates and spin torque nano oscillators. This includes fundamentals of ferromagnetism in solids, a phenomenological understanding of the giant magnetoresistance (GMR) effect, the idea of spin-transfer-torque (STT), spin valve pillars etc. We also present in this chapter the Landau-Lifshitz-Gilbert-Slonczewski (LLGS) equation and various dynamical regimes admitted by the equation using a dynamical systems approach. We also present some fundamental technological concepts needed to understand the spintronics applications of our studies. This includes the concept of field induced magnetization switching (FIMS) and current induced magnetization switching (CIMS). Finally we give a simplified working principle of a magnetic random access memory or MRAM.

Chapter 3 is devoted to spin logic gates. In this chapter, after a quick review of existing literature on the topic, we go into the detailed exploration of novel STT driven magneto logic gate designs (universal as well as non-universal), which are both simple and intuitive compared to the existing designs.

Chapter 4 is devoted to spin torque nano oscillators. In this chapter, after a quick review of existing coupling schemes, we study the various types of synchronization as well as chaotic dynamics a drive-response coupling of two STNOs can bring about. To this end, we propose a coupling using a high speed operational amplifier (Op Amp), which acts like a voltage follower.

Chapter 5 concludes the thesis with some brief remarks placing the work in a broader perspective. We also list several directions current research in the area can take.

CHAPTER 2

REVIEW OF NONLINEAR MAGNETIZATION DYNAMICS AND SPINTRONICS

> *“One can still say that quantum mechanics is the key to understanding magnetism. When one enters the first room with this key there are unexpected rooms beyond, but it is always the master key that unlocks each door"*
>
> — John H. Van Vleck

2.1 Introduction

In this chapter we piece together various concepts needed to follow the studies presented in the coming chapters. This includes fundamentals of ferromagnetism in solids, a phenomenological understanding of the giant magnetoresistance (GMR) effect, the idea of spin-transfer-torque (STT), spin valve pillars etc. We also present in this chapter the Landau-Lifshitz-Gilbert-Slonczewski (LLGS) equation and various dynamical regimes admitted by the equation using a dynamical systems approach. Some fundamental technological concepts, needed to understand the spintronics applications of our studies, get some focus towards the end of the chapter. This includes the concept of field induced magnetization switching (FIMS) and current induced magnetization switching (CIMS). Finally we give a simplified working principle of a magnetic random access memory or MRAM. We will build on the materials presented in this chapter in the subsequent chapters on spin logic gates and spin torque nano oscillators (STNO).

2.2 Basics of ferromagnetism in solids

When an electron system gets spontaneously spin polarized we have ferromagnetism in action. In transition metals it is a result of complex interplay between exchange interactions, which tend to align spins, and inter atomic hybridization, which tends to reduce the spin polarization. Qualitatively the phenomenon of ferromagnetism can be understood as follows. While filling the nearly degenerate orbitals of isolated atoms with electrons one goes by the Hund's rule, according to which one fills in electrons with spin in same direction into partially filled atomic orbitals before adding electrons with opposite spin. It is the Pauli exclusion principle and subsequently the quantum mechanical exchange interaction that explains the energy gain purported by the Hund's rule. Hence all isolated atoms with partially filled atomic orbitals have non-zero spin moments. Sometimes non-zero values of orbital angular momentum can contribute to the magnetic moments of isolated atoms.

In the case of solids the orbitals of individual atoms hybridize to form bands. This suppresses spin polarization owing to two reasons:

1. Hybridization breaks the spherical symmetry of the nuclear central potential thereby quenching orbital component of total magnetic moment.
2. Band formation adds a kinetic energy cost associated with moving electrons from lower energy filled band states to higher-energy free band states.

The end result is that most of the solids are not ferromagnetic. An important exception is solids with tightly bound $4f$-orbitals which act more or less like isolated atomic orbitals. Here the hybridization is weak and the material does become spin polarized. In this thesis we primarily deal with thin films made up of transition metal or transition metal alloys which are ferromagnetic. The mechanism for spin polarization here is the strong exchange splitting of bands. Transition metal ferromagnets have strong hybridization too, but the strong exchange splitting stabilizes the spin-polarized state by generating a self-consistent shift of the majority-electron-spin band to lower energy as compared to the minority-electron-spin band. This more than compensates for the kinetic energy cost incurred during spin polarization.

2.3 Models of ferromagnetism and the Giant Magnetoresistance (GMR) effect

In this Section we very briefly brush through various models developed to explain the ferromagnetism in solids followed by a phenomenological explanation of the giant magnetoresistance (GMR) effect. The GMR effect is of central importance to the devices we are going to model and analyse later in the thesis. The pre-eminent method of analysis is the density functional theory (DFT) with local spin density approximation (LSDA) which captures much of the essential features of ferromagentism in solids. Here the ground state properties of a system is expressed as functionals of the ground state electron density; i.e., they are determined by the a knowledge of the density alone(Jones and Gunnarsson, 1989). The total energy can be expressed in terms of such a functional. Apart from DFT, there are two other simplified models which can be used to explain certain features of ferromagentism in solids—The free electron stoner model and $s-d$ model. For our purposes here it is sufficient to understand that all these models invoke exchange splitting in some way or the other and hence a downward shift of majority-electron-spin band states relative to that of minority-electron-spin band states. As an example we shown the majority-electron-spin and minority-electron-spin band structure of cobalt, as calculated using LSDA(figure (2.1)).

For conductors like copper, the Fermi levels lie within the sp-band and the d-band is completely filled. In the case of transition metal ferromagnets like cobalt, nickel or iron the partially filled $3d$ band is split, as it contains a different number of electrons with up and down spins. Therefore, the density of states at the Fermi level (F) is also different for electrons with up and down spin. The Fermi level for majority-spin electrons is located within the sp band, and they conduct as in non-magnetic metals. For minority-spin electrons the *sp* and *d* bands are hybridized, and the Fermi level lies within the d band. The hybridized spd band has a high density of states (as shown in figure (2.1)), which results in stronger scattering and thus shorter mean free path, λ, for minority-spin than majority-spin electrons. This is the origin of ‘*spin-dependant transport*’ in ferromagnetic materials(Ralph and Stiles, 2008). This also brings about spin-polarization in magnetic thin films and makes them good *spin filters*, a concept used in the construction

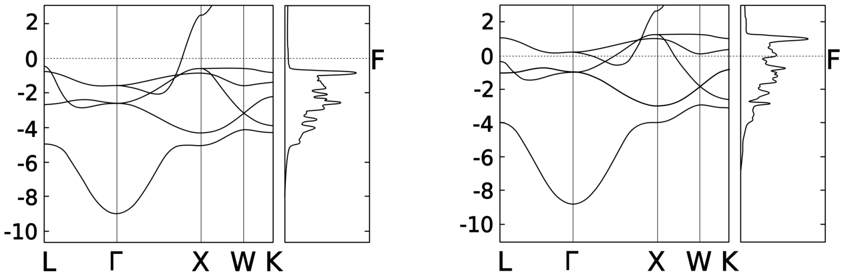

(a) Cobalt majority-spin-electron band (b) Cobalt minority-spin-electron band

Figure 2.1: Model band structure for ferromagnetic face-centered cubic (fcc) Cobalt as calculated by LSDA. Γ is the Brillouin zone center. The $3d$ band is split, as it contains a different number of electrons with up and down spins. Therefore, the density of states at the Fermi level (F) is also different for electrons with up and down spin. The vertical axis is energy in eV.

of spin valves, since electrons ‘remember’ the direction of spin within spin relaxation length or spin diffusion length (which can be much larger than the mean free path). For example, consider the Co/Cu multilayer and let electrons incident from Co layer onto the Cu layer. The majority-spin electrons entering to Co layer have a greater probability to be transported through Co film than the minority-spin electrons (since they have a shorter λ in Co). Therefore the current transmitted through Co layer in a Co/Cu/Co device will be partially spin-polarized in the majority-spin direction, while the current reflected from the Co layer will be partially polarized in the minority-spin direction. Since a spin-polarized current persists in a non-ferromagnetic material on the scale of spin diffusion length, $\sim$ 100nm in Cu, when two Co layers (with the direction of magnetization of the second layer parallel to that of the first) in the Co/Cu/Co trilayer are spaced closer than this length, majority-spin electrons easily pass through the whole structure resulting in a over all low resistance. This is true even though the minority carriers are scattered strongly through out the structure. That is to say that the majority electrons ‘short out’ the structure giving an overall low resistance. When the Co layers in the Co/Cu/Co trilyer have anti-parallel magnetizations, both majority and minority electrons undergo scattering, in one layer or the other, giving the structure a relatively high resistance. This is the celebrated GMR effect(Baibich et al., 1988; Binasch et al.,

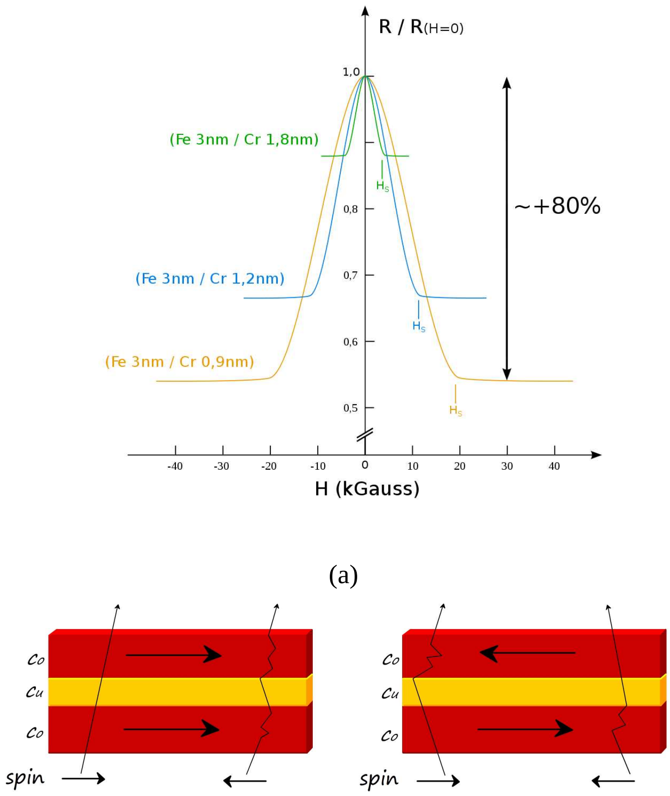

(a)

(b)

Figure 2.2: (a) First observation of GMR on Fe(001)/Cr(001) multilayers prepared by molecular beam epitaxy at 4.2K. MR = 80% for Fe 3nm/Cr 0.9nm multilayerBaibich et al. (1988). (b) The schematic of trilayer structure showing the spin dependant transport and the phenomenon of GMR.

1989). The ideas discussed thus far are expressed schematically in the figure 2.2(b). It is worth noting that in the case of Cr/Fe multi-layers in which the GMR was originally discovered, it is the minority-spin-electrons which get transmitted with less scattering and the majority-spin-electrons are scatted strongly(Vouille et al., 1999; Bass and Jr., 1999). The resistance change associated with GMR effect is quantified using the GMR ratio, which is defined as $MR = \frac{R_{AP}-R_P}{R_P} \times 100$. This can be several 10's of percent in a typical metallic trilayer structure as shown in figure 2.2(a) (Baibich et al., 1988; Chappert et al., 2007).

2.4 Spin valves (SV) and Magnetic tunnel junctions (MTJ)

Early works on GMR were based on so called current-in-plane (CIP) geometry, in which current flows in the plane of the multilayer sample. In the current-perpendicular to-plane (CPP) geometry, which is considered in this thesis, current flows perpendicular to the magnetic multilayer giving larger GMR ratio(Bass and Jr., 1999). Spin Valves (SV) are essentially the GMR trilayer sandwiches in CPP configuration in which the magnetization of one of the layers in *pinned*, either by making it thicker or by using additional layers which anti-ferromagnetically couple with the pinned layer and fix its magnetization in some direction. For the sake of ensuing discussions we shall label this layer as $\mathbf{F}_1$ and its fixed magnetization as $\mathbf{M}_1$. This layer acts as a spin polariser. On the other hand the second ferromagnetic layer, called *free* layer which is separated from $\mathbf{F}_1$ using a thin non-magnetic conducting layer, is thin and its magnetization can be altered in response to either magnetic field of spin current. This layer is labelled as $\mathbf{F}_2$ and its magnetization $\mathbf{M}_2$. A schematic of the SV pillar is shown in the figure (2.3).

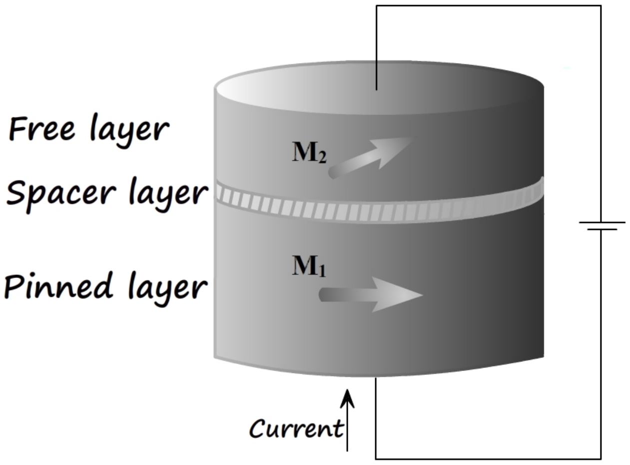

Figure 2.3: Schematic representation of the active region of a spin valve pillar in the current-perpendicular to-plane (CPP) configuration. It has a trilayer structure with a non-magnetic metallic layer (spacer) sandwiched between two ferromagnetic layers, (*pinned* layer and *free* layer. In the actual device there may be additional layers providing metallic contact for passing currents or for providing the anti-ferromagnetic coupling to enhance the pinning.

We will be mostly focussing on spin valves for our studies. But it is important to introduce magnetic tunnel junctions (MTJ) at this point because of their much higher tunnel magnetoresistance (TMR) as compared to the standard GMR(Moodera et al., 1995). MTJ has essentially the same structure as that of a spin valve pillar except that the non-magnetic metallic spacer layer has been replaced with a thin non-magnetic insulating layer. In this configuration electrons tunnel from one ferromagnetic layer to the other conserving their spin in the process. Earlier designs used an amorphous Al_2O_3 insulating layer with TMR clocking 70% at room temperature. Much higher TMR rations were later obtained using a MgO (100) tunnel barrier(Parkin et al., 2004; Yuasa et al., 2004). We focus primarily on SV because of the existence of a well tested theoretical model for their free layer magnetization dynamics. But most of the results we derive for SV can be easily extrapolated to MTJ as there exist a close resemblance between the functioning of both the devices. This is to be expected since, notwithstanding the difference in mechanism by which spin-polarized current is injected into the free layer, the interaction of spin current with the free layer magnetization is indeed given by the LLGS equation. In Section 2.9 we will take a closer look at the SV/MTJ based magnetic random access memory (MRAM) designs before going into a detailed exploration of spin logic gates in the next chapter.

2.5 Micromagnetics

In order to describe the equilibrium magnetization configuration of a ferromagnet or the magnetization dynamics under the influence of an external magnetic filed or spin current we must take the spatial in-homogeneity of magnetization into consideration. Micromagnetics is a phenomenological description of magnetism on a mesoscopic length scale which models such non-uniformities in an approximate manner. Micromagnetics is useful because, for most practical uses, the length scale of the problem is much larger than that of the atomic scale. So a description based on individual atomic moments becomes impractical, and to a good extent unnecessary.

Micromagnetics is a continuum theory, which is highly non-linear in nature and includes effects on different spatial scales, such as short range exchange forces and long-range magnetostatic effects. The state of the ferromagnet is described by a differentiable vector field $\mathbf{M}(\mathbf{r}, t)$, which represents the local magnetization at every spacial grid point inside a ferromagnet. Below Curie temperature, the ferromagnet gets spontaneously magnetized owing to the strong exchange interactions. I.e., the magnitude of the local magnetization vector at each point inside the ferromagnet becomes equal to the saturation magnetization at the given temperature T. In micromagnetics theory this is taken into account by imposing the '*fundamental micromagnetic constraint*':

$$|\mathbf{M}(\mathbf{r}, t)| = M_s \tag{2.1}$$

In a paramagentic or diamagnetic medium $\mathbf{M}(\mathbf{r}, t)$ will be proportional to the magnetic field **B**. For a ferromagnetic medium the relationship between **M** and **B** is given by:

$$\mathbf{B} = \mu(\mathbf{H} + \mathbf{M}) \tag{2.2}$$

Where **H** is the demagnetizing field inside a ferromagnet, henceforth denoted by $\mathbf{H}_{demag}$. The vector field $\mathbf{M}(\mathbf{r}, t)$ represents, in general, a non-uniform magnetization. At equilibrium, however, the spatial distribution of $\mathbf{M}(\mathbf{r}, t)$ is such that the corresponding Gibbs-Landau free energy is minimized(Bertotti et al., 2009). This is a functional of $\mathbf{M}(\mathbf{r}, t)$ and external magnetic field $\mathbf{H}_{ext}$ (temperature dependence is suppressed since a temperature uniform in space and constant in time is assumed in the subsequent discussions). This micromagnetic free energy can be expressed as a sum of contributions arising out of different material properties and phenomena. For our purposes the following contributions are considered:

1. Exchange energy: Penalizes non-uniformities in the magnetization orientation.
2. Anisotropy energy: Penalizes magnetization orientation not along (either parallel or anti-parallel) the direction of crystal easy axes.
3. Magnetostatic energy: Energy of interaction with the demagnetizing field inside a ferromagnet. Penalizes uniform orientations.
4. Energy of interaction with external magnetic field: Penalizes magnetization orientations not parallel to the direction of applied field

The magnetostatic field, $\mathbf{H}_{demag}$ is determined by solving the pair of magnetostatic Maxwell's equations, subject to appropriate boundary conditions:

$$\nabla \times \mathbf{H}_{demag} = 0, \quad \nabla \cdot \mathbf{H}_{demag} = -\nabla \cdot \mathbf{M}. \tag{2.3}$$

A graphical idea of the competing energies can be derived from figure (2.4). As can be seen from the figure, exchange energy is high for disordered magnetic configurations compared to the ordered ones (figure 2.4 (a)). Anisotropy contribution is more for magnetization orientations not along one of the easy axes (figure 2.4 (b)). Magnetostatic energy is more for uniform magnetizations as compared to the non-uniform ones (figure 2.4 (c)). Interaction energy with the external field is minimum if the individual magnetization vectors align in the direction of the field and is high otherwise (figure 2.4 (d)). It is mainly due to the competition between the short range exchange field and the long range magnetostatic field that the spatially extended ferromagnets develop internal domains instead of getting uniformly magnetized even below Curie temperature.

Incorporating all the above energies, the Gibbs-Landau free energy, G_L, for a ferromagnet occupying a region Ω can be written as the following volume integral(Bertotti et al., 2009):

$$\begin{aligned} G_L[\mathbf{M}(\mathbf{r},t);\mathbf{H}_{ext})] = \int_\Omega \Bigg[& \frac{A}{M_S^2}\left((\nabla M_x)^2 + (\nabla M_y)^2 + (\nabla M_z)^2\right) \\ & + f_{an}(\mathbf{M}) - \frac{\mu_0}{2}\mathbf{M}\cdot\mathbf{H}_{demag} - \mu_0 \mathbf{M}\cdot\mathbf{H}_{ext}\Bigg]\, \mathrm{d}V \end{aligned} \tag{2.4}$$

Where the terms in the R.H.S of the equation (2.4) appear in the same order as enumerated before. The constant A is the exchange stiffness constant, typically of the order of $10^{-11}\,\mathrm{J\,m^{-1}}$. $f_{AN}(\mathbf{M})$ describes crystal anisotropy effects. H_{ext} is the external applied field and which is a given vector valued function.

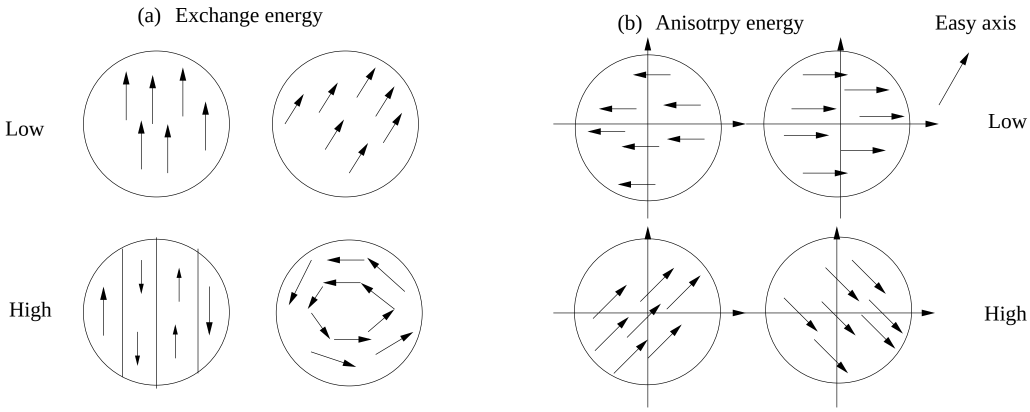

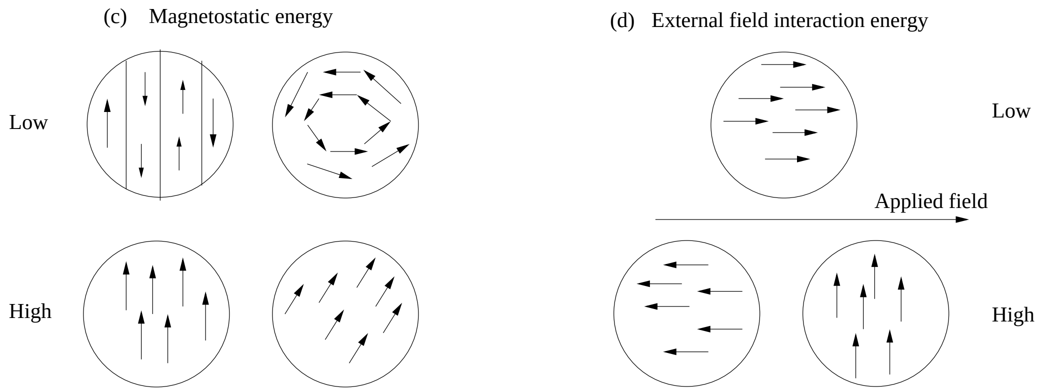

Figure 2.4: Simplified graphical depiction of competing energies making up the Gibbs-Landau free energy. ‘Low’ and ‘High’ suggest low and high contribution of the corresponding term to the free energy.

2.6 The Landau-Lifshitz-Gilbert equation

Once an external field is given, in order to find equilibrium magnetization states we need to find the extrema of the free energy functional with respect to arbitrary variations of the vector field $\mathbf{M}(\mathbf{r})$ subject to the micromagnetic constraint (equation (2.1)). The variations, denoted by δG_L, is given by:

$$\delta G_L = -\mu_0 \left[\int_\Omega \mathbf{H}_{eff} \cdot \delta\mathbf{M}\, \mathrm{d}V - \frac{2A}{\mu_0 M_s^2} \oint_\Sigma \frac{\partial \mathbf{M}}{\partial n} \cdot \delta\mathbf{M}\, \mathrm{d}S \right] , \tag{2.5}$$

where the Σ is the surface of the ferromagnet and $\partial/\partial n$ is the normal derivative at Σ. We define the effective field, $\mathbf{H}_{eff}$, as:

$$\mathbf{H}_{eff} = \mathbf{H}_{ext} + \mathbf{H}_{demag} + \mathbf{H}_{an} + \mathbf{H}_{exchange} \, , \tag{2.6}$$

where the anisotropy field, $\mathbf{H}_{an}$ and the exchange field, $\mathbf{H}_{exchange}$ is obtained from the corresponding energy terms in the Gibbs-Landau free energy.

$$\mathbf{H}_{an} = -\frac{1}{\mu_0}\frac{\partial f_{an}}{\partial \mathbf{M}}, \quad \mathbf{H}_{exchange} = \frac{2A}{\mu_0 M_s^2}\nabla^2\mathbf{M} \tag{2.7}$$

The variations in free energy with respect to arbitrary variations $\delta\mathbf{M}$ consistent with constraint (2.1) should vanish at equilibrium; i.e., $\delta G_L = 0$. This yields the Brown's equation(Bertotti et al., 2009):

$$\mathbf{M} \times \mathbf{H}_{eff} = 0, \tag{2.8}$$

$\forall$ points in Ω. The physical content of the Brown's equation is that, at equilibrium, the local torque experienced by the magnetization due to the effective field at each point inside the ferromagnet is zero. When $\mathbf{M} \times \mathbf{H}_{eff} \neq 0$, the magnetization is not at equilibrium and will evolve according to some dynamical equation. Such an equation, first proposed by L.D. Landau and E.M Lifshitz in 1935, was based on the idea that the magnetization vector $\mathbf{M}(\mathbf{r}, t)$ precess around the effective field when pushed away from equilibrium. We follow T. L. Gilbert here(Gilbert, 2004) to provide a derivation of the Landau-Lifshitz equation without the dissipation term.

From classical mechanics we know that the rate of change of angular momentum, **L**, of a rigid body is equal to the net torque (**T**) acting on it.

$$\frac{\mathrm{d}\mathbf{L}}{\mathrm{d}t} = \mathbf{T}. \tag{2.9}$$

Equation (2.9) remains valid in quantum mechanics when **L** and **T** are reinterpreted as operators in a Hilbert space. Further it can be used for spin systems by replacing the angular momentum operator **L** with the operator **S** for spin angular momentum associated with electron spin.

$$\frac{\mathrm{d}\mathbf{S}}{\mathrm{d}t} = \mathbf{T}. \tag{2.10}$$

Equation (2.10) can be used for a classical spin system provided we replace the operators with their expectation values over appropriate quantum states or a density matrix. Now, since the magnetic moment of an electron is related to the spin momentum by $\mathbf{M} = -\gamma\mathbf{S}$, where $\gamma > 0$ is the gyromagnetic ratio for electron spin, the torque experienced by a magnetic moment in an external magnetic field $\mathbf{H}_{eff}$ is:

$$\frac{\partial \mathbf{M}}{\partial t} = -\gamma \mathbf{M} \times \mathbf{H}_{eff}, \tag{2.11}$$

where $\gamma = 2.2{\times}10^5\,\mathrm{A}^{-1}\ \mathrm{ms}^{-1}$, determines the precession rate. Dynamics prescribed by equation (2.11) conserves the magnitude of the magnetization, $|\mathbf{M}|$, for it follows directly from equation (2.11) that $\mathbf{M} \cdot \partial \mathbf{M}/\partial t = 0$ consistent with the micromagnetic constraint (2.1). Since this equation cannot describe any approach to equilibrium, additional phenomenological term can be added to account for dissipation. One such approach was taken by Landau and Lifshitz themselves proposing a damping term proportional to the compoent of $\mathbf{H}_{eff}$ which is perpendicular to the magnetization. The Landau-Lifshitz (LL) equation(Landau and Lifshitz, 1935) with the damping term is given below:

$$\frac{\partial \mathbf{M}}{\partial t} = -\gamma' \mathbf{M} \times \mathbf{H}_{eff} - \frac{\lambda \gamma'}{M_s} \mathbf{M} \times (\mathbf{M} \times \mathbf{H}_{eff}), \tag{2.12}$$

where λ is the Landau-Lifshitz damping parameter. T. L. Gilbert(Gilbert, 2004) proposed a different phenomenological term to take into account dissipation in ferromagnetic systems employing a Lagrangian formulation of magnetization dynamics and a Rayleigh dissipation function. The equation has the following form, which is known as the Landau-Lifshitz-Gilbert (LLG) equation. In our studies we mostly will be following the LLG equation:

$$\frac{\partial \mathbf{M}}{\partial t} = -\gamma \mathbf{M} \times \mathbf{H}_{eff} + \frac{\alpha}{M_s} \mathbf{M} \times \frac{\partial \mathbf{M}}{\partial t}, \tag{2.13}$$

where α is the Gilbert damping coefficient. The two equations are equivalent if γ' and γ are related by $\gamma' = \gamma/(1+\alpha^2)$. It is often convenient to rewrite the LLG equation in the normalized form, where the magnetization and fields are measured in units of M_s and energies are measured in the units of $\mu_0 M_s^2 V$, V being the volume of the ferromagnet. The magnetization states are described by the following vector with modulus 1:

$$\mathbf{m}(\mathbf{r}, t) = \frac{\mathbf{M}(\mathbf{r}, t)}{M_s}, \tag{2.14}$$

and the micromagnetic constraint, equation (2.1) takes the form:

$$|\mathbf{m}(\mathbf{r}, t)| = 1. \tag{2.15}$$

The normalized free energy is defined as $g_L[\mathbf{m};\mathbf{H}_{ext}] = \frac{G_L[\mathbf{M};\mathbf{H}_{ext}]}{\mu_0 M_s^2 V}$. Measuring time in the units of $(\gamma M_s)^{-1}$ and defining $\mathbf{h}_{eff} \equiv \frac{\mathbf{H}_{eff}}{M_s}$ one obtains, from equation (2.13), the normalized LLG equation:

$$\frac{\partial \mathbf{m}}{\partial t} = -\mathbf{m} \times \mathbf{h}_{eff} + \alpha \mathbf{m} \times \frac{\partial \mathbf{m}}{\partial t}. \tag{2.16}$$

For permalloy, with $\gamma = 2.2{\times}10^5$ A^{-1} ms^{-1} (1.7 × 10^{-7} Oe^{-1} s^{-1}) and $M_s = 8{\times}10^5$ A m^{-1}, $(\gamma M_s)^{-1} \simeq 6$ ps. We will add one more term to the equation (2.13) in the subsequent section to account for the spin-transfer-torque effect in ferromagnetic multilayers.

It should be noted that most of our studies are focussed on spin valve pillars which are made up of thin films having area of cross section ∼100×100 nm^2 and hence the spatial inhomogeneity in magnetization is usually negligible. Also there are fabrication techniques which produce thin films with a single domain with uniform magnetization. So it is reasonable to throw away the exchange field contribution in equation (2.6). That is, we assume a *monodomain* ferromagnetic thin film in most of our calculations. This approximation is called *monodomain* approximation.

2.7 The spin-transfer-torque (STT) effect and the LLGS equation

Spin-polarised current flowing through a magnetic nano structure can influence its magnetic state due to the exchange interaction between the spin of the incoming conduction electrons and the spin of the electrons responsible for the local magnetization (transfer of spin angular momentum). This effect lies at the heart of most of the device physics we are going to study in this thesis. Two papers, independently by J.C. Slonczewski and L. Berger in 1996, were most influential in the study of spin-transfer-torques(Slonczewski, 1996; Berger, 1996). They independently predicted that current flowing perpendicular to the plane in a metallic multilayer can generate a spin transfer torque strong enough to reorient the magnetization in one of the layers. Information coded in the form of macrospin of the magnetic layer, considered as a monodomain, is thus amenable to manipulation using spin-polarized currents(Stiles and Miltat, 2006; Wolf et al., 2006).

Since the low resistance SV pillars we have been discussing can easily sustain current densities at which spin-transfer-torques become important, it becomes natural to study them in such structures.

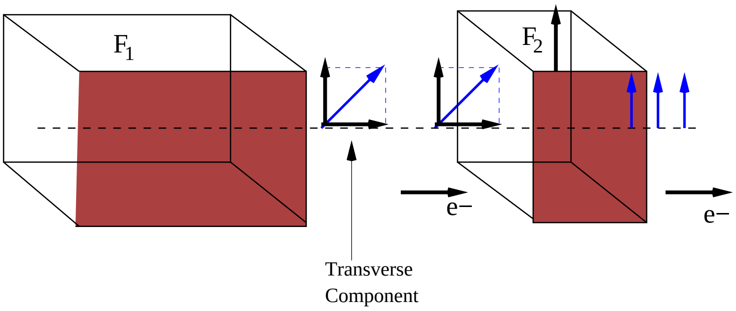

Figure 2.5: The schematic of standard SV trilayer geometry originally proposed by J. Slonczewski. It consists of two ferromagnetic layers F_1 and F_2 separated by a thin non-ferromagnetic conducting layer sandwiched between them. The thick F_1 layer spin polarizes the injected direct current where as F_2 is thin enough to be considered as a monodomain whose macro magnetization vector can experience the spin transfer torque effect. The transverse component of the spin angular momentum of the electrons are absorbed and transferred to the local moments in F_2 when they pass through this layer. This results in a torque that can excite or reverse the magnetization $\mathbf{M}_2$.

J. C. Slonczewski in his 1996 paper estimated the torque due to transfer of spin angular momentum in now standard SV structures, whose schematic is given in figure (2.5)(Slonczewski, 1996). This structure contains two ferromagnetic layers $\mathbf{F}_1$ and $\mathbf{F}_2$ separated by a non-ferromagnetic (NM) spacer layer. The $\mathbf{F}_1$ layer is thick enough to be considered having a fixed magnetization ($\mathbf{M}_1$) which spin polarize the injected direct current through the device. On the other hand the thin free layer allows the magnetization ($\mathbf{M}_2$) to be easily movable by the current. When the electrons are injected perpendicular to the layers, the direction of spin polarization in the metallic layer cannot be parallel to both $\mathbf{M}_1$ and $\mathbf{M}_2$ but makes an angle with $\mathbf{M}_2$ (in the case where $\mathbf{M}_1$ and $\mathbf{M}_2$ are not collinear). When these electrons pass through the free layer, due to exchange interaction, they align their spins in the direction of $\mathbf{M}_2$. Due to the spin conserving nature of exchange interaction, what this amounts to is that the transverse component of spin angular momentum of electrons has been absorbed and transferred to $\mathbf{M}_2$. This transfer of spin angular momentum can be treated as a torque exerted on $\mathbf{M}_2$ by the spin current. Slonczewski derived an expression for this spin transfer torque (STT) in magnetic multi-layers assuming ballistic conditions and using WKB approximation(Slonczewski, 1996). The expression for time variation of free layer magnetization, $\mathbf{M}_2$, due to STT is given below(Cros et al., 2005) (see Appendix A for a more detailed exposition).

$$\frac{d\mathbf{M}_2}{dt} = -P_{transv}\mathbf{M}_2 \times (\mathbf{M}_2 \times \mathbf{M}_1) \, , \tag{2.17}$$

This term is added to the Landau-Lifshitz-Gilbert equation (2.16) to model most of the physical effects related to free layer magnetization in the GMR trilayers. Without going into much details we give below the normalized Landau-Lifshitz-Gilbert-Slonczewski (LLGS) equation in the dimensionless form(Bertotti et al., 2005) (see Appendix B for a complete derivation). Similar to what was done in previous Sections, a time rescaling has been done and time is expressed in the units of $(\gamma M_s)^{-1}$, i.e., $t \to \gamma M_s t$. We already gave approximate numbers pertaining to permalloy film, so here we give some numbers for Cobalt. For Co, $M_s \simeq 1.4 \times 10^6$ A m^{-1} and hence $(\gamma M_s)^{-1} \simeq 3.2$ ps.

$$\frac{\partial \mathbf{m}}{\partial t} - \alpha \mathbf{m} \times \frac{\partial \mathbf{m}}{\partial t} = -\mathbf{m} \times \left(\mathbf{h}_{eff} - \beta \frac{\mathbf{m} \times \mathbf{e}_p}{1 + c_p \mathbf{m} \cdot \mathbf{e}_p} \right) , \tag{2.18}$$

where $\mathbf{m}(\equiv \{m_x, m_y, m_z\})$ is the normalized magnetization vector of the free layer and $\mathbf{e}_p$ is the pinning direction of the fixed layer magnetization. The effective field consists of an external magnetic field (h_{ext}), anisotropy field, demagnetization field perpendicular to the layer and an exchange field for spatially extended films with inhomogeneous magnetization as already stated in equation (2.6). The other constant c_p $(1/3 \leq c_p \leq 1)$ is a function of degree of spin polarization P $(0 \leq P \leq 1)$:

$$c_p = \frac{(1+P)^3}{3(1+P)^3 - 16P^{3/2}} . \tag{2.19}$$

In the numerical calculations we have used the typical value of $P = 0.3$. c_p is a small number compared to 1 for all realistic values of P. The parameter β is proportional to the spin current density (typically of the order of 10^{-2}—10^{-3} for Co layers, with current densities $\sim 10^8$ A/cm^2).

It should be noted that the equation (2.18) can be used in dimension-full form as well, as we will do in the chapter on spin-torque nano oscillators. Also the term proportional to degree of spin polarization can be grouped with the coefficient β, by defining an appropriate new function $g(P)$, making the equation simpler to work with. Such alternative forms of LLGS equation also will be used extensively in the thesis. In the next Section we give an overview of the new dynamical effects brought about by the addition of Slonczewski term to the LLG equation.

2.8 Dynamical systems approach and STT driven magnetization dynamics

The spin-transfer interaction between the spin current and the magnetization can give rise to two major effects:

- Current induced magnetization switching
- Self-sustaining magnetization precession at microwave frequencies in SV pillars.

Current-induced magnetization switching has been extensively studied in nanopillar devices(Myers et al., 1999; Grollier et al., 2001; Albert et al., 2000; Krivorotov et al., 2004; Albert et al., 2002; Braganca et al., 2005; Mangin et al., 2006). Figure (2.6) shows comparisons between spin-torque driven magnetization switching and magnetic field driven magnetization switching in the case of a spin valve nanopillar device. More difficult has been the search for current induced microwave oscillations in SV pillars, but there is mounting experimental evidence in the literature for the phenomenon(Kiselev et al., 2003; Rippard et al., 2004; Cros et al., 2005; Berkov and Miltat, 2008). Rippard et. al. in 2004 reported direct measurements of spin-current induced magnetization dynamics as a function of field strength H and current I. The spin valve structures were Co$_{90}$Fe$_{10}$ (20 nm)/Cu (5 nm)/Ni$_{80}$Fe$_{20}$ (5 nm) with typical MR values of $80\,m\Omega$. The Co$_{90}$Fe$_{10}$ acted as the pinned layer due to its large volume, exchange stiffness, and saturation magnetization compared to Ni$_{80}$Fe$_{20}$. The device is contacted with microwave probes

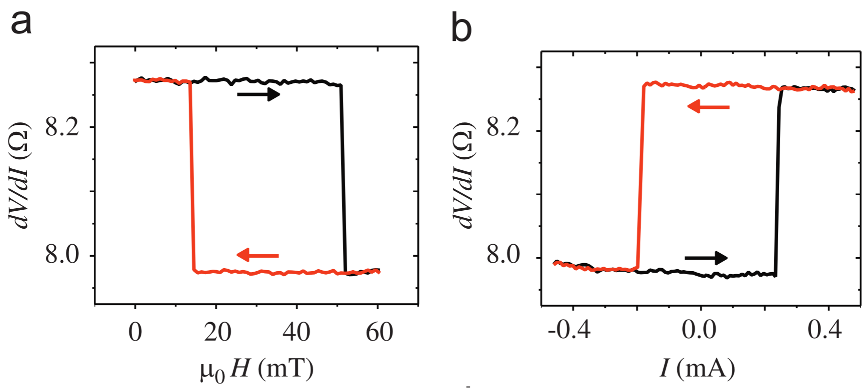

Figure 2.6: Comparison of magnetization switching scenario in a SV pillar at room temperature as driven by spin-transfer-torques vis-á-vis applied magnetic field. (a) Switching of an all metal nanopillar device consisting of layers 20 nm $Ni_{81}Fe_{19}$/ 12 nm Cu/ 4.5 nm $Ni_{81}Fe_{19}$, as the magnetization of the free layer is aligned parallel and antiparallel to the pinned layer by the applied magnetic field. The differential resistance, $\mathrm{d}V/\mathrm{d}I$ is plotted on the Y axis.(b) Spin-transfer-torque driven magnetization switching by an applied current in the same device with a constant magnetic field applied to give zero total field acting on the free layer. Figure based on data from (Braganca et al., 2005). Reprinted with permission. Copyright [Applied Physics Letters 2005], AIP Publishing LLC.

and a dc current is injected through a bias-tee, along with a 20 μA ac current (500 Hz), allowing simultaneous measurement of the dc resistance, differential resistance, and microwave output. The devices are current biased so that changes in the alignment between the $Ni_{80}Fe_{20}$ and $Co_{90}Fe_{10}$ layers appear as voltage changes across the point contact. Spin current induced oscillations are directly observed in the figure (2.7) reproduced from (Rippard et al., 2004). For low currents, no peaks are observed in the spectra. As I is increased to 4 mA a peak appears at f = 7.9 GHz. Upon increasing I further, the peak frequency decreases (for in-plane fields). This frequency redshift is linear in I, as shown in the inset. At higher values of I, the excitations decrease in magnitude until no peaks are observed, as shown in the $I = 9$ mA spectrum.

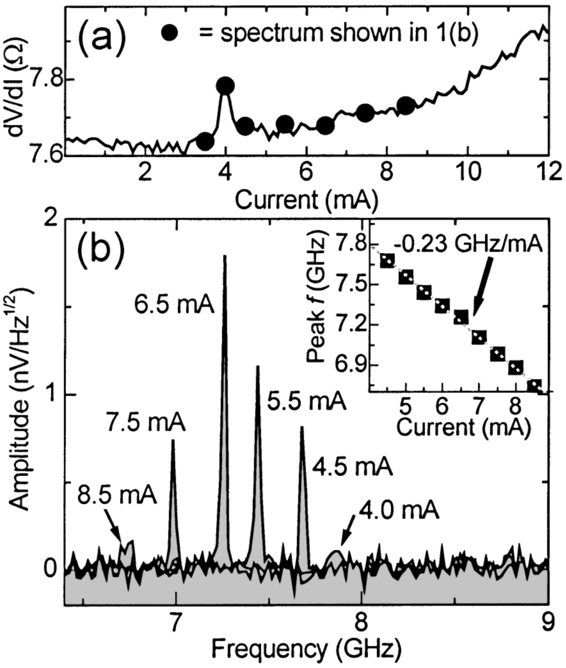

Figure 2.7: (a) $\mathrm{d}V/\mathrm{d}I$ vs I with $\mu_0 H = 0.1\,\mathrm{T}$. (b) High frequency spectra taken at several different values of current through the nanopillar device. Inset: Variation of frequency of precession with I. The frequency redshift is linear. Figure reprinted with permission from(Rippard et al., 2004). Copyright (2004) by the American Physical Society.

Qualitatively, the types of dynamics brought about by spin-transfer-torques can be understood by looking closely at the equation (2.18). The dynamical systems perspective reveals some robust and general features of this system as they are topological in nature. When external field $\mathbf{h}_{ext}$ and current β are constant in time, the equation (2.18) is an autonomous system on the unit sphere. The dynamics is confined to the surface of the unit 2-sphere (S^2) because of the fundamental micromagnetic constraint (equation (2.15)). This immediately leads to the following conclusions regarding the admissible dynamical states of the system:

- Chaos is precluded. Since LLGS equation with micromagnetic constraint is essentially a two dimensional continuous time dynamical system on unit 2-sphere (when external field $\mathbf{h}_{ext}$ and current β are constant in time and when a monodomain approximation holds). We will come back to this fact many times later in the thesis.

- Steady states are confined to either *fixed points* or *limit cycles*. Spin-torque can destabilize a previously stable fixed point and just as well stabilize a previously unstable fixed point paving the way to magnetization switching. We will delve deep into this kind of behaviour when we discuss the magneto-logic gates. self-sustained microwave oscillations are naturally associated with stable limit cycles. We will see glimpses of this behaviour in the next chapter and explore them in great detail in chapter 4.

As already stated in Section 2.7, the coefficient β appearing in equation (2.18) is at most 10^{-3}—10^{-2}, for Co layers for the typical current densities reported in the experiments ($\sim$ 10^{7}—10^{8} A cm^{-2}), which is of the same order of magnitude as that of the damping coefficient α. It is reasonable to conclude that the direction of spin-transfer-torque, as predicted by equation (2.13), is either parallel to the damping, strengthening it, or anti-parallel to the damping, weakening it. This is true for circular precession in the absence of anisotropy fields. In the presence of magnetic anisotropy the precession is elliptical and hence the instantaneous orientations of the spin torque and the damping are not always collinear, but on average over each cycle the spin torque can still be understood as either reinforcing or acting opposite to the damping(Ralph and Stiles, 2008). See figure (2.8) for a pictorial representation of the damping torque as well as spin-torque acting on a magnetization vector as predicted by equation (2.13) when no magnetic anisotropies are present. According to LLGS equation, when the above conditions hold, the free layer magnetization **m** once perturbed away from the equilibrium position executes circular precession around the direction of the $\mathbf{H}_{ext}$ (assumed to be along $\hat{\mathbf{z}}$). Now if damping is switched on, due to damping torque shown in figure (2.8), the magnetization is slowly pushed towards the equilibrium position. The system dissipates energy and the precession angle decreases gradually and the magnetization slowly relaxes to the equilibrium position in a spiral path. If a current is now switched on, depending on the polarity, it can either strengthen or weaken the damping force. In the case when the spin-torque opposes damping, a small current has the effect of reducing the damping and the magnetization relaxation to equilibrium becomes slow.

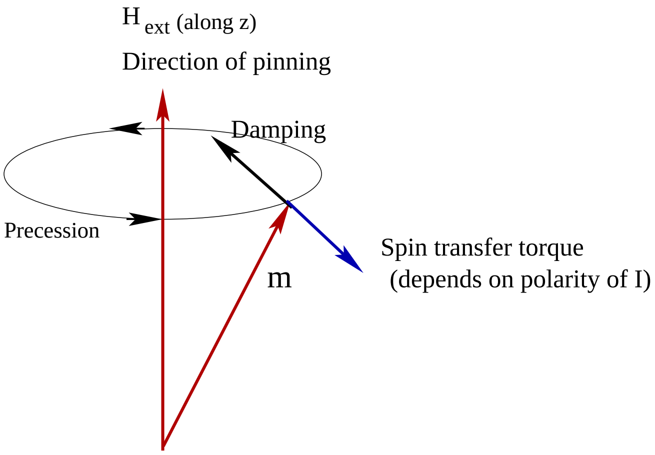

Figure 2.8: Simplified schematic showing the directions of damping torque and spin-transfer-torque according to LLGS equation for circular precession.

Nothing interesting happens as yet. But larger current amplitudes can destabilize the fixed point at the north pole along $\hat{\mathbf{z}}$, simultaneously giving birth to a stable limit cycle (Hopf bifurcation). Thus current destabilizes the orientation of $\mathbf{m}$ along the equilibrium direction and excites large angle precession dynamics. The system achieves a dynamical equilibrium; the energy gained from the spin torque during each cycle of precession is balanced by the energy lost to damping. This is the origin of microwave precession in spin-torque nano oscillators. At still larger current values the spin-torque completely takes over the damping term and the precession angle is excited to ever-increasing values until eventually it reaches 180°. The physical meaning is that the direction of $\mathbf{m}$ is reversed. Thus explaining the current induced magnetization switching. These possible spin-torque driven magnetization dynamics scenarios are graphically represented in figure (2.9).

In the next Section we do a quick review of various MRAM designs based on spin valve pillars.

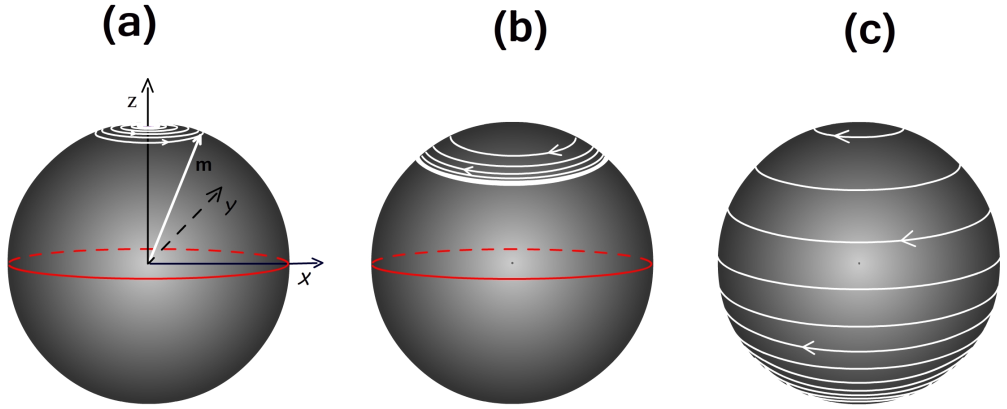

Figure 2.9: Representative trajectories of spin-torque driven dynamics of macro magnetization vector **m** on S^2. (a) For low spin current values, ($j < j_{critical}$), damping dominates over spin-torque and the magnetization relaxes to the stable equilibrium point at the north pole. (b) and (c) For high current values spin-torque dominates over damping. Two scenarios can arise depending upon the angular dependence of damping as well as spin-torque: Large angle self-sustained precession (shown in (b)), and at even larger current values or complete magnetization reversal (shown in (c)).

2.9 MRAM designs using spin valve pillars

The discovery of the giant magnetoresistance (GMR) effect and the development of spin-valve structures kindled a race to develop magnetic random access memory, or MRAM. Devices based on the GMR and TMR effects have already found very widespread application as the magnetic field sensors in the read heads of magnetic hard disk drives. The aspect of *non-volatility*, fundamentally inherent in the system, and the significant reduction in power consumption have been the winning factors for spin-valves as memory devices. The MRAM designs fall under two categories—Ones based on field induced magnetization switching (FIMS) and the ones based on current induced magnetization switching (CIMS).

2.9.1 FIMS based MRAM

Here two orthogonal pulses of magnetic field are used to achieve writing. Hence the name *field induced* magnetization switching, or FIMS. The binary information ‘0’ and ‘1’ is recorded using the two opposite orientations of the magnetization of the free layer along its easy magnetization axis. The SV/MTJ are connected to the crossing points of two perpendicular arrays of parallel conducting lines. For writing, current pulses are sent through one line of each array, and only at the crossing point of these lines is the resulting magnetic field high enough to reorient the magnetization of the free layer. For reading, the resistance between the two lines connecting the addressed cell is measured. In principle, this *cross-point architecture* promises very high densities. A schematic representation of FIMS based MRAM is given in figure (2.10) which is based on the first MRAM product, a 4-Mbit stand-alone memory(Engel et al., 2005) commercialized by Freescale in 2006. Drawbacks of the FIMS scheme include higher power dissipation due to the relatively large currents needed to produce the required Oersted fields, and limits on localization of the magnetic field which hamper selective writing.

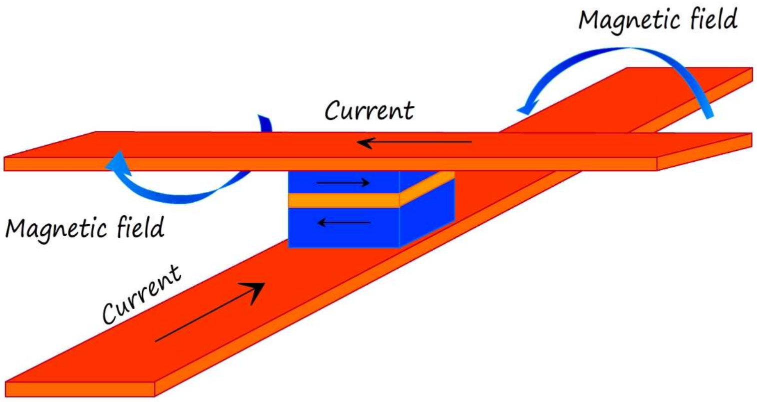

Figure 2.10: Schematic representation of an FIMS based MRAM. To write an MRAM bit, current is passed through the conducting lines. The sum of magnetic field from both the lines is needed to flip the free layer magnetization. To read an MRAM bit, current is passed through the cell and the resistance of the cell is sensed.

2.9.2 CIMS based MRAM

Magnetic random access memory (MRAM) models based on *current induced* magnetic switching, wherein STT phenomenon forms the core, have since been proposed. Here the current sent through the spin valve structure would be greater than the critical current needed to switch the free layer magnetization. Current of opposite polarity would switch the magnetization back to its original direction. Thus writing ‘0’ or ‘1’ as per interpretation. A simplified schematic of STT based MRAM is given in figure (2.11). This clearly solves the selectivity and scalability issue suffered by the FIMS approach.

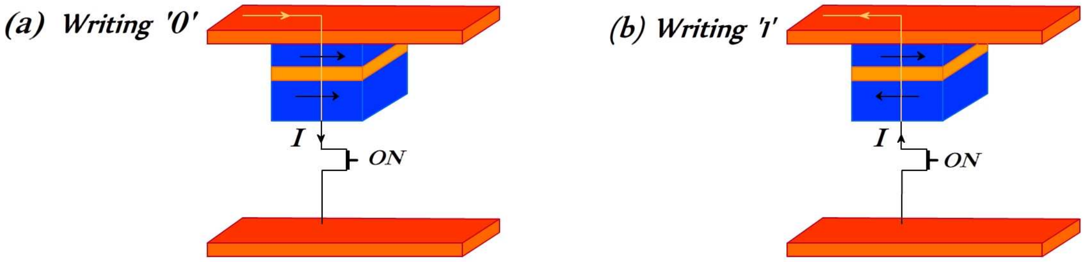

Figure 2.11: Schematic representation of an CIMS based MRAM. To write an MRAM bit, current, whose magnitude is greater than some critical value, is passed through the nano pillar structure. A current with opposite polarity would be used to write the other bit.

The selectivity issue is taken care of since write current is flowing only through the addressed cell and hence there is no risk of writing an unselected cell. Also, since the switching is determined by a current density, the total current required to write a memory cell scales as the area of the cell. Thus, the smaller the cell is the smaller the write current. This contrasts with the FIMS approach in which the current for writing actually increases as the cell size decreases. As a result, the STT approach offers good scalability in STT-MRAM down to cell size of the order of 45 nm(Dieny et al., 2010). STT based MRAMs have potentially infinite endurance (compared with $\sim 10^5$ cycles for a Flash memory) and potential for sub-nanosecond operation, that make them strong candidates for universal memory(Chappert et al., 2007). In November 2012, Everspin technologies introduced a 64Mb DDR3 STT-MRAM to the market. The *racetrack* memory conceived by IBM technologies is also based on spin torque effects; specifically they make use of current driven domain wall motion in a 3D array of nanowires(Parkin et al., 2008) . There is a huge energy gain in this device because the movable mechanical read head of conventional magnetic storage is not required here. The memory bits, arranged sequentially on a nanowire, are pushed through the read head using spin current instead of read head locating the memory bit using actuators(S.S.P. Parkin, United States Patent # 6,834,005, December 21, 2004).

2.10 Outlook

Spintronics as a contemporary area of technology bridges the gap between fundamental research and technology follow up. Much of the insights churned out by fundamental research is immediately taken up by the industry in terms of new and improved technology solutions. This is specifically true in the area of MRAM technology and magneto-logic gates. The possibility of commercial application has been a strong driving force in this field from the beginning. The phrase ‘GMR’ now appears in over 1500 US patents. With the concepts presented in this chapter we can now move to the detailed study of spin logic gates and spin torque nano oscillators, both actively pursued by both academia and industry. In the next chapter a detailed study of spin based logic gates are presented.

CHAPTER 3

SPIN LOGIC GATES

> *“The logic of the world is prior to all truth and falsehood."*
>
> — Ludwig Wittgenstein

3.1 Introduction

As seen in the earlier chapters, the discovery of the celebrated giant magnetoresistance (GMR) effect and the spin transfer torque (STT) effect followed by the development of spin-valve structures kindled a race to develop spin based memory devices. It became apparent that STT effect generates a torque strong enough to reorient magnetization of the free layer in spin valve pillars. Information coded in the form of macrospin of the magnetic layer, considered as a monodomain, is thus amenable to manipulation using spin-polarized currents. The next step in STT based technology was naturally the spin logic gates. Many innovative spin logic gate models has been proposed in the literature, some of them making use of FIMS whereas some of them are based on STT and CIMS. In this chapter, after a quick review of existing literature on the topic, we go into the detailed exploration of novel STT driven magneto logic gate designs (both universal and non-universal), which are both simple and intuitive compared to the existing designs(Sanid and Murugesh, 2012, 2013). We propose magneto-logic gates using a spin valve pillar, wherein the logical operation is induced by spin-polarized currents which also form the logical inputs. The operation is facilitated by the simultaneous presence of a constant *controlling* magnetic field. The same spin-valve assembly can also be used as a magnetic memory unit. We identify regions in the parameter space of the system where the logical operations can be effectively performed. The proposed gates retain the non-volatility of a magnetic random access memory (MRAM). We verify the functioning of the gate by numerically simulating its dynamics, governed by the appropriate Landau-Lifshitz-Gilbert equation with the spin-transfer torque term. The flipping time for the logical states is estimated to be within nano seconds. The model is also shown to be robust against fluctuations of some key parameters in the model.

3.2 Spin valve pillars as magneto-logic gates

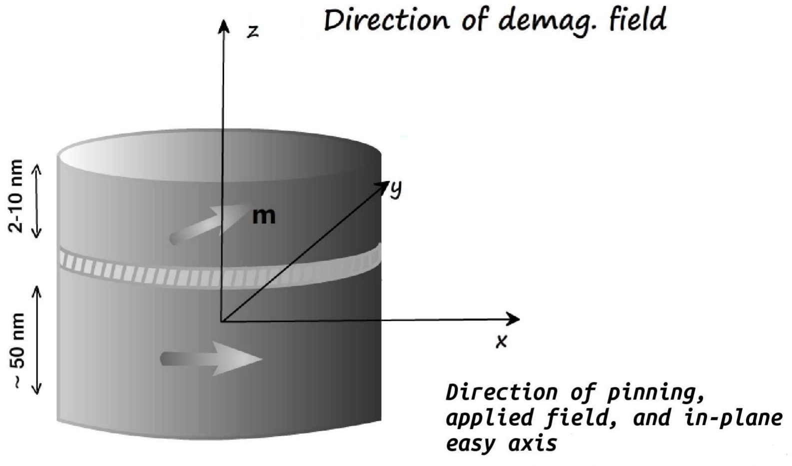

Figure 3.1: Schematic representation of the spin valve geometry based on which the novel magneto-logic universal as well as universal gates are designed. The pinning direction is $\hat{\mathbf{x}}$ which is same as the direction of applied magnetic field and crystal in-plane easy axis. The current is sent across the pillar in the $\hat{\mathbf{z}}$ direction which is same as the direction of demagnetizing field, $\mathbf{H}_{demag}$.

Apart from the more obvious application as plain memory storage devices, many spin valve based magneto-logic devices have been attempted in the recent past. FIMS based field programmable logic gates using GMR elements were proposed by Hassoun *et al.*(Hassoun et al., 1997), wherein the type of the logical operation to be performed can be altered by additional fields. Further models have also been suggested where the logical state of the GMR unit is manipulated using FIMS (Richter et al., 2002;

Ney et al., 2003; Ney and Harris, 2005; Wang et al., 2005; Lee et al., 2007). Similar programmable models based on spin valve magneto-logic devices are also known in literature(Zhao et al., 2007; Dery et al., 2007). These later models, based on CIMS, involve additional spin-valve elements that together form a single logical unit, or more than one current carrying plate capable of generating fields in orthogonal directions. Besides, in these models, bi-polar currents were crucial in writing or manipulating data. Invariably, this requires a more complex architecture than is required for a simple magnetic memory unit. In this chapter we propose alternative magneto-logic gate designs for both universal as well as non-universal gates, wherein the logical operation is performed through CIMS in the presence of a controlling field. Apart from the simplicity in the architecture, the models also carry the advantage that they can be used as plain memory elements in a MRAM. They consist of a single spin-valve pillar and no additional elements, than those required for its functioning as a memory unit, are required to enhance its role as a logical gate. In the proposed models we use STT for writing, while the magnetic field is held constant in magnitude (though polarily may change depending on the logic gate) and required only during the logical operation. Thus the applied field acts as a control switch for the gates. Moreover, as we will show in this chapter the logic gate is *non-volatile* and has sub-nano second operation time.

3.3 Spin valve pillar geometry and the governing Landau-Lifshitz-Gilbert equation

The nanopillar geometry is schematically illustrated in figure (3.1. We use the same device geometry for universal as well as non-universal gate designs. The pinning direction is $\hat{\mathbf{x}}$ which is same as the direction of applied magnetic field and crystal in-plane easy axis. The current is sent across the pillar in the $\hat{\mathbf{z}}$ direction which is same as the direction of demagnetizing field, $\mathbf{H}_{demag}$.

The dynamics of the macrospin magnetization of the free layer is governed by the Landau-Lifshitz-Gilbert (LLG) equation with the STT term, whose dimensionless form is given by equation (2.18). Since we will be constantly referring back to this equation,

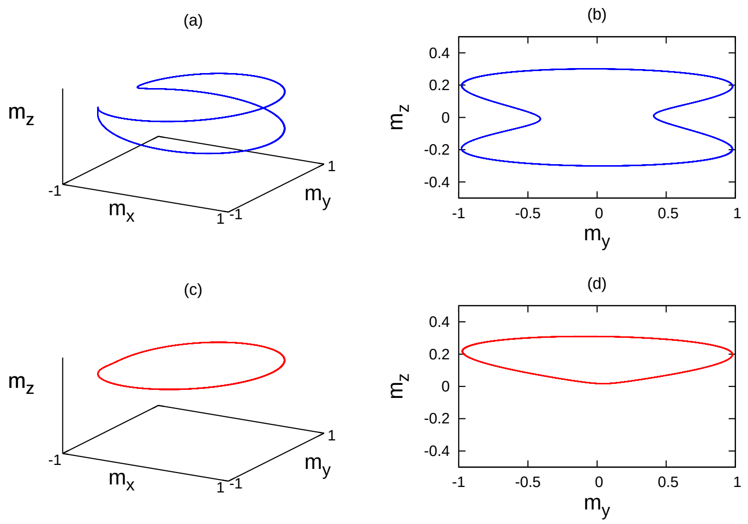

Figure 3.2: The in-plane (IP) and out-of-plane (OOP) regimes of magnetization precession in spin valves. (a) The in-plane (IP) precession is a symmetric precession visiting both the hemispheres of S^2. (b) Projection of the IP trajectory onto the $y - z$ plane. (c) The out-of-plane (OOP) precession spontaneously breaks the symmetry and is confined to either of the hemispheres depending on the initial condition (here confined to the northern hemisphere). (d) Projection of the OOP trajectory onto the $y - z$ plane.

it is reproduced here for quick reference:

$$\frac{\partial \mathbf{m}}{\partial t} - \alpha \mathbf{m} \times \frac{\partial \mathbf{m}}{\partial t} = \mathbf{m} \times \left(\mathbf{h}_{eff} - \beta \frac{\mathbf{m} \times \mathbf{e}_p}{1 + c_p \mathbf{m} \cdot \mathbf{e}_p} \right) . \tag{3.1}$$

The free-layer magnetization $\mathbf{m}$ and the effective field $\mathbf{h}_{eff}$ are normalized by the saturation magnetization M_s. Time is measured in units of $(\gamma M_s)^{-1}$, where γ is the gyromagnetic ratio (for Co layers, this implies time scales in the order of picoseconds). The constant α is the damping factor and unit vector $\mathbf{e}_p$ is the direction of pinning ($\hat{\mathbf{x}}$ in our case, and in plane). The other constant c_p $(1/3 \leq c_p \leq 1)$ is a function of degree of spin polarization P $(0 \leq P \leq 1)$ given by equation (2.19). In the numerical calculations that follow we have used the typical value of $P = 0.3$. The phase diagrams, to be discussed in the next section, do exhibit minor variations with change in the value of P, but do not alter our results much. For, as can be seen from equation (2.19), c_p is a small number compared to 1 for all realistic values of P. The parameter β is proportional to the spin current density (typically of the order of 10^{-2} for Co layers, with current densities $\sim 10^8$ A/cm^2). The effective field, specific to geometry defined in figure (3.1) is given by:

$$\mathbf{h}_{eff} = h_{ax}\hat{\mathbf{x}} - (D_x m_x \hat{\mathbf{x}} + D_y m_y \hat{\mathbf{y}} + D_z m_z \hat{\mathbf{z}}),$$

where $h_{ax}\hat{\mathbf{x}}$ is the external field and D_is$(i = x, y, z)$ are constants that reflect the crystal shape and anisotropy effects. Particularly, we chose our film such that the anisotropy is in-plane, and also lies along the x-axis. The plane of the free layer is chosen to be the $x - y$ plane. With this choice $D_i s$ are such that $D_x < D_y < D_z$, making $\hat{\mathbf{x}}$ the free-layer easy axis.

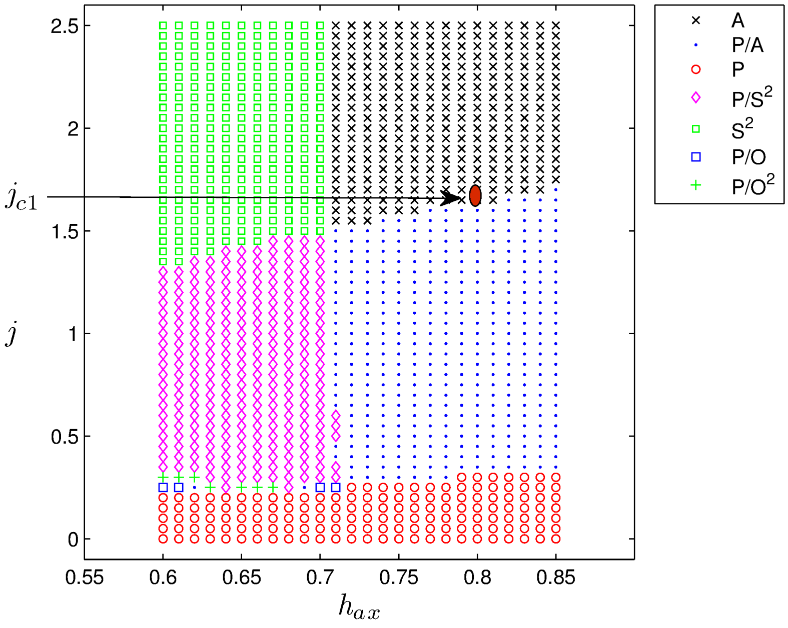

Figure 3.3: Phase diagram in the $h_{ax} - j$ space, in regions relevant for the NOR gate. The system displays in-plane limit cycles(O), out-of-plane limit cycles (O^2), stable fixed points parallel to $\hat{\mathbf{x}}$ (P) or $-\hat{\mathbf{x}}$ (A), and out-of-plane stable fixed points (S^2). The critical value of the current and the field used for our model (j_{c1}) is circled in the figure.

3.4 Universal magneto-logic gates

For our choice of geometry, described in the previous section, the magnetization in the free layer exhibits a variety of dynamics in different regions of the $h_{ax} - j\,(\equiv\, \beta/\alpha)$ parameter space - such as in-plane limit cycles (O) and symmetric out-of-plane limit cycles (O^2), and stable fixed points parallel to $\hat{\mathbf{x}}$ (P), parallel to $-\hat{\mathbf{x}}$ (A) and symmetric out-of-plane stable fixed points (S^2)(Bertotti et al., 2005). The difference between in-plane limit cycles and out-of-place limit cycles are depicted in figure (3.2). The in-plane (IP) precession is a large angle precession approximately confined to the plane of anisotropy visiting both the hemispheres symmetrically, whereas the approximately circular out-of-plane (OOP) precession spontaneously breaks this symmetry and is confined to either of the hemispheres depending on the initial condition. This typically happens with increasing the magnitude of the current or in equation (3.1), the magnitude of β. The general behaviour of STNO is that, the frequency of IP precession decreases monotonously with increasing the dc current until the onset of OOP precession regime, after which frequency monotonously increase with increasing dc current(Grollier et al., 2006; Kiselev et al., 2003). We will explore this in greater detail on the next chapter. In figure (3.3) we show a specific portion of the parameter space of our model equation where the logic NOR gate we propose can perform the desired logical operation. The type of dynamics in the different regions of the parameter space is identified here by numerically simulating the LLGS equation (3.1).

3.4.1 Geometry of fixed points

For the logical NOR gate, we shall choose the applied field (whenever non-zero) to be positive and $|h_{ax}| > D_z - D_x$. For this choice, there can at best be only one stable fixed point, lying along either $\pm\hat{\mathbf{x}}$ directions depending on the values of h_{ax} and j(Bertotti et al., 2009). For a given set of values of the system parameters, D_is and α, fixed points corresponding to four scenarios of special interest to us in designing our NOR gate are shown in figure (3.4). When j is held below a certain threshold value, and $|h_{ax}| > D_z - D_x$, $\mathbf{m} = \hat{\mathbf{x}}$ is the only stable fixed point, while $-\hat{\mathbf{x}}$ is unstable. For j beyond a certain upper threshold value j_{c1}, with h_{ax} held at the same value, the

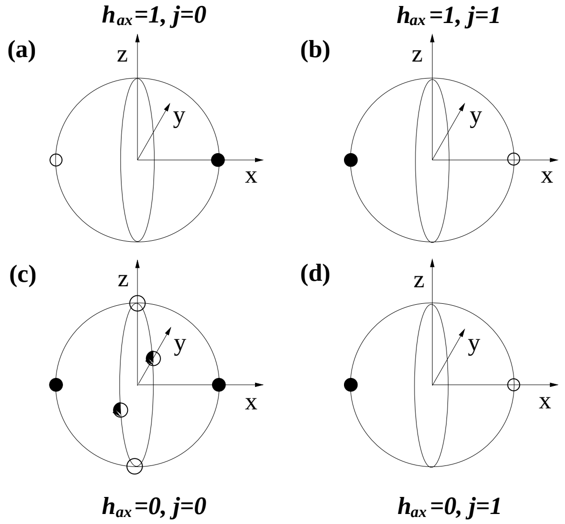

Figure 3.4: Fixed point illustration for NOR gate. Fixed points for four different cases. For convenience, we have indicated the fixed value of the applied field we have used through out, satisfying the condition $|h_{ax}| > D_z - D_x$, as h_{ax} =1. Similarly the value for $j\ (> j_{c1})$, is indicated by $j = 1$. (a) $h_{ax} = 1,\ j = 0$, (b) $h_{ax} = 1,\ j = 1$, (c) $h_{ax} = 0,\ j = 0$, and (d) $h_{ax} = 0,\ j = 1$. Stable fixed points are indicated by filled dots, and unstable fixed points by unfilled dots. For $h_{ax} = 0 = j$, there arise six fixed points, two of which are saddles indicated by half filled dots, and both $\pm\hat{\mathbf{x}}$ are stable fixed points.

situation reverses, with $\hat{\mathbf{x}}$ becoming unstable and $-\hat{\mathbf{x}}$ becoming the stable point. When $h_{ax} = 0 = j$, both $\pm\hat{\mathbf{x}}$ become stable on account of the anisotropy field along the $\mathbf{x}$ axis. Finally, when h_{ax} is held at zero, but $j > j_{c1}$, the scenario in figure 3.4 (b) repeats, with $-\hat{\mathbf{x}}$ stable and $\hat{\mathbf{x}}$ unstable.

A numerical simulation of the governing LLGS equation (3.1), shows the expected magnetization switching in conformity with figure (3.5). We choose the system parameters $\alpha = 0.01$, $D_x = -0.034$, $D_y = 0$, and $D_z = 0.68$ (as in (Kiselev et al., 2003)). Taking the value of saturation magnetization, M_s, to be that of Co ($1.4 \times\ 10^6$ A/m), it effectively implies a time scale of 3.2 ps. The switching time due to the spin-current is roughly 0.2 ns, while that due to the magnetic field is slower, at nearly 0.7 ns, accompanied by a ringing effect. This delay and ringing effect are well understood to be due

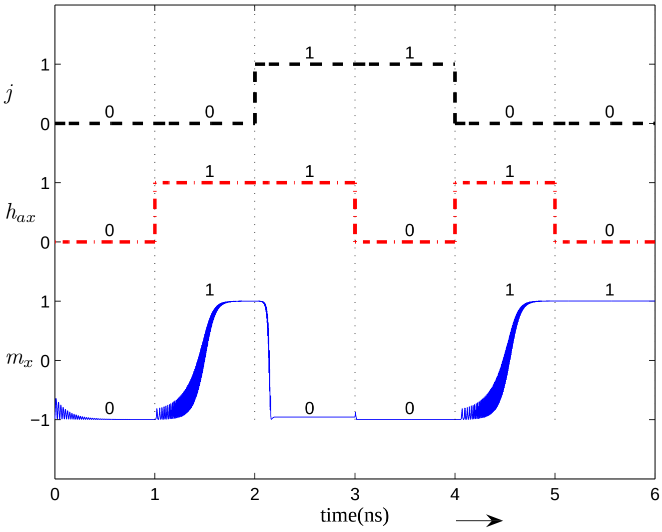

Figure 3.5: Time evolution of m_x (bottom) as the applied field h_{ax} (middle) and j (top) are flipped through various combinations, with the interpreted logical state. The initial orientation of $\mathbf{m}$ is chosen arbitrarily. For the case $h_{ax} = 0 = j$, both $\pm\hat{\mathbf{x}}$ are stable fixed points, and the magnetization relaxes to the nearest of the two directions- $m_x = -1$ initially, and $m_x = +1$ finally.

to the fact that, even with $\alpha = 0$, a spin-transfer-torque leads to both precession and dissipation whereas a magnetic field alone can only cause a precession of magnetization vector about the applied field(Murugesh and Lakshmanan, 2009). Field induced switching is thus exclusively due to the damping factor, leading to a longer switching time, consequently. A longer switching time invariably implies more precession meanwhile, causing the ringing effect. In figure (3.5), we show the dynamics of the x component of the normalized magnetization vector $\mathbf{m}$ as the field and current are switched through various possible combinations. The current density used is of the order of 10^8 A/cm^2, and the field h_{ax} is of the order of 10^6 A/m. Such a magnitude for the applied field, although frequently used (see, for instance (Kiselev et al., 2003)), is substantially high for real world applications. Magnetic tunnel junctions (MTJs) have proved themselves to be more worthwhile candidates as MRAMs, with their operability at much lower spin-current and field amplitudes, and higher ferromagnetic to anti-ferromagnetic current ratios(Kalitsov et al., 2009; Parkin et al., 2003; Daughton, 1997). Although the STT

h_{ax}	j_1	j_2	$\mathbf{m}$ (logical state)
1	0	0	$\hat{\mathbf{x}}$ (1)
1	1	0	$-\hat{\mathbf{x}}$ (0)
1	0	1	$-\hat{\mathbf{x}}$ (0)
1	1	1	$-\hat{\mathbf{x}}$ (0)

Table 3.1: The truth table for NOR gate. The applied field is always held constant through out the operation ($|h_{ax}| > D_z - D_x$) indicated by $h_{ax} = 1$. The currents $j_{1,2}$ take either a value greater than j_{c1}, indicated as the logical input 1, or zero taken as input 0.

phenomenon in MTJs and that in spin-valve pillars display several qualitative similarities, MTJs are hampered by the lack of an appropriate mathematical model to describe their dynamics. We believe results presented in this paper will be of relevance in MTJs too and may possibly be reproduced. Our numerical simulations show that the model presented is robust with respect to errors that may creep in through two of the system parameters - variations in the degree of polarization, and in plane anisotropy fields in the form of D_x. We have varied these values upto 10% and yet noticed no perceivable difference in the phase diagram. The chosen values of $j_i's$ $(0.6j_{c1})$ provides enough room for errors arising out of fluctuations. Further, we recall that as long as the condition $|h_{ax}| > D_z - D_x$ is satisfied we have the two desired fixed points, enabling the required logical operation.

3.4.2 Logic NOR gate

We make use of the first three scenarios (figure 3.4 (a)-(c)) to construct the universal NOR gate, which retains the non-volatility of spin based memory devices. Let j_1 and j_2 be currents that form inputs to the logic gate, and each take either of the two values - *zero*, or some value j little over j_{c1}. We shall identify these values of the current with the logical input states 0 and 1, respectively. Both currents j_1 and j_2 are fed together into the spin-valve from the pinned layer end. The field h_{ax} is held fixed throughout the logical operation (represented henceforth simply as h_{ax} =1), and acting as a controlling

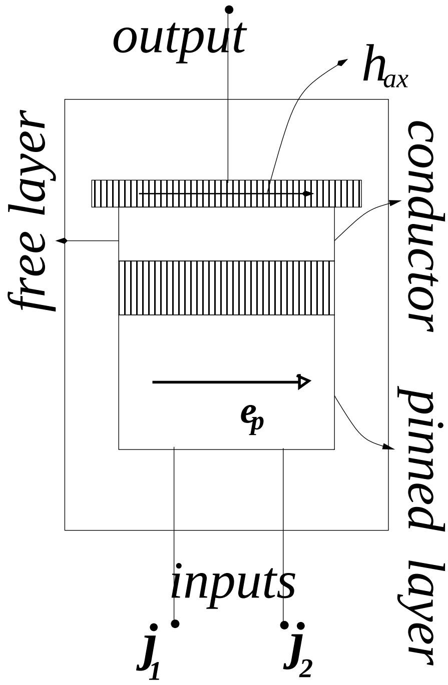

Figure 3.6: A schematic diagram of the NOR gate, with the relevant portion of the spin-valve pillar with the input currents $j_i' s$ and the control field h_{ax}. The logical output is interpreted from the value of the potential V_{out}, either high (state 1) or low (state 0).

field. When the currents $j_{1,2}$ are both zero, the magnetization $\mathbf{m}$ orients itself along $\hat{\mathbf{x}}$, the only stable fixed point. This corresponds to the low resistance state, being *parallel* to the pinned layer magnetization, which we read as the logical state 1. When either, or both, of the currents $j_{1,2}$ is greater than j_{c1}, the torque is sufficient enough to flip the spin $\mathbf{m}$ from any direction to the new stable fixed point $-\hat{\mathbf{x}}$ (the high resistance *anti-parallel* state 0). The truth table of the NOR gate is thus obtained (see table 3.1). When the field h_{ax} and the currents $j_{1,2}$ are all switched off, both $\pm\hat{\mathbf{x}}$ are equally good stable fixed points due to the anisotropy field along the $\mathbf{x}$ axis. Prior value of magnetization is therefore retained, and the gate carries the non-volatility of the MRAM. The nature of fixed points depicted in figure 3.4 (a), (c), (d), show that the same valve assembly can also be used as a plain memory device. To this end we shall use a single current input, j, to the spin-valve as opposed to the two inputs for the gate assembly. *Writing* the data bit 1 is then enabled with a applied field $h_{ax} = 1$ and current $j = 0$. Similarly the bit 0 is written when $h_{ax} = 0$ and $j = 1$. The two stable fixed points, as shown

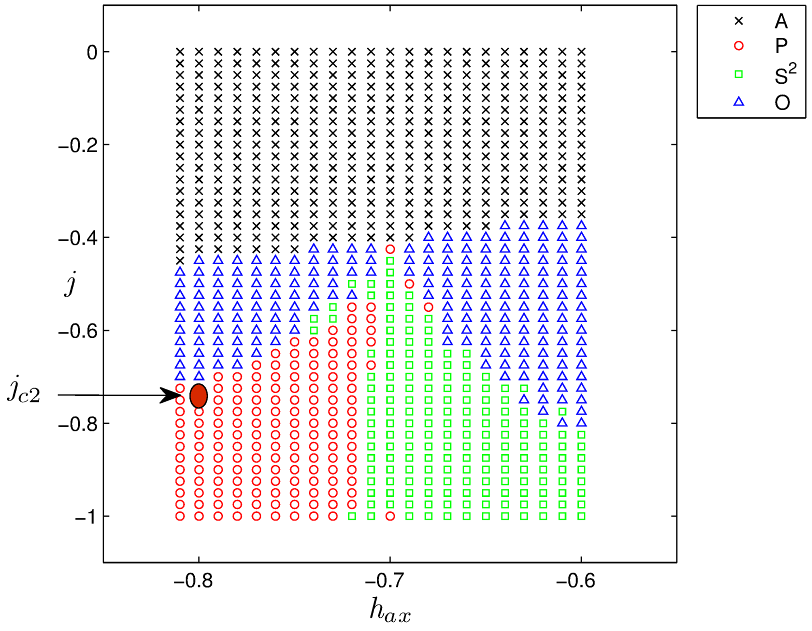

Figure 3.7: Phase diagram in the $h_{ax} - j$ space, in regions relevant for the NAND gate. The system displays in-plane limit cycles(O), stable fixed points parallel to $\hat{\mathbf{x}}$ (P) or $-\hat{\mathbf{x}}$ (A), and out-of-plane stable fixed points (S^2). The critical value of the current and the field used for our model (j_{c2}) is circled in the figure.

in figure 3.4 (c), then ensure that the magnetization, or *data*, is retained in the absence of both the current and field, preserving non-volatility. A schematic representation of the logical NOR gate for a choice of input currents, and with control field $h_{ax} = 1$, is shown in figure (3.6).

3.4.3 Logic NAND gate

We now look at the fixed points corresponding to another region of the $h_{ax} - j$ parameter space [figure (3.7)]. The applied field h_{ax} is chosen to be *negative* (again, whenever non-zero), while still satisfying the earlier condition that $|h_{ax}| > D_z - D_x$, and the current j assumes either of the three values, *zero*, $0.6j_{c2}$ or $1.2j_{c2}$ [where j_{c2} is indicated in figure (3.7)]. Notice that j_{c2} is *negative*, implying a current sent in the opposite direction along the pillar. The fixed points corresponding to different combinations of h_{ax} and

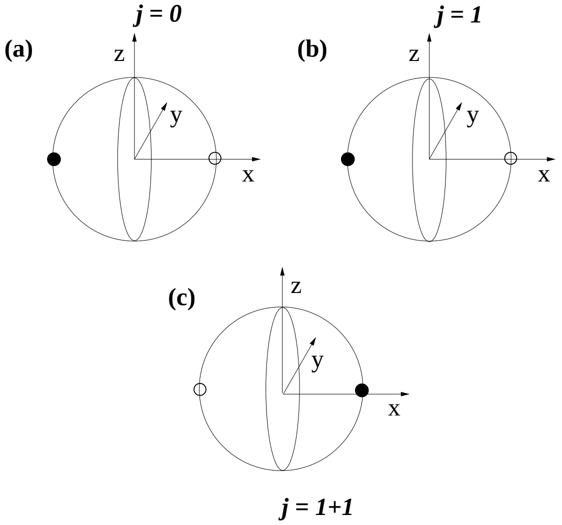

Figure 3.8: Fixed point illustration for NAND gate. Fixed points for three different values of the current j, (a) $j = 0$, (b) $j = 1\,(0.6j_{c2})$ and (c) $j = 1{+}1\,(1.2j_{c2})$. The applied field h_{ax} is the same, and is negative with $|h_{ax}| > D_z - D_x$. When both field and current are zero, the fixed points are the same as in figure 3.4 (c).

j are shown in figure (3.8). We shall denote the above mentioned negative value of the magnetic field as $h_{ax} = -1$. For the NAND gate we shall take the current value $j = 0$, and $j = 0.6j_{c2}$ as the logical inputs 0 and 1, respectively. In the absence of both current and field, the stable fixed points are $\pm\hat{\mathbf{x}}$, as in figure 3.4 (c). When the field $h_{ax} = -1$ and the current is either 0 or 1, $\hat{\mathbf{m}} = -\hat{\mathbf{x}}$ is the only stable fixed point while $\hat{\mathbf{m}} = \hat{\mathbf{x}}$ becomes unstable. When the current value $j = 1.2j_{c2}$, however, the situation reverses, with $\hat{\mathbf{x}}$ becoming stable, and $-\hat{\mathbf{x}}$ unstable. A numerical simulation, analogous to figure (3.5), for these new values of h_{ax} and j is shown in figure (3.9), with results as expected. As in the case of the NOR gate, let j_1 and j_2 be the currents fed together, and each take values 0 or 1 (now corresponding to negative currents). The magnetic field is held constant at $h_{ax} = -1$ all along the logical operation. For the logical NAND gate we adopt the opposite convention, interpreting the high-resistance state ($\hat{\mathbf{m}} = -\hat{\mathbf{x}}$) as the logical state 1, and the low-resistance state as 0. The truth table of the NAND operation is thus realized (table 3.2). As both $\pm\hat{\mathbf{x}}$ are stable fixed points in the absence of current and magnetic field [figure 3.4 (c)], non-volatility is ensured.

In summary, we have proposed spin-valve based magneto-logic NOR and NAND

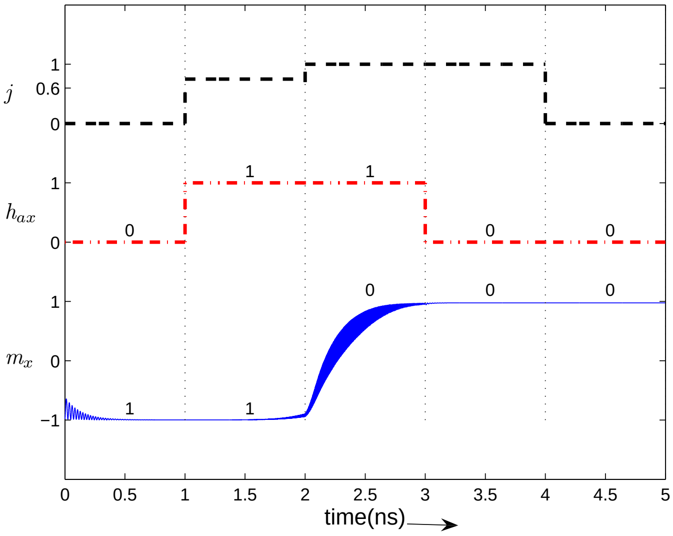

Figure 3.9: Time evolution of m_x (bottom) as the applied field h_{ax} (middle) and j (top) are flipped through various combinations, relevant to the NAND gate. The interpreted logical state is indicated over the respective m_x values. For the parameter values chosen, the switching time is within 1 ns.

gate assemblies, which render themselves to the dual role of universal gate and a magnetic memory. A constant applied magnetic field parallel to the pinned layer magnetization acts as a control for the logic gate operation, while spin-currents are fed in as the logical inputs. The same pillar geometry is used for both the NOR and NAND gates, and also doubles as a magnetic memory device. We also demonstrated the robustness of our model against current fluctuations as well as changes in the degree of spin polarization. We also see two ailments of the proposed design, which can hamper the practical implementation of our model to a significant extent. First and foremost is the *redefinition* problem. The model we proposed is of a programmable gate, but while changing its operation from logic NOR to logic NAND we had to re-interpret the high-resistance state ($\hat{\mathbf{m}} = -\hat{\mathbf{x}}$) as the logical state 1, and the low-resistance state as 0. This is opposite of the convention we used for the logic NOR. Secondly the magnitude of critical value of current (not just its polarity) changes while changing the logic operation of the gate. Both of these issues can pose certain engineering challenges while implementing our model in practice. In the next Section, we propose model magneto-logic non-universal

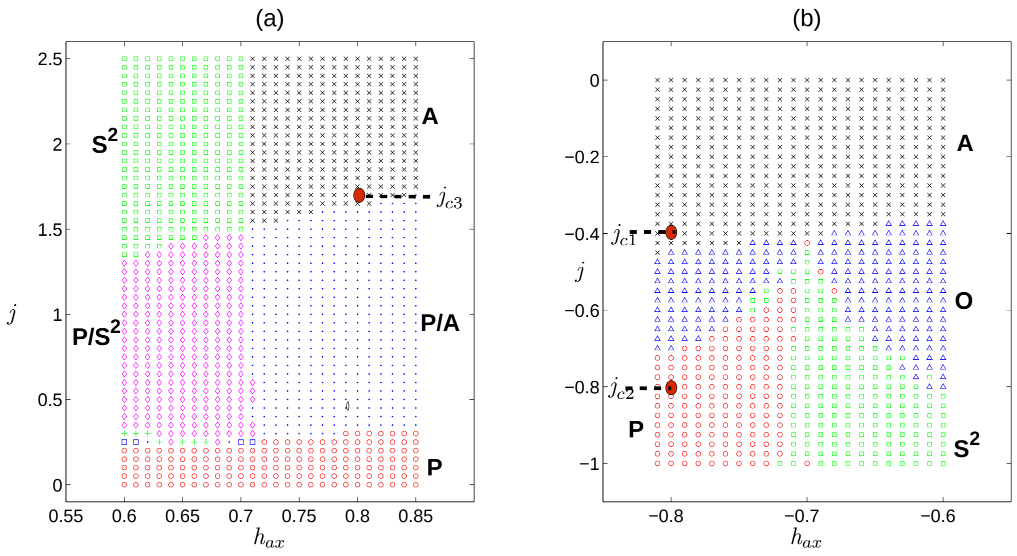

Figure 3.10: Phase diagram in the $h_{ax} - j$ space, in regions relevant for the (a) NOT and (b) AND and OR gates. The system displays limit cycles(O), symmetric out-of-plane limit cycles (O^2), stable fixed points parallel to $\hat{\mathbf{x}}$(P) or $-\hat{\mathbf{x}}$(A), and symmetric out-of-plane stable fixed points (S^2). The critical value of the current and the field used for our models (j_{c1}, j_{c2} and j_{c3}) are circled in the two figures.

OR,AND and NOT gates using essentially the same nanopillar geometry. We show that the *redefinition* problem is completely avoided while implementing these non-universal gates.

3.5 Non-universal magneto-logic gates

In this section, we develop model non-universal gates, which solves the *redefinition* problem suffered by their universal counterparts. For our choice of geometry, described in the previous section, the magnetization in the free layer exhibits a variety of dynamics as earlier (see figures (3.3) and (3.7)). In figure (3.10) we show two specific ranges where the models we propose can perform the desired logical operations. The critical value of the current and the field used for our models (j_{c1}, j_{c2} and j_{c3}) are circled in the figure 3.10 (a) and (b).

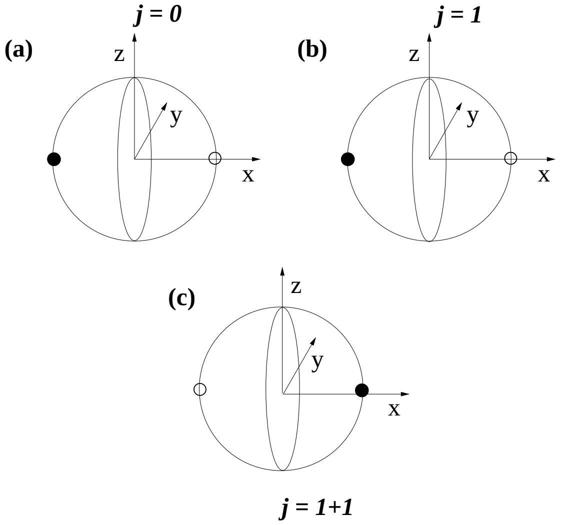

Figure 3.11: Fixed point illustration for AND gate. Fixed points for three different values of the current j, (a) $j = 0$, (b) $j = 1\,(j_{c1})$ and (c) $j = 1 + 1\,(2j_{c1})$. The applied field h_{ax} is the same, and is negative with $|h_{ax}| > D_z - D_x$ which is represented by h_{ax} =1. Both the currents should be 'high' in order to have a 'high' output.

3.5.1 Logic AND gate

For the logical AND gate design consider the fixed points corresponding to a specific negative region of $h_{ax} - j$ parameter space [figure 3.10 (b)]. The applied field h_{ax} is chosen to be *negative* (whenever non-zero) and and $|h_{ax}| > D_z - D_x$. For this choice, there can at best be only one stable fixed point, lying along either $\pm\hat{\mathbf{x}}$ directions depending on the values of h_{ax} and j. The spin current j assumes either of the three values, *zero*, j_{c1} or $2.0j_{c1}$ [where j_{c1} is indicated in figure 3.10 (b)]. The currents used in the simulations are atleast 1% higher than the critical currents to ensure the robustness of the device against random noises. Notice that j_{c1} is *negative*, implying a current sent in the opposite direction along the pillar. The fixed points corresponding to different combinations of h_{ax} and j are shown in figure (3.11). We shall denote the above mentioned negative value of the magnetic field as $h_{ax} = -1$. Also we shall take the current value $j = 0$, and $j = j_{c1}$ as the logical inputs 0 and 1, respectively. In the absence of both current and field, the stable fixed points are $\pm\hat{\mathbf{x}}$. When the field $h_{ax} = -1$ and the current is either 0 or 1, $\hat{m} = -\hat{\mathbf{x}}$ is the only stable fixed point while $\hat{m} = \hat{\mathbf{x}}$ be-

h_{ax}	j_1	j_2	$\mathbf{m}$ (logical state)
-1	0	0	$-\hat{\mathbf{x}}$ (1)
-1	1	0	$-\hat{\mathbf{x}}$ (1)
-1	0	1	$-\hat{\mathbf{x}}$ (1)
-1	1	1	$\hat{\mathbf{x}}$ (0)

Table 3.2: The truth table for NAND gate. As earlier, the applied field is always held constant through out the operation, though negative. The currents $j_{1,2}$ take either of the two values $0.6j_{c2}$ - the logical input 1, or zero taken as input 0.

h_{ax}	j_1	j_2	$\mathbf{m}$ (logical state)
-1	0	0	$-\hat{\mathbf{x}}$ (0)
-1	1	0	$-\hat{\mathbf{x}}$ (0)
-1	0	1	$-\hat{\mathbf{x}}$ (0)
-1	1	1	$\hat{\mathbf{x}}$ (1)

Table 3.3: The truth table for AND gate. The applied field is always held constant through out the operation ($|h_{ax}| > D_z - D_x$) indicated by $h_{ax} = -1$. The currents $j_{1,2}$ take either a value greater than j_{c1}, indicated as the logical input 1, or zero taken as input 0.

comes unstable. When the current value $j = 2.0j_{c1}$ (but same applied field), however, the situation reverses, with $\hat{\mathbf{x}}$ becoming stable, and $-\hat{\mathbf{x}}$ unstable. Let j_1 and j_2 be the currents fed together, and each take values 0 or 1. The magnetic field is held constant at $h_{ax} = -1$ through out the logical operation. When the free layer magnetization is parallel to the direction of pinning magnetization, we have a low resistance state due to the GMR effect and vice versa. We interpret the high-resistance state ($\hat{m} = -\hat{\mathbf{x}}$) as the logical state 0, and the low-resistance state ($\hat{m} = \hat{\mathbf{x}}$) as the logical state 1 (consistency of this convention is preserved in all the gates). The truth table of the AND operation is thus realized (table 3.3). As both $\pm\hat{\mathbf{x}}$ are stable fixed points in the absence of current and magnetic field, non-volatility is ensured. Figure (3.12) shows the expected response

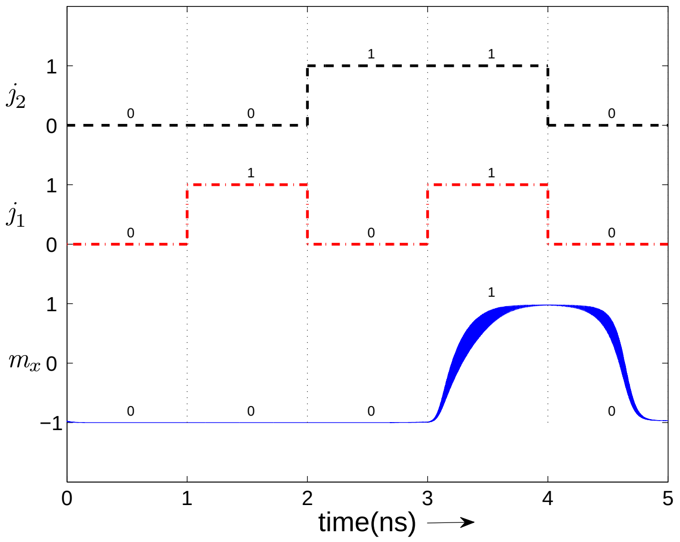

Figure 3.12: Time evolution of m_x (bottom) as the applied currents j_1 (middle) and j_2 (top) are flipped through various combinations, relevant to the AND gate. The interpreted logical state is indicated over the respective m_x values. For the parameter values chosen, the switching time is within 1 ns.

of the free layer magnetization to the flipping of input current j_i's.

3.5.2 Logic OR Gate

We again consider the region of parameter space we used for logic AND gate [figure 3.10 (b)], but we now identify another critical current density value denoted by j_{c2} which can be used for implementing the logic OR gate. Again the applied field h_{ax} is chosen to be *negative* (whenever non-zero) and and $|h_{ax}| > D_z - D_x$. Now the spin current j assumes either of the three values, *zero*, j_{c2} or $2.0j_{c2}$ [Again, j_{c2} is indicated in figure 3.10 (b)]. The fixed points corresponding to different j values are shown in figure (3.13). We shall take the current value $j = 0$, and $j = j_{c2}$ as the logical inputs 0 and 1, respectively. In the absence of both current and field, the stable fixed points are $\pm\hat{\mathbf{x}}$. When the field $h_{ax} = -1$ and the current j_i =0, $\hat{m} = -\hat{\mathbf{x}}$ is the only stable fixed point while $\hat{m} = \hat{\mathbf{x}}$ becomes unstable. When either of the input current value j_i =1 ($j_i = 1.0j_{c2}, i = 1, 2$), the situation reverses, with $\hat{\mathbf{x}}$ becoming stable, and $-\hat{\mathbf{x}}$ unsta-

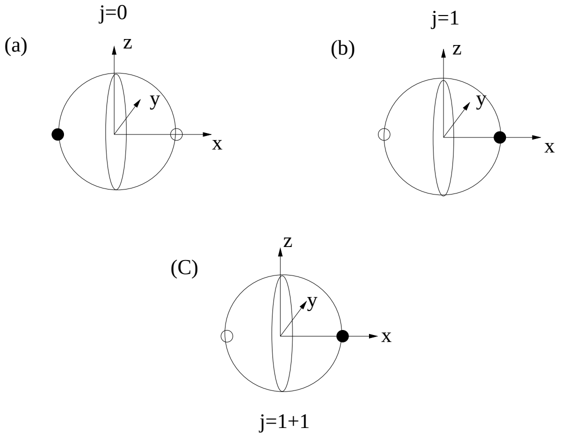

Figure 3.13: Fixed point illustration for OR gate. Fixed points for three different values of the current j, (a) $j = 0$, (b) $j = 1\,(j_{c2})$ and (c) $j = 1 + 1\,(2j_{c2})$. The applied field is the same as in figure (3.11). It is seen that a single 'high' input current drives the output to a 'high' state.

ble. The same scenario repeats with the current value j =1+1 ($j = 2.0j_{c2}$) realizing a magneto-logic OR gate. The truth table of magneto-logic OR gate is shown in the table 3.4, and numerical results for the flipping of x-component of free layer magnetization is shown in figure (3.14).

3.5.3 Logic NOT gate

In order to realize the logic NOT gate, we turn our attention to the selected positive side of the $h_{ax} - j$ control space shown in figure 3.10 (a). Now h_{ax} is held at the same numerical value as earlier but now in the $+\hat{\mathbf{x}}$ direction denoting $h_{ax} = 1$ in the following discussion. We use the critical current density denoted by j_{c3} in the figure 3.10 (a) to realize the NOT gate. The spin current density $j > j_{c3}$, but within the same dynamic regime in phase space, is denoted by j =1. From the nature of fixed points illustrated in figure (3.15), it is clear that whenever the current density toggles from logical values $j = 0$ to $j = 1$, the nature of stability interchanges between the two fixed points $\hat{\mathbf{x}}$ and $-\hat{\mathbf{x}}$, and vice-versa. With our interpretation of $+\hat{\mathbf{x}}$ as logical state 1 and $-\hat{\mathbf{x}}$ as state 0, we have an immediate realization of NOT gate (See table 3.5 for the truth table).

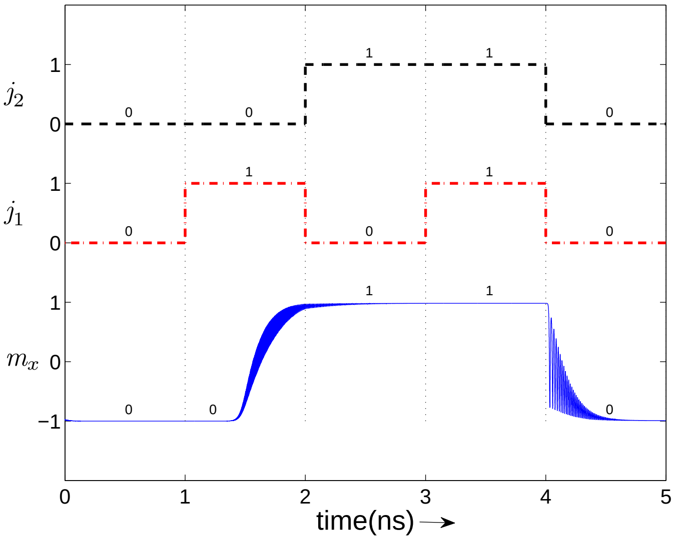

Figure 3.14: Time evolution of m_x (bottom) as the applied currents j_1 (middle) and j_2 (top) are flipped through various combinations, relevant to the OR gate. The interpreted logical state is indicated over the respective m_x values. For the parameter values chosen, the switching time is within 1 ns.

3.6 Outlook

Here we give a quick summary of the logic gate designs proposed in this chapter. The fundamental idea is to bring about an *exchange of stability* bifurcation by tuning the current through the nanopillar device. For digital applications, we need to discretize the input current values, either zero or above a well-defined critical value $j_{critical}$. The current values, $j > j_{critical}$, either switches the magnetization or leave it intact depending upon the region of parameter space under use. This is in turn modified using the polarities of *control* field and current itself. These ideas are based on a well tested theoretical model for a single domain ferromagnet of nanometer size. Using modern fabrication techniques it is indeed possible to fabricate patterned single domain nanomagnets. This fact should be encouraging enough for experimentalists to actually test our model. There is significant reduction of complexity and material cost compared to other proposed models of magneto-logic gates in the literature. The success of our model will be largely determined by the width of individual dynamical regions in the

h_{ax}	j_1	j_2	$\mathbf{m}$ (logical state)
-1	0	0	$-\hat{\mathbf{x}}$ (0)
-1	1	0	$-\hat{\mathbf{x}}$ (1)
-1	0	1	$-\hat{\mathbf{x}}$ (1)
-1	1	1	$\hat{\mathbf{x}}$ (1)

Table 3.4: The truth table for OR gate. The applied field is always held constant through out the operation ($|h_{ax}| > D_z - D_x$) indicated by $h_{ax} = -1$. The currents $j_{1,2}$ take either a value greater than j_{c2}, indicated as the logical input 1, or zero taken as input 0.

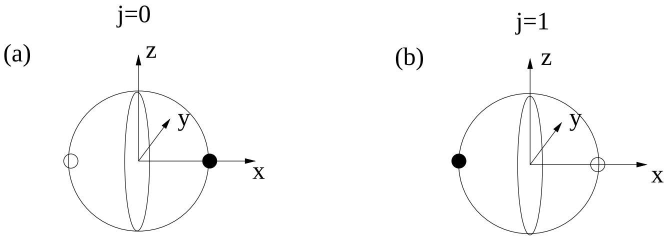

Figure 3.15: Fixed point illustration for NOT gate. (a) $j = 0$ and (b) $j = 1\,(j_{c3})$. The applied field is the same as figure (3.11) in magnitude but is now pointing in the $+\hat{\mathbf{x}}$ direction denoted by h_{ax} =1. It is seen that a 'high' input current drives the output to a 'low' state realizing NOT gate.

relevant control plane (see, for example, figure (3.3)). Well separated dynamical regions provide robustness to the device. But as seen in the early experiments, all the dynamical regions predicted by single domain theory are not successfully reproduced in experiments. For example, Kiselev et. al. reported that the out-of-plane (OOP) precession mode (O^2) predicted by the LLGS equation is not observed in their experiments, instead there was a state with resistance in between P and AP state accompanied by only small microwave signals(Kiselev et al., 2003). It is conjectured that in this region, denoted by W, the single-domain approximation becomes invalid owing to dynamical instabilities. In this region different regions of the sample are inferred to move incoherently, giving total time dependant resistance changes much smaller than for single-domain motion.

h_{ax}	j	$\mathbf{m}$ (logical state)
1	0	$+\hat{\mathbf{x}}$ (1)
1	1	$-\hat{\mathbf{x}}$ (0)

Table 3.5: The truth table for NOT gate. The applied field is once again held constant through out the operation ($|h_{ax}| > D_z - D_x$), indicated by $h_{ax} = 1$. The current j take either a value greater than j_{c3}, indicated as the logical input 1, or zero taken as input 0.

We will talk more about the breakdown of single domain approximation in chapter 5.

Once a nanomagnet possessing the right phase portrait characteristics is fabricated, our model guarantees a robust and error free performance as shown earlier in this chapter. This would be more of an exercise in choosing the right materials, fabrication techniques and device dimensions rather than an exercise in fundamental device physics. The salient features of the proposed model universal and non-universal gates are summarized below:

1. Simplicity of architecture as compared to other proposed models of CIMS based magneto-logic gates (requires a single spin-valve pillar in CPP geometry)
2. The same spin valve assembly be used as both logic gate and MRAMs
3. Programmable logic—The logic operation can be changed by reversing the sign of current and the controlling magnetic field.
4. Model is non-volatile with switching time in nanoseconds
5. Functionally robust with respect to current fluctuations as well as changes in the degree of spin polarization.

We also see that the *redefinition* problem suffered by the universal gates are mitigated by the non-universal gates. The critical current densities, used to represent logical input, are different for each type of gate. There is, however, consistency in the interpretation of the logical inputs and outputs, with respect to the direction, or sign, of the current densities.

In the next chapter we leave the fixed point dynamics behind and focus almost exclusively on the *limit cycle* dynamics. This brings us to the exciting area of spin-torque nano oscillators (STNO).

CHAPTER 4

SPIN TORQUE NANO OSCILLATORS

> *“In all chaos there is a cosmos, in all disorder a secret order."*
>
> — Carl Gustav Jung

4.1 Introduction

Spin torque nano oscillators (STNO) represents a paradigm shift in the age of nanotechnology and spintronics. As we have shown in chapter 2, the self-sustained oscillations in nano-pillar devices can be understood in terms of the balance between the torque generated by the damping forces and the spin transfer torque which acts in opposite direction to the former. These spin-torque nano-oscillators (STNOs), whose oscillations are in microwave range (frequency in GHz), are excellent candidates for oscillators to be integrated into a spintronics motivated architecture. The steady-state magnetic precession mode that can be excited by spin transfer is under investigation for a number of high-frequency applications, for example nanometer-scale frequency-tunable microwave sources, detectors, mixers, and phase shifters. Another potential area of use is for short range chip-to-chip or even within-chip communications. Some notable features of STNOs are summarised below:

- Nanometer in size and GHz in frequency.
- Smallest self-oscillation known in nature.
- Broad working temperature.
- Low power dissipation
- Narrow linewidth

- Ultra low critical current
- Microwave emission at *zero field*

However, very feeble microwave power output from a single STNO ($\sim 1\,\mathrm{nW}$) remains the main practical problem, in terms of their desired spintronic applications. Various coupling schemes to enhance the output power of a set of such STNOs have been proposed in the last few years.

Coupling of nonlinear oscillatory systems can reveal several interesting phenomena like synchronization (of various kinds), amplitude death, etc. Synchronization plays an important role in several biological systems. For example, the synchronous firing of pacemaker cells generates the normal sinus rhythm of human heart, and in a similar fashion the synchronous firing of billions of neurons in human brain constitute various brain waves. The nature of coupled dynamics often depends critically on the nature of coupling, time delay and other physical factors. A time delay in coupling can have a dramatic effect on the dynamics in certain systems, at times leading to periodic behaviour or sometimes to chaotic or hyper chaotic behaviour.

Two different schemes of synchronizing the STNOs are often considered in the literature. In an experiment using electrical nano-contacts at close proximity on the same mesa, Kaka et.al. (Kaka et al., 2005) showed that a direct spin-wave coupling can synchronize two STNOs. This scheme has proven to be very fruitful and is replicated in various experiments(Mancoff et al., 2005; Pufall et al., 2006). Recently attempts have been made to theoretically explain the spin wave induced coupling, predominantly using linear spin wave theory(Rezende et al., 2007; Chen and Victora, 2009). Another effective coupling scheme uses electrically connected STNOs to get them phase locked to the ac generated by themselves. Following the experimental demonstration of injection locking of STNOs to applied ac current by Rippard et. al.(Rippard et al., 2005), it was numerically shown that an array of oscillators electrically connected in series mutually synchronize in frequency as well as in phase(Grollier et al., 2006). The coupling was due to the microwave component of the common current flowing through the oscillators. This and similar coupling schemes have been explored extensively in the literature ever since(Persson et al., 2007; Georges et al., 2008; Tiberkevich et al., 2009; Zhou et al., 2009; Urazhdin et al., 2010; Dussaux et al., 2011; Li et al., 2012). This way of augmenting power by an array of electrically connected phase coherent oscillators, once realized, may prove to be a great milestone towards a nano scale oscillator with useful power output. Analytical as well as numerical studies of the synchronization effects in STNOs subject to microwave magnetic fields also appear in the literature(Bonin et al., 2010; Subash et al., 2013).

In this work we study the various types of synchronization as well as chaotic dynamics a drive-response coupling of two STNOs can bring about(Sanid and Murugesh, 2014). To this end, we propose a coupling using a high speed operational amplifier (Op Amp), which acts like a voltage follower. It essentially insulates the driver (master) oscillator from any feedback from the response (slave) system. The intention here is to study the dynamical response of a slave STNO to the signal input from another identical element whose dynamical behavior can be controlled. The current and applied field values fed in to the STNOs are such that they exhibit limit cycle behaviour. The oscillations can be large amplitude In-Plane (IP) oscillations (symmetric about the in-plane easy axis), or Out-of-Plane (OOP) where the precession is confined to only one of the hemispheres depending upon the initial condition. The signal generated across STNO1 by virtue of GMR effect is fed to STNO2 via the high speed Op Amp. The master-slave setup as well as the nature of coupling (which can be fine tuned using a coupling resistance, R_C, in the slave circuit) makes them a unique system not studied thus far. The time varying signal fed from the master effectively raises the dimensionality of the slave system (without coupling, the dynamics of the free layer magnetization of the slave STNO would be confined to surface of a 2-sphere, S^2, in the monodomain approximation which is employed in this work). We expect chaotic dynamics to appear in the borderline between IP and OOP oscillations for STNO2. What is remarkable is that, as the coupling resistance R_c is changed across this borderline we observe the emergence of phase locking and synchronous precession as well. We elaborate the various criteria which decides whether the system will go to synchronous, asynchronous or chaotic dynamics.

In addition, we also study the properties of this system under periodic forcing. We use a small ac input current, of frequency ω, in addition to the dc part to be fed to both of the STNOs. We then study how the phase portrait of slave system changes in relation to that of the master system. These considerations would be of great importance in building a robust coupled system of STNOs for enhancing micro-wave power.

4.2 Two spin-valve pillars coupled using high speed Op Amp

The system under consideration is a regular spin valve, consisting of a conducting layer sandwiched between two ferromagnetic layers - one pinned with magnetization along $\mathbf{e}_x$, the unit vector along the x direction, and the other free. Further, the free layer is also subject to a constant Oersted field also along the $\mathbf{e}_x$ direction (refer 3.1). The dynamics of the macrospin magnetization of the free layer is governed by the Landau-Lifshitz-Gilbert-Slonczewski (LLGS) equation (in dimension -full form)(Berkov and Miltat, 2008).

$$\begin{aligned}\frac{\partial \mathbf{m}}{\partial t} - \alpha \mathbf{m} \times \frac{\partial \mathbf{m}}{\partial t} = \\ -\gamma \mathbf{m} \times \left(\mathbf{H}_{eff} - \beta \mathbf{m} \times \mathbf{e}_x\right), \end{aligned} \tag{4.1}$$

where $\mathbf{m}(\equiv \{m_x, m_y, m_z\})$ is the normalized magnetization vector of the free layer. The effective field consisting of an external magnetic field (h_{ext}), anisotropy field (both in the $\mathbf{e}_x$ direction, with the thin film assumed to have a uni-axial anisotropy whose easy axis is aligned along the direction of the applied filed), and demagnetization field perpendicular to the layer, is given by:

$$\mathbf{H}_{eff} = h_{ext}\mathbf{e}_x + \kappa m_x \mathbf{e}_x - 4\pi M_s m_z \mathbf{e}_z. \tag{4.2}$$

The parameter β is proportional to the spin current density (for a given pillar geometry, and is roughly of the order of $200\,$Oe with typical current densities of the order of $10^8\ A/cm^2$). The rescaled applied dc current, a_{dc}, is same as β in what follows which has the dimensions of field intensity, frequently expressed in literature in the cgs unit Oersted. Also note that, in contrast to 3.1, here the polarization factor is grouped along with β (see Section 2.7 for more details). The expression for β is(Bazaliy et al., 2004):

$$\beta \equiv \frac{\hbar A j}{2 M_s V e} g(P), \tag{4.3}$$

where A is the area of cross section, j is the current density and V is the volume of the pinned layer. $g(P)$ is a dimensionless function of the degree of spin polarization of pinned layer $(0 \leq P \leq 1)$, with typical numerical value $\sim$0.3. The sample parameters appearing in (4.1) and (4.2) are given values similar to that of permalloy film. So, damping constant $\alpha = 0.02$, anisotropy constant $\kappa = 45$ Oe, demagnetization field constant $4\pi M_s = 8400$ Oe and the gyromagnetic ratio $\gamma = 1.7 \times 10^{-7}\, Oe^{-1}\, s^{-1}$.

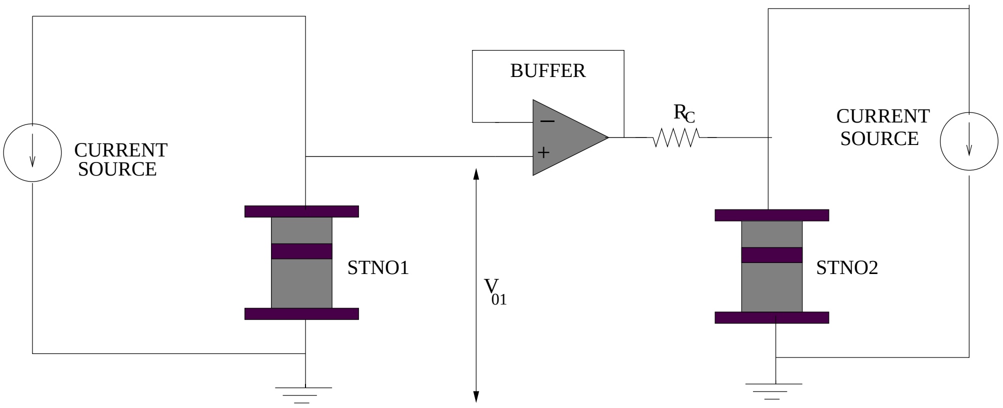

Figure 4.1: Circuit diagram depicting the coupling using a high-speed Op Amp. The left STNO is the master and the right one is the slave, each of them separately biased using a current source. The coupling resistance, R_C in the response circuit, turns out to be a very useful experimentally tunable parameter in this model.

We investigate the effect of coupling on the dynamical regions of the phase space of second STNO. Our coupling scheme using a high speed Op Amp is shown in figure 4.1. The Op Amp acts as voltage follower and effectively isolates the drive circuit from that of the response circuit. The voltage appearing across its non-inverting terminal is that of the STNO1 generated by virtue of GMR effect. By the property of Op Amp in buffer configuration essentially the same voltage appears across STNO2 and the coupling resistor R_C. Denoting the free-layer magnetization of STNO1 as $\mathbf{m}_1$ and that of STNO2 as $\mathbf{m}_2$ we derive the following pair of equations governing the dynamics of the above drive-response system:

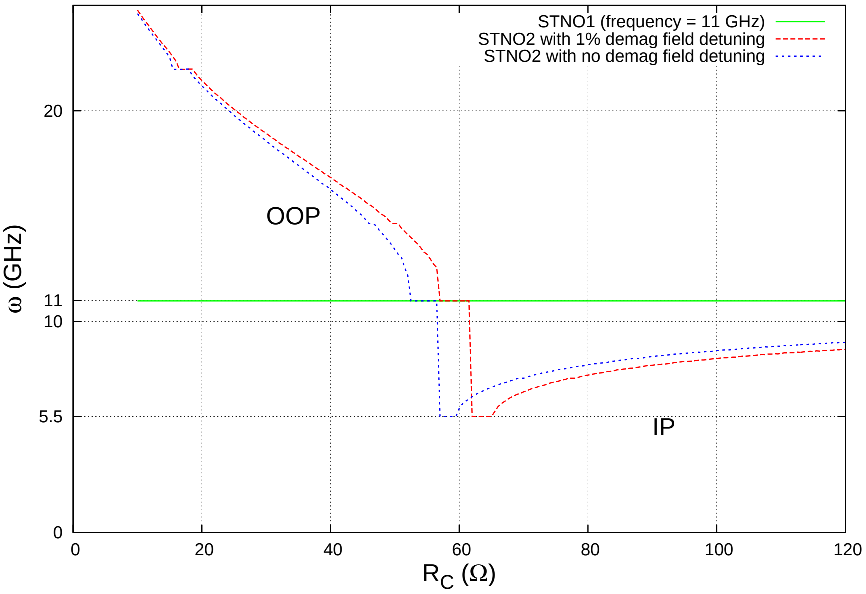

Figure 4.2: The synchronization curve of STNO2. The parameter values are $\kappa = 45$, $4\pi M_s = 8400\,\text{Oe}$, $R_P = 10\,\Omega$, $R_{AP} = 11\,\Omega$, $a_{dc} = 200\,\text{Oe}$ and $h_{ext} = 200\,\text{Oe}$. The mismatch in the anisotropy field is 5% and the mismatch in the demagnetization field is either 0 or 1% as indicated in the figure. Curve flattens up to plateaus at the synchronization regime. The IP and OOP regimes of oscillations are also marked in the figure.

$$\begin{aligned}\frac{\partial \mathbf{m}_1}{\partial t} - \alpha \mathbf{m}_1 \times \frac{\partial \mathbf{m}_1}{\partial t} &= \\ -\gamma \mathbf{m}_1 \times \left(\mathbf{H}_{eff_1} - \beta \mathbf{m}_1 \times \mathbf{e}_x\right), \end{aligned} \tag{4.4}$$

$$\begin{aligned}\frac{\partial \mathbf{m}_2}{\partial t} - \alpha \mathbf{m}_2 \times \frac{\partial \mathbf{m}_2}{\partial t} &= \\ -\gamma \mathbf{m}_2 \times \left(\mathbf{H}_{eff_2} - \beta' \left(t\right) \mathbf{m}_2 \times \mathbf{e}_x\right), \end{aligned} \tag{4.5}$$

where:

$$\beta' \left(t\right) = \beta \left(1 + \frac{R_1(t)}{R_C + R_2(t)}\right) \tag{4.6}$$

$$R_i = R_0 - \triangle R \; cos \left(\theta_i\right). \tag{4.7}$$

The resistances of the two STNOs, R_1 and R_2, depend on the dynamical state of the free layer and is modelled using the standard equation (4.7), where θ is the angle between the free layer and the pinned layer magnetizations(Grollier et al., 2006). If R_P and R_{AP} are the resistances of the spin valve in parallel and anti-parallel configurations, respectively, then $R_0 = (R_P + R_{AP})/2$ and $\triangle R = (R_{AP} - R_P)/2$. The right hand side of equation (4.6) comprises of contribution from coupling as well as the bias voltage of the slave STNO. For simulating the STNO dynamics we used a fourth order runge-kutta method with a time step of 0.5 ps. We used the Wolf algorithm(Wolf et al., 1985) to find the Lyapunov exponents which is used in conjunction with power spectrum to differentiate chaotic, multi-periodic as well as periodic dynamics. Fourier analysis is used to determine the precession frequencies in the periodic regime.

4.3 Coupled dynamics - Synchronization and Chaos

4.3.1 Synchronization

The STNOs are given different initial conditions and are given 10% mismatch in anisotropy field and about 1% mismatch in demagnetization field. The coupled LLGS equation, (4.4) and (4.5), is simulated using a fourth order runge-kutta algorithm with a time step of 0.5 ps. The inclusion of time delay (due to Op Amp action) turned out to be of no significance to the results we are presenting here and hence omitted from the discussions that follow until Section 4.

When the GMR values are chosen to be $R_P = 10\,\Omega$ and $R_{AP} = 11\,\Omega$, we see the occurrence of 1:1 as well as 2:1 synchronization as plateaus in figure 4.2. In the 1:1 synchronization regime, the master and slave STNOs precess with the same frequency, whereas in 2:1 synchronization the master STNO has double the frequency of precession as compared to slave STNO. As the coupling resistance R_C is increased the limit cycle frequency of the slave decreases in the OOP regime and then cross over to IP regime. After this, increasing R_C causes the frequency to slowly go up. This also matches with the general response of a STNO to spin current, as increasing R_C effectively reduces the strength of coupling(Bertotti et al., 2005). Upon close inspection

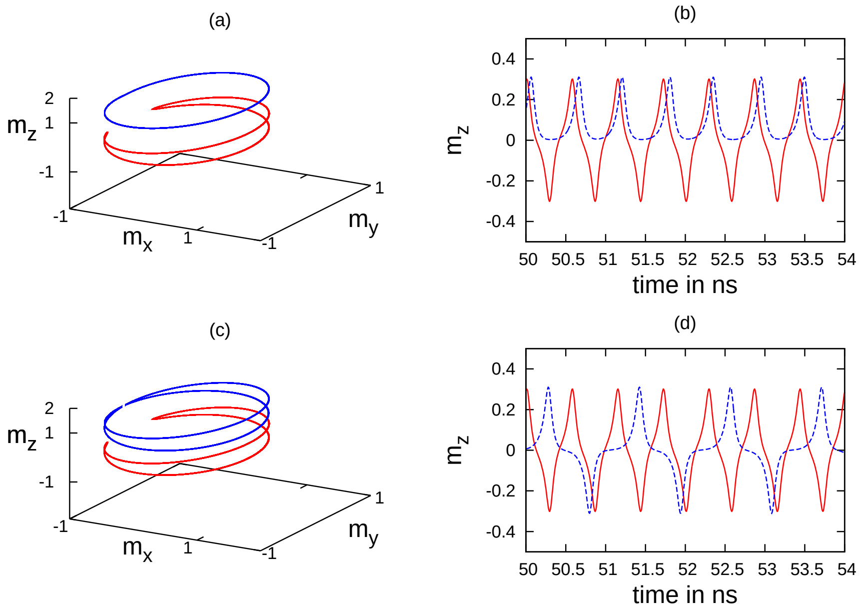

Figure 4.3: The phase space trajectory (limit cycles) and time trace of free layer magnetization dynamics at 1:1 as well as 2:1 synchronization phases. Solid red lines (lower trajectory in (a) and (c)) denote the master where as dashed blue lines (upper trajectory in (a) and (c)) denote the slave dynamics. To avoid overlap of the figures, in (a) and (c), the trajectory of the slave oscillator (dashed blue lines) has been shifted up by 1 unit along the m_z axis.

evidence for 1:2 synchronizations can also be found in the figure. This is discussed in some detail later in this section. The nature of free layer magnetization dynamics in these regions are further elucidated in figure 4.3. Figure 4.3 (a) and (b) are phase space trajectory and time trace of m_z respectively, at 1:1 synchronization region. The coupling resistance $R_C = 60\,\Omega$ and the other parameter values are as in figure 4.2. It is clear that when the master is executing IP oscillations the slave is executing OOP oscillations. Figure 4.3 (c) and (d) are phase space trajectory and time trace of m_z respectively, at 2:1 synchronization region. The coupling resistance $R_C = 63\,\Omega$. It can be seen that both the master and the slave are now executing IP oscillations. We see that there is a definite phase-locking happening between the STNOs though phase of one lags the other (figure 4.3 (b) and (d)). While 1:1 mode locking, when STNO1 is undergoing IP oscillations STNO2 goes to OOP oscillation. During 2:1 mode locking both STNO1 as well as STNO2 executes IP oscillations.

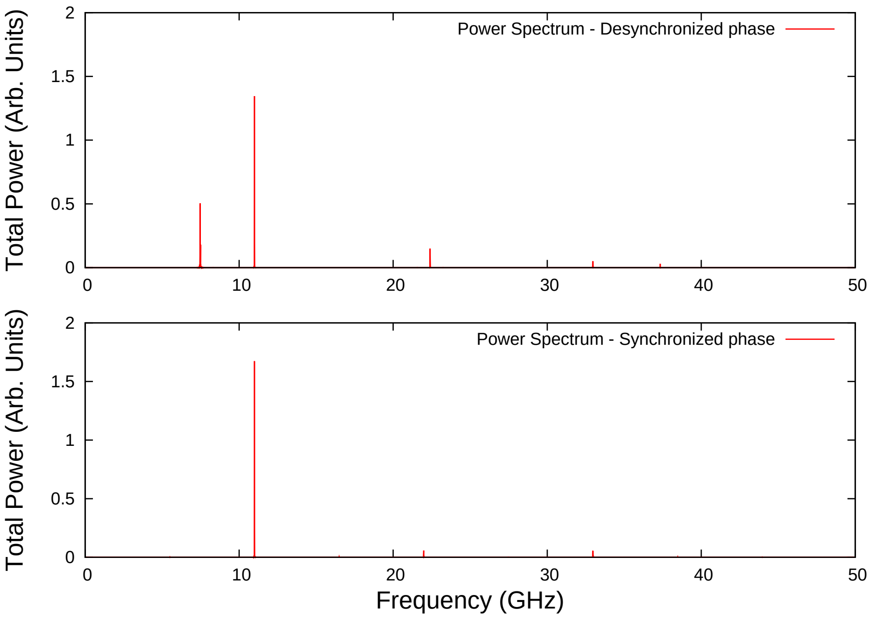

Figure 4.4: The power spectrum for the synchronized as well as desynchronized phase. Parameter values are same as that in figure 4.2. Synchronized precession is at $11\,\mathrm{GHz}$. Desynchronized precession is at $11\,\mathrm{GHz}$ for the Master and $7.5\,\mathrm{GHz}$ for the slave. At synchronization $R_C = 60\,\Omega$ and at desynchronization $R_C = 80\,\Omega$.

In order to see the power gain at the synchronization frequency we plot the Fourier spectrum of both the STNOs in a single figure (figure 4.4 (b)). For comparison the scenario during desynchronization is also given at the top of the same figure. We see a distinct increase in the power at the synchronization frequency at $11\,\mathrm{GHz}$. The power ratio of the two oscillators, an important quantity to keep track of, is found to be independent of initial condition of the slave system, a direct consequence of limit cycle motion. To further analyse the extent of synchronization we construct the phase portrait in the plane of a_{dc} and R_c which is shown in figure 4.5. Many points in the region (blank) between the 1:1 and 2:1 mode locking corresponds to the multi-periodic dynamics where the dynamics jumps between the two symmetric OOP orbits but with a definite frequency. In multi-periodic case, the frequency of STNO2 differs from that of STNO1 and hence is grouped with the desynchronization region. This point is further elaborated in Section 4.3.2. It is evident from figure 4.5 that higher spin currents require higher coupling resistance in order to synchronize the coupled dynamics. The power ratio (between oscillator 2 and 1) remains more or less the same within the 1:1 synchronization regime, with average value 0.5 and fluctuations bounded between 0.6 and 0.4, even when the limit cycle frequency is changed by tuning the parameters. We notice that, apart from some isolated points, chaos at the boundary between IP and OOP oscillations is seldom observed at the chosen parameter values. In the next section we give a plausible explanation for the clustered chaotic points far from the synchronization region.

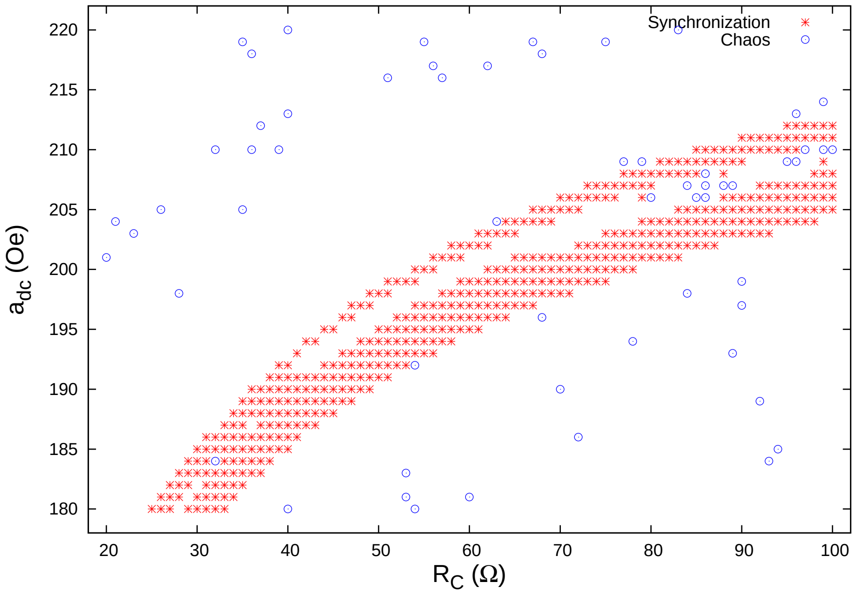

Figure 4.5: The phase portrait in the $a_{dc} - R_C$ plane at the GMR value $R_{AP} = 11\,\Omega$. h_{ext} is fixed at 200 Oe. We see a well delimited synchronization region (red asterisks) surrounded by desynchronization regions (blank). Chaos is observed only at isolated points (blue circles).

4.3.2 Chaos

When the GMR values are chosen to be $R_P = 10\,\Omega$ and $R_{AP} = 12\,\Omega$, as shown in figure 4.6, we see the occurrence of chaos at the boundary between 1:1 and 2:1 synchronization regions. This is because the system switches between these modes of oscillations in a random manner. In figure 4.6 we have shown the time trace as well as the power spectrum during this phase. This is interesting because it can be used to estimate the GMR ratio itself in conjunction with other experimental techniques. During chaos, the power spectrum gets noisy and there is no useful power to be derived

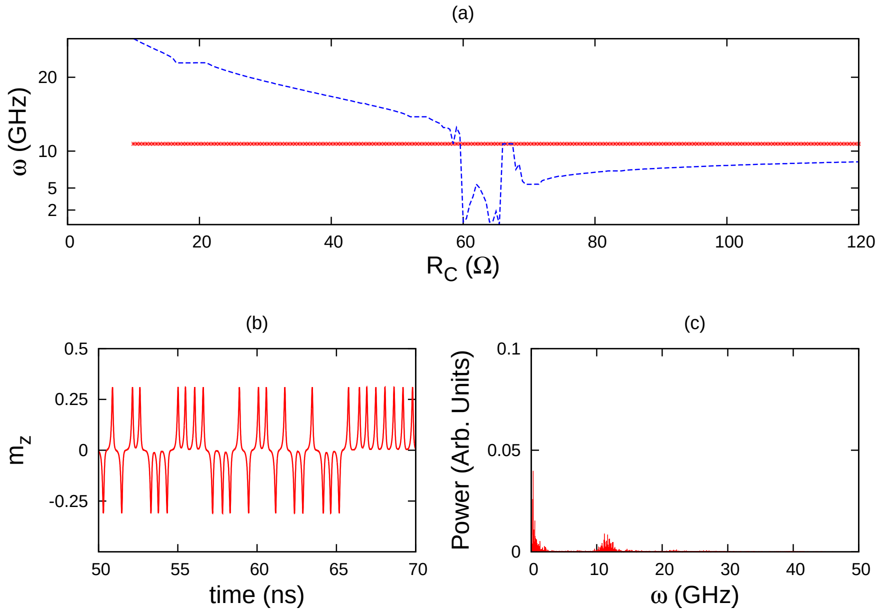

Figure 4.6: The occurrence of chaos in coupled STNOs at the GMR value $R_{AP} = 12\,\Omega$. (a) At $R_C = 60\,\Omega$, which showed synchronization earlier, we see the limit cycle frequency approaching zero. This is due to irregular switching of STNO2 dynamics among the available OOP and IP modes which, at these parameter values, is same as 1:1 and 2:1 synchronization modes respectively. The red line is the frequency of STNO1. (b) The time trace of m_z displaying the random jump between IP and OOP modes. (c) The power spectrum of STNO2 showing the vanishing of the well-defined peaks. The scale of power is the same as that in figure 4.4.

out of the system. Notwithstanding the commercial problems chaotic dynamics can bring about, from a dynamical systems point of view, they are still extremely important and interesting. The effect brought about by increasing R_{AP} can be understood in the following way: Increasing R_{AP} essentially implies a direct increase in the GMR value which has a direct impact on the electrical coupling and can sometimes enhance the synchronization regimes(Grollier et al., 2006). In our case the chaotic region seems to be sensitive to the GMR value, and more the GMR value stronger the chaotic dynamics.

For gaining a better understanding of chaotic dynamics we turn our attention to the control space dynamics in $R_C - a_{dc}$ plane (figure 4.7). We see the onset of chaotic

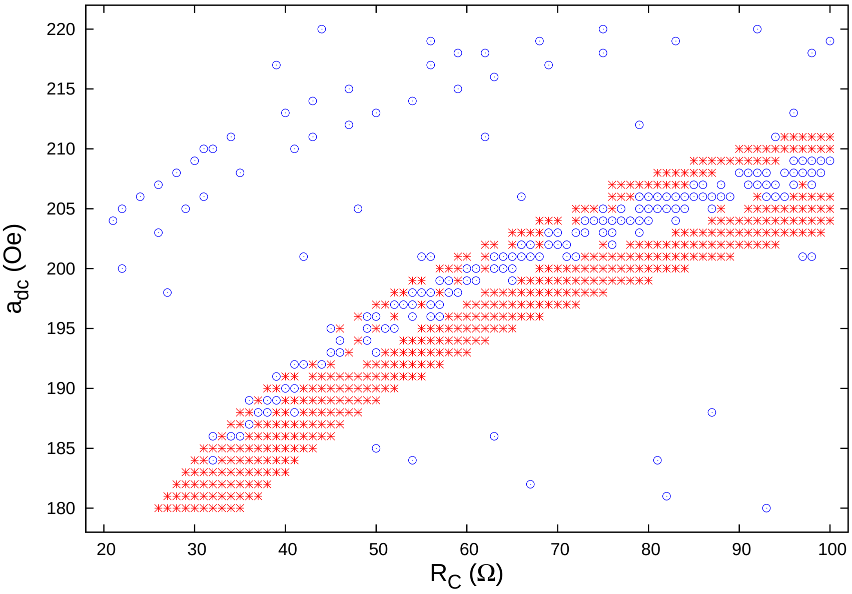

Figure 4.7: The phase portrait in the $a_{dc} - R_C$ plane at the GMR value $R_{AP} = 12\,\Omega$. All other parameter values are same as in figure 4.5. We see chaotic dynamics (blue circles) encapsulated by the synchronization regions (red asterisks). Blank regions corresponds to desynchronization dynamics.

dynamics within the synchronization region itself as expected. As in the previous case, here also the dynamics turns into multi-periodic regime for some parameter values but is included in the desynchronization region in phase portraits. In figure (4.7, at $a_{dc} = 200Oe$ and $R_c = 66\Omega$, we have a desynchronization region which, for representative purpose, has been used to generate figure (4.8). It is clear that the dynamics is multi periodic. Since the frequency of this precession is different from that of the master STNO, it is grouped under desynchronization region (For example here slave STNO precess with frequency = 2.742 GHz where as master STNO frequency = 11 GHz). However, all the desynchronization points in between the synchronization branches do not belong to this category. Thus we see that in these coupled systems where various m:n synchronizations happen in close by parameter ranges, chaotic dynamics tends to happen at the boundary between these regions. This is also crucial in noisy systems, because noise invariably make the system to randomly switch between the available states and can result in the vanishing of resonance peak even at synchronization(Li et al., 2012).

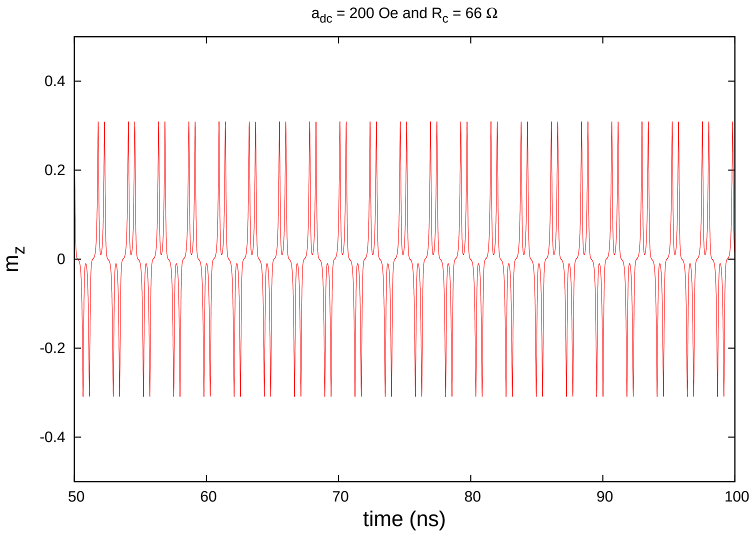

Figure 4.8: Time trace of m_z dynamics at $a_{dc} = 200Oe$ and $R_c = 66\Omega$ which is a desynchronization region in figure (4.7). It is clear that the dynamics is multi periodic. Other parameter values remain the same as in figure (4.7).

The phase picture in the $h_{ext} - R_C$ space also shows the embedding of chaos region within the synchronization region(figure 4.9). Notice that chaos regions also appear outside of synchronization regions in figure 4.7 as well as in figure 4.9. This is because in the simulations we have only looked for 1:1 and 2:1 mode locking where as other m:n synchronizations are also possible in the system. We see evidence of such a locking in figure 4.2, where a small plateau appears at the frequency appropriate for 1:2 mode locking. Arguably chaotic dynamics is expected to be found associated with such higher order mode locking as well. Here it is worth pointing out that fractional synchronization in coupled STNOs are also experimentally observed(Urazhdin et al., 2010).

4.3.3 Robustness under noise

Real world experiments are seldom free from external noise. This can affect the reliability of our synchronization as well as chaotic regimes. In order to address the issue of robustness, we studied numerically the effect of incorporating a Gaussian white noise to the spin current, which is a good numerical approximation to thermal noise. The result of such a numerical experiment incorporating noise is shown in figure 4.10. We notice

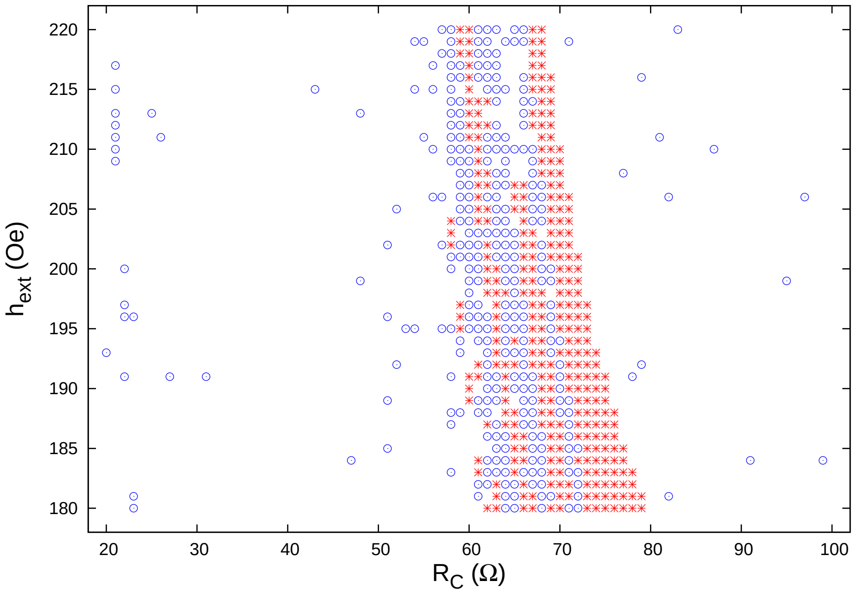

Figure 4.9: The phase portrait in the $h_{ext} - R_C$ plane. a_{dc} is fixed at 200 Oe. Other parameter values and colour codings are as in figure 4.7. Here again chaos is closely tied to synchronization dynamics.

that when a Gaussian white noise with standard deviation 0.3 was used, introducing an equivalent error of ± 1 Oe in the spin current (quite large deviation in a real experiment), our synchronization and chaotic regions remain more or less intact.

We even pushed the system with an error of ± 5 Oe in spin current and still found the synchronization regions intact, though more and more desynchronization regions turned to chaotic regions. We believe this suffices to state that the system under consideration is indeed robust to thermal fluctuations.

4.4 Coupled dynamics with periodic forcing

In order to incorporate the full richness of spin-valve dynamics into our study, we let both of our STNOs to be susceptible to dynamical chaos. We use a small ac input current, of frequency ω, in addition to the dc part to generate dynamical chaos. A time varying current is imperative to witness chaos in an isolated STNO, whose phase space is otherwise just two dimensional (under the macrospin assumption). Such a system displays three distinct dynamical regimes, namely *Synchronization, Modifications and*

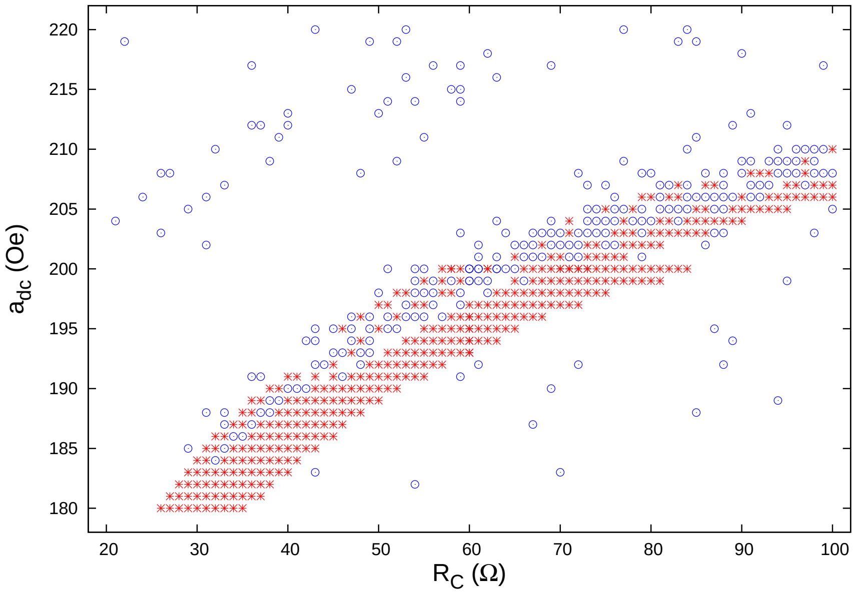

Figure 4.10: The phase portrait in the $a_{dc} - R_C$ plane when a Gaussian white noise with standard deviation 0.3 was used, introducing an equivalent error of ± 1 Oe in the spin current. All parameter values and the interpretation of legends remain the same as that of figure 4.7. We see that synchronization as well as chaos regions remain more or less intact.

Chaos in the $a_{dc} - \omega$ parameter space (Li et al., 2006). Qualitatively, similar dynamical behavior is noticed even with a periodically alternating Oersted field instead of the alternating spin current (Murugesh and Lakshmanan, 2009). The figure 4.2 in Section 2 is applicable here with the modification that apart from the dc biasing voltage both the STNOs are driven by ac current sources with tunable frequency as well. We have a small ac current, in addition to dc current, flowing through both of the STNOs.

It should be noted that this scenario is qualitatively different from the previous case in various important aspects. The major differences are listed below:

- Here the master and slave oscillators are driven using a periodic signal, whereas in the unforced scenario only the slave STNO experiences a time varying signal (fed from the output of STNO1) in the form of coupling signal.

- Here the master STNO can go chaotic feeding the slave with a chaotic signal as shown later in this section, whereas in unforced case the slave is at best fed a periodic signal.

- The meaning of synchronization itself differs considerably from the earlier case. In the unforced case, the frequency of slave STNO synchronize with that of the master STNO. In the forced case it is the synchronization of slave STNO with that of the external forcing which is considered as synchronization.
- Yet another difference is that, in the unforced case the frequency of master can only be controlled indirectly via the injected spin current, where as in the forced case frequency of forcing (ω) itself is an experimentally tunable parameter.

Again the Op Amp in voltage follower mode replicates the voltage being applied to its non-inverting terminal on its output terminal which act as the coupling signal. In the present analysis we take in to account the time delay, τ, introduced by the Op Amp action between the the two oscillators. Since this is due to the internal switching delay of Op Amp, it is taken to be a constant in the simulations ($\tau = 0.05\,\mathrm{ns}$). For the sake of numerical calculations, delay coupled oscillator pair is approximated as an array of N coupled oscillators, each having a coupling delay of $\Delta = \tau/N$ with its previous member(Farmer, 1982; Lakshmanan and Senthilkumar, 2010). It is noticed that time delay has no effect on the dynamics of the system and is included here for the sake of completeness of the analysis. Our effort to introduce phase synchronization via tuning time delay has also been futile as yet.

The modified coupled LLGS equations are given below (see Section 2 for details):

$$\begin{aligned}&\frac{\partial \mathbf{m}_1}{\partial t} - \alpha \mathbf{m}_1 \times \frac{\partial \mathbf{m}_1}{\partial t} = \\ &\quad -\gamma \mathbf{m}_1 \times \left(\mathbf{H}_{eff_1} - a\left(t\right)\mathbf{m}_1 \times \mathbf{e}_x\right), \end{aligned} \tag{4.8}$$

$$\begin{aligned}&\frac{\partial \mathbf{m}_2}{\partial t} - \alpha \mathbf{m}_2 \times \frac{\partial \mathbf{m}_2}{\partial t} = \\ &\quad -\gamma \mathbf{m}_2 \times \left(\mathbf{H}_{eff_2} - \beta\left(t-\tau\right)\mathbf{m}_2 \times \mathbf{e}_x\right). \end{aligned} \tag{4.9}$$

where:

$$a\,(t) = (a_{dc} + a_{ac}\, cos\; \omega t) \tag{4.10}$$

$$\beta\,(t-\tau) = a\,(t) + \frac{a\,(t-\tau) \times R_1(t-\tau)}{R_C + R_2(t)} \tag{4.11}$$

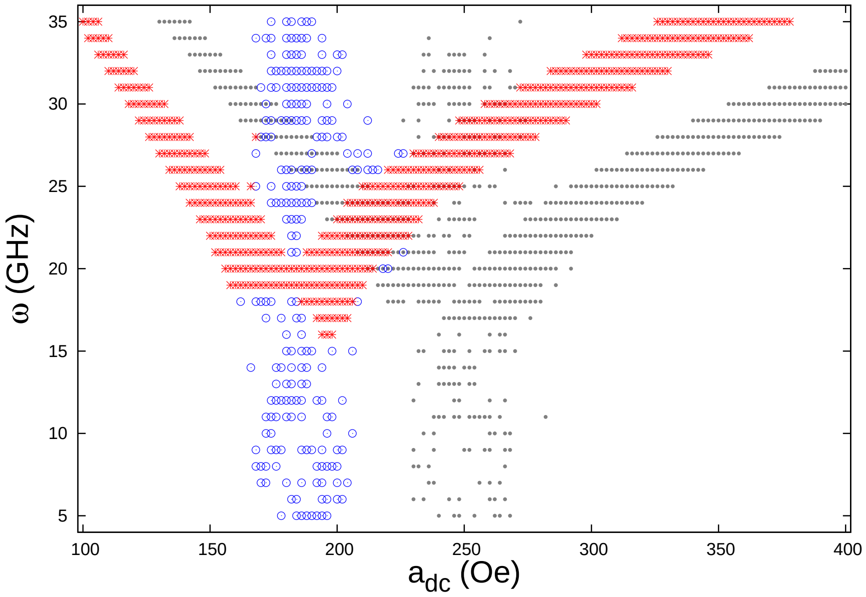

Figure 4.11: Phase diagram of the free layer magnetization dynamics in the $a_{dc} - \omega$ plane for the slave STNO. The delay time $\tau = 0.05\,$ns. The parameter values are $a_{ac} = 20\,$Oe, $\kappa = 0$, $4\pi M_s = 8400\,$Oe, $R_P = 10\,\Omega$, $R_{AP} = 11\,\Omega$, $R_C = 20\,\Omega$. The three dynamical regions are synchronization(red asterisks), modification(blank) and chaos(blue circles). The phase diagram for the master, STNO1, shown shaded for reference, also has similar dynamic regimes.

The $\omega - a_{dc}$ phase diagram for the drive system, STNO1 (figure 4.11), features the *synchronization branches* with a *chaotic stem*, as expected (see figure 1 in (Li et al., 2006)). Interestingly, the response system, STNO2, too shows synchronization branches and a chaotic stem (red crosses and blue stars, respectively, in figure 4.11) identical to that of the drive system, but with a prominent shift of the entire phase diagram towards a lower value of spin current, a_{dc}, with the shift determined only by the coupling resistor R_C. An important observation is that the qualitative picture of the phase diagram is preserved by the response STNO, in spite of being fed in, at times, a chaotic signal.

One may speculate that for an extended system of N-STNOs, coupled in the manner discussed here, the individual STNOs will continue to preserve their qualitative phase (tree) structures, albeit shifted. Although the phase diagram of STNO1, the chaotic stem and synchronization branches, appears shifted compared to that of STNO2, it has to be noted that upon a careful reading the two 'trees' are not exactly identical in their detail. For instance, there are points on the stem region of STNO1 that correspond to chaotic motion, but whose counterparts in the stem region of STNO2 do not.

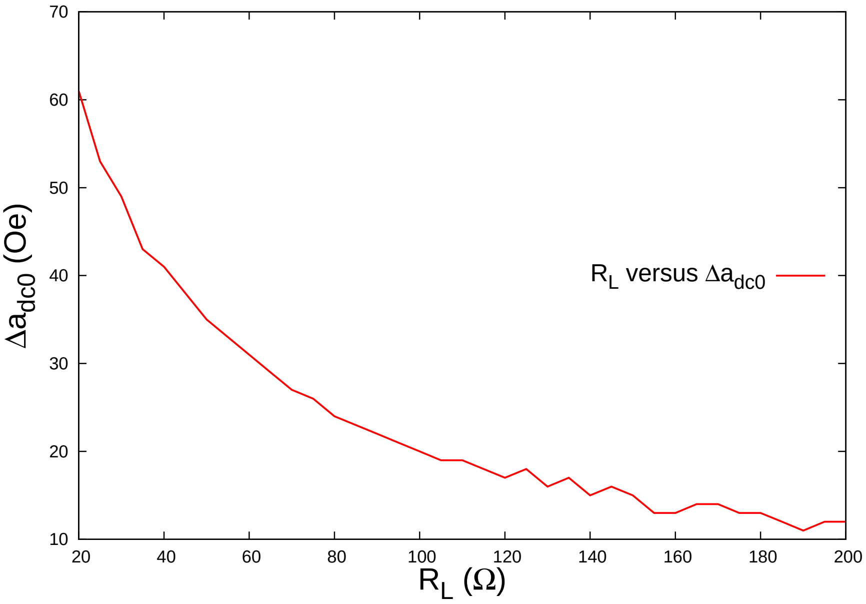

Figure 4.12: The dependence of shift in critical value of current denoted as Δa_{dc0} for the onset of chaos on the coupling resistance R_C for $\omega = 10\,\text{GHz}$. R_C is measured in Ωs and Δa_{dc0} in Oe. As can be seen from the figure, larger the resistance lower the shift.

An important parameter in the set of coupled equations (4.8) and (4.9), is the coupling resistance in the slave circuit, R_C. For a coupling resistance of $20\,\Omega$, the shift in a_{dc} is noticed to be nearly $60\,$Oe. The shift in the value of a_{dc} as a function of R_C is shown in figure (4.12). Agreeably, the shift in the value of a_{dc} approaches zero for large values of R_C, when $\beta(t)$ approaches $a(t)$ and the signal from STNO1 is effectively nullified.

We rewrite here the expression for the coefficient β, equation (4.11), to gain a heuristic understanding of the contribution due to coupling.

$$\beta = a_{dc}\left(1+\frac{R_1(t-\tau)}{R_C+R_2(t)}\right)+$$
$$a_{ac}\left(cos\omega t + cos\omega(t-\tau)\frac{R_1(t-\tau)}{R_C+R_2(t)}\right)$$
$$= a'_{dc} + a_{ac}\, f(t) \tag{4.12}$$

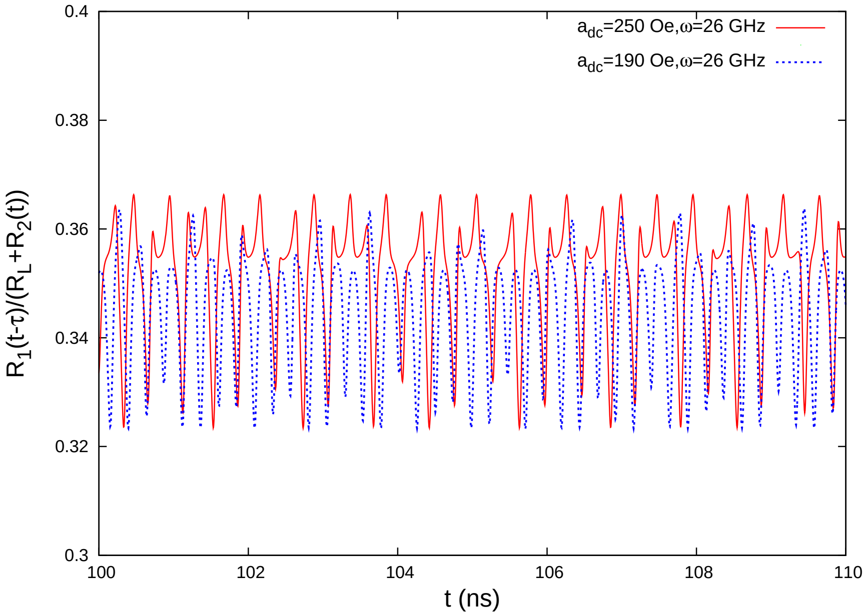

Figure 4.13: Time series of the ratio $\left(\frac{R_1(t-\tau)}{R_C+R_2(t)}\right)$. The average fluctuations are smaller than one but yet significant. The value of $R_C = 20\,\Omega$. The red line corresponds to $a_{dc} = 250\,$Oe and $\omega = 26\,$GHz and blue lines correspond to $a_{dc} = 190\,$Oe and $\omega = 26\,$GHz. Other parameters remains the same as that of figure 4.11.

For some sample values of the parameters ω and a_{dc} we study the temporal behaviour of the term $R_1(t-\tau)/(R_C+R_2(t))$ (see figure (4.13). It is noticed that this ratio shows sharp fluctuations over a period, but varies smoothly in between. For the sample values we studied, the time period of fluctuations are comparable (∼0.4 ns) to the time period of the ac part of the spin current(∼0.25 ns). However, the magnitude of these fluctuations are bounded in the range of 0.04, but with a significant average value compared to 1. Thus, allowing for small fluctuations, the effective value of the dc current increases (a'_{dc} in (4.12)), consequently reducing the critical value of a_{dc} at which chaotic dynamics sets in. For the same reason, the time periodic part of β, $f(t)$ in (4.12), remains periodic with the same frequency ω as the applied spin-current.

4.5 Outlook

In summary, we have proposed a system of two coupled spin-torque nano-oscillators—a drive system and a response system—and studied its behaviour numerically. The occurrence of 1:1 as well as 2:1 synchronization in the system are examined in detail. In the crossover region between these two synchronization dynamics we have shown the existence of chaotic dynamics and how it depends upon system parameters. We have demonstrated the power augmentation in the synchronization regimes which is of great practical importance in the current spintronics industry. We extended the study to the coupled dynamics under periodic forcing scenario and demonstrated the interesting possibility of controlling the nature of dynamics of the response oscillator - periodic oscillations synchronized to the applied ac spin-current, or chaotic. Our simulations show a prominent shift of the chaos regions towards low spin-current side due to coupling, the shift being determined by the coupling resistor. The pivotal role played by the coupling resistor in unforced as well as forced scenarios, as an experimentally tunable parameter for the response system, is demonstrated.

Commercially available ultra-high speed Op Amps (frequency $>$1 GHz) have frequency ranges upto 2 GHz (For example the model LMH6702 from Texas Instruments is a 1.7 GHz, ultra low distortion, wide band Op Amp). Though frequency of limit cycles in STNOs usually shoots above this range, making the immediate experimental realization of the coupled system impractical, we nevertheless believe higher frequency Op Amps would be available commercially in the near future. Moreover, from our results it is apparent that it is the average value of fluctuations which is responsible for dynamical effects. Hence, minor distortions in the high frequency coupling signal due to Op Amp will not alter the the results presented here.

The master slave coupling and the preservation of structures in the phase space are attractive features for large scale integration of coupled STNOs. Thermal as well as

other fluctuations in the output signal of the slave will not be fed back into the master. So a fine tuned master can serve as the source of a pre-set frequency to which all other oscillators can be made to synchronize in a *N-coupled* scenario by tuning individual coupling resistors. This feature, unique to master-slave coupling, makes our proposal distinct and interesting over other proposed coupling schemes.

CHAPTER 5

CONCLUSION

“As far as the laws of mathematics refer to reality,
they are not certain; and as far as they are certain,
they do not refer to reality."
— Albert Einstein

In the preceding chapters, we have described our results in detail, and also summarized them at various places in the text. It remains to place the work in a broader perspective, and to list interesting open problems and vistas for future work. Along the lines of the famous saying “*No man is an island unto himself*" (attributed to poet John Donne), one can say that no scientific work is an island unto itself. The work presented here forms part of a grander constellation of problems related to the area of spintronics and nonlinear dynamics in general. Here we outline some of the directions research in this area can take.

First, on the numerical front, the most obvious extension of the work presented here is to go beyond the *macrospin* concept. This means tackling a nonlinear *partial* differential equation in two or three dimensions, which is a computationally extensive problem. This nevertheless is an important eventuality to be taken care of in the future work. Dispensing with the macrospin approximation leads us to a full fledged micromagnetic simulation with the exchange interaction term included (refer 2.4). This could be achieved either by using a finite difference method or a finite element method depending upon the geometry of the sample using packages like OOMMF(Donahue and Porter, Sept 1999) or nmag(Donahue and Porter, Sept 1999; Fischbacher et al., 2007). Many results have already been reported in this regard in the literature(Li and Zhang, 2003; Liu et al., 2003; Lee and Dieny, 2006; Acremann et al., 2006). Some predictions of single-domain spin-torque theory, such as very weak dependence of the critical current density j_c for the onset of magnetic excitation on wafer-level distribution of cell size, have been shown to be incorrect by such rigorous micromagnetic simulations. It is seen that the switching time and current density are strongly affected by the cell size for low spin polarization. Larger samples with a small length-to-width ratio and small spin polarization can exhibit a nonmonotonous dependence of switching time on current. Excitation of incoherent spin waves caused by the circular Oersted field due to the current is responsible for this nonmonotonous dependence. However, the magnetic dynamics recovers a single-domain-like behaviour when the spin polarization is high and/or the cell size is small(Lee and Dieny, 2006). In another study, micromagnetic simulations revealed that, spin transfer effects and the vortex fields cannot fully account for the CIMS in low resistance MTJs (area of cross-section $\sim$2-3 μm^2) with reported critical current densities of 1.9×10^6 A/cm^2(Liu et al., 2003). It would be illuminating to see how our results get modified by relaxing the monodomain approximation. But apart from that, this is a research area on its own right and can lead to new and unexpected results.

Another interesting area of research, closely related to the work presented here, is the current driven domain wall motion in nano ferromagnetic films. Magnetic domain walls (DW) have always attracted enough attention due to its fundamental and applicative appeal. They are small magnetic objects propagating with high speeds ($\sim$100 ms^{-1})(Hayashi et al., 2007; Pizzini et al., 2009). The first conclusive experimental evidence for current driven DW motion came in the years 2000(Grollier et al., 2002; Kläui et al., 2003; Grollier et al., 2003). By using e-beam lithography techniques, it was then possible to fabricate magnetic stripes, which favoured magnetization reversal by domain wall nucleation and propagation. Thanks to the small cross section of the samples, the current densities necessary to move the domain wall where reached for reasonable injected dc currents of typically a few mA. The favoured geometry of the DW in magnetic stripes made of NiFe material is that of Neel type. The magnetization rotates in the plane of the layer, resulting in domain wall sizes of a few hundred nanometer, comparable to the stripe width. The spin-transfer torque experienced by such a wall can be written as (this is due to in-plane currents as contrasted to the out-of-plane currents we have been dealing with till now using equation (2.17)):

$$\mathbf{T}_{STT} = -(\mathbf{u}\cdot\nabla)\mathbf{m}, \tag{5.1}$$

where **u** is a velocity proportional to the amplitude of the torque, given by:

$$\mathbf{u} = JPg\mu_B/(2eM_s), \tag{5.2}$$

where J is the current density, P the spin polarization, M_s the saturation magnetization, g the g-factor and μ_B the Bohr magneton. As we did in the earlier chapters, it is quite useful to add this term to the LLG equation (2.13), to study the current induced DW motion. We get:

$$\dot{\mathbf{m}} = -\gamma\mathbf{m} \times \mathbf{H}_{eff} + \alpha\mathbf{m} \times \dot{\mathbf{m}} - (\mathbf{u} \times \nabla)\mathbf{m}. \tag{5.3}$$

The other terms have the usual meaning as explained in chapter 2. By solving equation (5.3) analytically or by micromagnetic simulations, the predicted threshold current densities for domain wall motion were one order of magnitude larger than the experimental values(Thiaville et al., 2004). In order to account for the experimental values, one more term was added to equation (5.3)(Zhang and Li, 2004):

$$\dot{\mathbf{m}} = -\gamma\mathbf{m} \times \mathbf{H}_{eff} + \alpha\mathbf{m} \times \dot{\mathbf{m}} - (\mathbf{u} \times \nabla)\mathbf{m} + \beta\mathbf{m} \times [(\mathbf{u} \times \nabla)\mathbf{m}], \tag{5.4}$$

where the last term points out of the plane and generates demagnetizing field for efficient DW motion. β is a dimensionless parameter like the Gilbert damping α, but is not the same as the one introduced in equation (2.18). Looking at equation (5.4), it is obvious that much analytic and numerical work can be done here along the same lines done in this thesis. This is an active research area mainly becuase of the potential application in the DW-RAM and the ‘racetrack’ memory(Parkin et al., 2008).

Even more exotic structures such as magnetic vortices appear in suitably shaped nano magnetic elements because they are energetically favoured over other configurations. Vortex is a curling in-plane magnetic configuration with a small spot of out-of-plane magnetization appearing at the core of the structure(Shinjo et al., 2000; Wachowiak et al., 2002). In 2007, spin polarized current driven magnetic vortex oscillations are demonstrated in a nanoscale spin valve structure(Pribiag et al., 2007; Mistral et al., 2008). Since then, magnetic vortex oscillators have begun to attract considerable attentions owing to several advantages over STT-driven nano-oscillators associated with the precessional motion of uniform magnetization (chapter 4). STT induced by in-plane currents are shown to produce a vortex gyroscopic motion, known as the vortex core (VC) translational mode, while passing through a single vortex(Shibata et al., 2006). Spin polarized current (perpendicular to plane) induced vortex polarity switching is also demonstrated around the same time(Caputo et al., 2007). Although most of the analysis are done using OOMMF(Donahue and Porter, Sept 1999), very useful analytical approaches are since been developed. One such approach includes treating the vortex as a quasi particle whose motion (with center at $\mathbf{a} = [a_x, a_y]$) is described by an equation derived from the LLG equation by Thiele(Thiele, 1973) (later adopted to vortices by Huber(Huber, 1982))):

$$\mathbf{G} \times \dot{\mathbf{a}} = \frac{1}{R^2}\frac{\partial E_{tot}}{\partial \mathbf{a}} - \overset{\leftrightarrow}{\mathbf{D}} \cdot \dot{\mathbf{a}}, \tag{5.5}$$

where $\mathbf{G} = \frac{1}{\gamma}(-2\pi p L \mu_0 M_s \hat{\mathbf{z}})$ is the gyrovector with $p = \pm 1$ denoting the vortex's polarity. L denotes disk's thickness, $\overset{\leftrightarrow}{\mathbf{D}} = \frac{1}{\gamma}(-2\pi L \alpha \mu_0 M_s(\hat{\mathbf{x}}\hat{\mathbf{x}} + \hat{\mathbf{y}}\hat{\mathbf{y}}))$ is the dissipation tensor of second order, and $E_{tot}(\mathbf{a})$ is the total magnetostatic potential energy of the vortex. Thiele's equation has been used as one of the most convenient approaches for dealing with vortex dynamics. Equation (5.5) can be extended to include the STT effects but we refrain from describing it here (see reference (Shibata et al., 2007)).

We now shift the focus to future work in the analytical front. The Landau-Lifshitz equation without dissipation or spin-transfer term appears as a dynamical equation for the classical continuous Heisenberg model of ferromagnets. The Hamiltonian density for the Heisenberg ferromagnet is given by:

$$\mathcal{H} = \frac{1}{2}(\partial_i \mathbf{m}) \cdot (\partial^i \mathbf{m}), \tag{5.6}$$

where the spin, $\mathbf{m}(\mathbf{r}, t) = (m_1, m_2, m_3)$, is a three dimensional vector with unit modulus ($\mathbf{m}^2 = 1$). Index i runs from 1 to 3 and dot product is defined in the internal spin space. This model is also closely related to the $O(3)$ nonlinear sigma model, which is the Lorentz invariant extension of the Heisenberg model. This is also the simplest relativistic field theory admitting soliton solutions. The model has the following Lagrangian density(Rajaraman, 1987):

$$\mathcal{L} = \frac{1}{2}\,(\partial_\mu \mathbf{n}) \cdot (\partial^\mu \mathbf{n}), \tag{5.7}$$

where **n** is a 3D vector in the internal space with the constraint $\mathbf{n} \cdot \mathbf{n} = 1$. μ is the Lorentz index running from 0 to 3. Scalar product is implied in internal space as well as in coordinate space. Note that both the Lagrangian (5.7) and the constraint are invariant under global $O(3)$ rotations in the internal space, hence the name $O(3)$ nonlinear σ-model. The LL equation in (1+1) dimensional was shown to be completely integrable some decades ago(Lakshmanan, 1977; Takhtajan, 1977). Belavin and Polyakov showed that in 2D, a class of static solutions can be obtained, each associated with some topological charge(Belavin and Polyakov, 1975). Further, in 2D, the system has been shown to be integrable with a Lax pair, but only for a particular case, using the Tjon and Wright ansatz(Tjon and Wright, 1977). Nothing much is known about the solutions of LL equaiton in (3+1) dimensions. Developing even some particular solutions for LL equation, or for nonlinear σ-model for that matter, in higher dimensions would be of much fundamental interest.

Most of the solitonic structures associated with Heisenberg model or nonlinear σ-model (in one or two dimensions) have been all point-like configurations. When embedded in three dimensions, a point-like 2D soliton becomes a line vortex. For finite energy, its length must be finite which is possible if its core forms a *knot*. In 1975, L. Faddeev proposed that, knotted vortices could be constructed in a definite dynamical model(Faddeev, 1979). This model describes the (3+1) dimensional dynamics of a three-component vector $\mathbf{n}(\mathbf{x}, \tau)$ with unit length, $\mathbf{n} \cdot \mathbf{n} = 1$. As we have seen, such a vector field is a typical degree of freedom in the nonlinear σ-model and also is an order parameter in the Heisenberg model of ferromagnets(see equation (5.7)). The explicit solution conjectured in the above reference, had the shape of a doughnut; it is a closed torus-like vortex ring, twisted once around its core before joining the ends to ensure stability against shrinking. In knot theory this structure corresponds to the *unknot*, the simplest possible knot-like structure. In 1997, Faddeev and Niemi numerically showed that knot like structures indeed emerge as stable, finite-energy solutions in the model stated above(Faddeev and Niemi, 1997). They found strong evidence for the existence of the doughnut-shaped *unknot* vortex. In addition their results pointed strongly to the possibility of existence of a trefoil vortex; the simplest non-trivial knot. This general family of knots can be classified by counting how many times a knot winds a torus, both around and along the direction of the doughnut. Despite the relevance of knots to a large number of physical systems, its properties have not been much investigated. This largely due to the absence of theoretical means for generating stable knots in a nonlinear field theory. Battye and Sutcliffe extended Faddeev's work and showed the existence of solutions exhibiting rich and spectacular variety of phenomena including toroidal solitons with twists, linked loops and knots (for topological charges between one and eight)(Battye and Sutcliffe, 1998). These works used the following Lagrangian density:

$$\mathcal{L} = \partial_\mu \mathbf{n} \cdot \partial^\mu \mathbf{n} - \frac{1}{2}(\partial_\mu \mathbf{n} \times \partial_\nu \mathbf{n}) \cdot (\partial^\mu \mathbf{n} \times \partial^\nu \mathbf{n}), \tag{5.8}$$

where the field $\mathbf{n} \equiv (n_1, n_2, n_3)$ takes values on 2-sphere ($\mathbf{n}^2 = 1$), just like in Heisenberg model. The two parts of the Lagrangian are known as the sigma model term and the Skyrme term respectively. The second term is added to stabilize the soliton against scaling as in Derrick's theorem(Faddeev, 1979). This is an exciting albeit difficult territory of exploration in the analytical front regarding the Heisenberg ferromagnet and LL equation in (3+1) dimensions. Interestingly enough, isolated trefoil knots as well as pairs of linked vortex rings in water have been created in laboratory recently using a new method of accelerating specially shaped hydrofoils(Kleckner and Irvine, 2013).

Unlike the soliton solutions of the conservative LL system, dissipative solitons are localized excitations realized by a balance between non-linearity, dispersion, gain and loss in dissipative systems. If we allow STT to be like a gain mechanism which balances the damping loss we can conjecture the existence of *dissipative solitons* in nano ferromagnets. These are called 'magnetic droplet' solitons(Hoefer et al., 2010; Hoefer and Sommacal, 2012; Hoefer et al., 2012). The existence of magnetic droplet solitons has been vindicated by experiments using nanocontact based STNO very recently (Mohseni et al., 2013). Undoubtedly this is a new and exciting area of research closely related to the work presented in this thesis.

Again it becomes apparent that the phenomena associated with Landau-Lifshitz equation and spin transfer torques in nano ferromagnets are indeed plenty. This remains a fertile area both for fundamental and application oriented research. As we have pointed out in section 2.10, spintronics as a contemporary area of science and technology bridges the gap between fundamental research and technology follow up. So it is reasonable to expect that our modest contribution to this vast area of knowledge would indeed turn out to be a stepping stone towards more research and exciting results.

APPENDIX A

Derivation of the Slonczewski term in LLGS equation

We give a brief account of Slonczewski's derivation of the spin transfer torque term added to the LLG equation (equation (2.13)) based on his 1996 paper(Slonczewski, 1996). He assumed ballistic conditions and used WKB wave functions to predict the interesting fact that a transfer of vectorial spin accompanies an electric current flowing perpendicular to two parallel magnetic films connected by a normal metallic spacer.

Let's consider a five-layer structure consisting of the trilayer structure similar to figure (2.3) with two additional paramagnetic conductors as contacts. The magnetization vectors (global spin orientation per unit area) of the ferromagnetic layers are denoted by $\mathbf{S}_1$ (pinned) and $\mathbf{S}_2$ (free). The relation between these two vectors and the total angular momenta $\mathbf{L}_1$ and $\mathbf{L}_2$ in the two layers is given by:

$$\mathbf{L}_1 = \hbar \mathbf{S}_1 A_s, \mathbf{L}_2 = \hbar \mathbf{S}_2 A_s, \tag{A.1}$$

where $\hbar$ is the Plank's constant and A_s is the cross-sectional area of the thin film. A schematic of the metallic five layer structure is given in figure (A.1).

In figure (A.1), layers A, B, and C are paramagnetic, whereas F1 and F2 are ferromagnetic. Consider a flow of electrons moving rightward through the structure. F1 spin polarizes the electrons to some degree (remember there is no *pinning* considered here) along the instantaneous axis parallel to the vector $\mathbf{S}_1$. This leads us to consider a trilayer (B, F2, C) model in which electrons with initial spin state along $\mathbf{S}_1$ is incident from region B onto ferromagnet F2. Consider the moving frame $(\hat{\mathbf{x}}, \hat{\mathbf{y}}, \hat{\mathbf{z}})$ satisfying $\mathbf{S}_2 = S_2\, \hat{\mathbf{z}}$ and having the axis $\hat{\mathbf{y}}$ in the direction of $\mathbf{S}_2 \times \mathbf{S}_1$. This frame rotates as determined by the rotating vectors $\mathbf{S}_{1,2}$. Using $\hat{\mathbf{z}}$ as the spin quantization direction in this moving frame, the spin state of electron incident from region B is $(\cos(\theta/2), \sin(\theta/2))$.

The Coulomb plus Stoner exchange potential of the magnet has the locally diagonal values $V_{\pm}(\xi)$, where ξ is the position coordinate perpendicular to the pentalayer. The

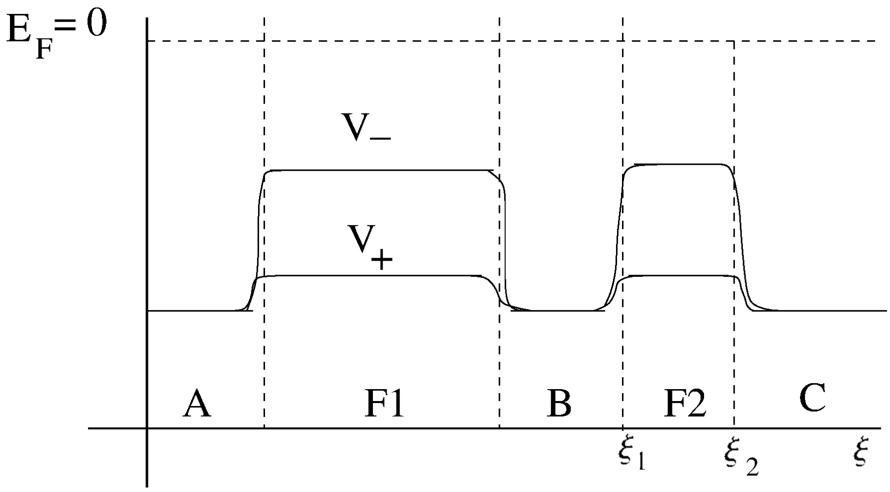

Figure A.1: Coulomb plus locally diagonalized exchange potential $V_\pm$ versus position ξ in five-layer system composed of paramagnets A, B, C, and ferromagnets F1 and F2(Slonczewski, 1996).

subscript $\pm$ corresponds to the majority/minority - spin electron band, respectively, introduced in the Chapter 1. Within WKB approximation, we define the ξ-component of the corresponding wave vectors $k_\pm(\xi)$. In units where ($\hbar^2/2$) divided by electron mass is taken as unity, the wave numbers are:

$$k_\pm = \left(E - k_p^2 - V_\pm\right)^{1/2}, \tag{A.2}$$

where E is the energy of the electron and k_p is the magnitude of the conserved component $\mathbf{k}_p$ of the wave vector normal to the axis ξ. Let F2 is between $\xi = \xi_1$ and ξ_2 and $\xi = 0$ be the center of region B so that we have the equality $V_+ = V_-$. We assume that $k_+ = k_-$ is real in paramagentic regions outside F2. The stationary WKB Hartree-Fock spinor wave function $\psi = (\psi_+, \psi_-)$ carrying unit particle flux is:

$$\begin{aligned}\psi(\xi) = \Bigg(& k_+^{-1/2}(\xi) \exp\left[i \int_0^\xi k_+(\xi')\, \mathrm{d}\xi'\right] cos\,(\theta/2), \\ & k_-^{-1/2}(\xi) \exp\left[i \int_0^\xi k_-(\xi')\, \mathrm{d}\xi'\right] sin\,(\theta/2)\Bigg),\end{aligned} \tag{A.3}$$

where $\xi \geq 0$.

The rightward particle flux Φ_e and the components of the rightward Pauli-spin flux $\mathbf{\Phi} \equiv (\Phi_x, \Phi_y, \Phi_z)$ defined as

$$\Phi_{e,z}(\xi) = Im\left(\psi_+^* \frac{\mathrm{d}\psi_+}{\mathrm{d}\xi} \pm \psi_-^* \frac{\mathrm{d}\psi_-}{\mathrm{d}\xi}\right), \tag{A.4}$$

$$\Phi_+(\xi) = \Phi_x + i\Phi_y = i\left(\frac{\mathrm{d}\psi_+^*}{\mathrm{d}\xi}\psi_- - \psi_+^* \frac{\mathrm{d}\psi_-}{\mathrm{d}\xi}\right) \tag{A.5}$$

satisfy general conditions of continuity. For the state (A.3), the Pauli-spin flux within regions B and C approaches:

$$\Phi_+ = \exp\left(i\int_0^\xi (k_- - k_+)\mathrm{d}\xi\right) sin\,\theta, \Phi_z = cos\,\theta. \tag{A.6}$$

These equations describe the conical precession of one-electron spin about $\mathbf{s}_2$ with the frequency governed by the exchange splitting $(V_- - V_+)$ while it traverse F2. Now we invoke the conservation of the angular momentum by stating that magnet *react* to the traversing of such an electron by acquiring a change in classical momentum $\Delta\mathbf{s}_2$ equal to the sum of the inward spin fluxes from both the sides of F2:

$$\begin{aligned} \Delta S_{2,x} + i\Delta S_{2,y} &= \left[\Phi_+(0) - \Phi_+(\infty)\right]/2 \\ &= \frac{1}{2}\left[1 - \exp\left(i\int_0^\infty (k_- - k_+)\,\mathrm{d}\xi\right)\right] sin\,\theta, \end{aligned} \tag{A.7}$$

$$\Delta S_{2,z} = 0. \tag{A.8}$$

The average spin transfer with respect to the direction of electron motion, and therefore that of $(k_+ - k_-)$, is according to equation (A.7):

$$\langle \Delta\mathbf{S} \rangle = (sin\,\theta, 0, 0)/2. \tag{A.9}$$

This is equivalent to the total absorption of the expectation value of the transverse component of spin ($\hat{\mathbf{x}}$) of the electron incident of F2. Now, if the Stoner splitting is so large as to eliminate the minority-spin electrons from the magnet or in the case where k_p is sufficiently large, then according to equation (A.2), k_- will be imaginary. That is, the component ψ_- completely reflects back to region B whereas ψ_+ completely transmits to region C. Consequently, the spin factor of the reflected wave is (0, sin θ/2) and that of the transmitted wave is ($\cos\theta/2$, 0). Since the matrix element given by equation (A.5) is off-diagonal, the scattering from F2 totally annihilates the transverse spin. Since the spin is conserved, this transverse spin is totally transferred to F2 without oscillations. But since the transmitted electron flux is $\cos^2(\theta/2)$, the spin-transfer *per transmitted electron* is:

$$\Delta\mathbf{S}_2 = \frac{sin\,\theta}{2cos^2\,(\theta/2)}\,(1,0,0) = (tan\,\theta/2)\,(1,0,0). \tag{A.10}$$

Equations (A.7, A.10) describe the complete transfer of the transverse component of incident electron-spin to the scattering ferromagnet.

Treatment of total electron flow through all the five regions in the figure (A.1) gives useful macroscopic expressions for current driven spin-transfer, including dynamical reactions of the ferromagnets F1 and F2. The paramagnets A and C are considered semi-infinite. The interiors of all the paramagnets have the parabolic energy-momentum expression $E = k_\pm^2 + k_p^2 - Q^2$, where Q is the magnitude of the Fermi vector **Q** and $E = 0$ is taken to be the Fermi level. Since, as seen in figure (A.1), $V_\pm$ only varies near the interfaces, we determine Q at the center $\xi = 0$ of region B. Since the ferromagnets are assumed to have similar band structure, we have $E = k_\pm^2 + k_p^2 - K_\pm^2$, where $K_\pm$ are similarly the magnitudes of $\mathbf{K}_\pm$, the internal Fermi vectors for majority/minority-spin electrons respectively. The calculations are very similar to what we have already described, but the algebra is quite lengthy. We refer the original Slonczewski's paper(Slonczewski, 1996) for the interested readers. Here we give the final result of such a calculation for the macro spin dynamics of both the ferromagnetic layers:

$$\dot{\mathbf{S}}_{1,2} = -\frac{GJ_e}{|e|}\mathbf{s}_{1,2} \times (\mathbf{s}_1 \times \mathbf{s}_2), \tag{A.11}$$

where $\mathbf{s}_1$ and $\mathbf{s}_2$ are the unit vectors along $\mathbf{S}_1$ and $\mathbf{S}_2$ respectively, e is the electron charge, and J_e is the electric current density, taken as positive when the electrons flow from the free layer into the fixed layer. The quantity G is given by the expression:

$$G = \left[-4 + (1+P)^3 \frac{(3 + \mathbf{s}_1 \cdot \mathbf{s}_2)}{P^{3/2}}\right]^{-1}, \tag{A.12}$$

where P is the degree of spin polarization. Typical values of P in ferromagnetic metals are $\sim$ 0.3—0.4 as mentioned in chapter 2. It is now just a matter of adding equation (A.11) to the LLG equation for the free layer to get a generalized LLG equation which can account for spin transfer effects in metallic trilayers. Slonczewski derived the following generalized LLG equation for the free layer magnetization dynamics:

$$\dot{\mathbf{S}}_2 = \mathbf{s}_2 \times \left(\gamma H_{an} (\mathbf{e}_x \cdot \mathbf{S}_2) \mathbf{e}_x - \alpha \dot{\mathbf{S}}_2 - \frac{G J_e}{|e|} (\mathbf{s}_1 \times \mathbf{s}_2) \right) , \qquad \text{(A.13)}$$

where H_{an} is the anisotropy field magnitude and $\mathbf{e}_x$ is the direction of in-plane anisotropy in the free layer. In appendix B we outline the steps involved in transforming equation (A.13) in the dimensionless form used in this thesis (equation (2.18)).

APPENDIX B

Derivation of the LLGS equation in the dimensionless form

As outlined in appnedix A, Slonczewski derived the following generalized LLG equation for the free layer magnetization dynamics subject to STT:

$$\dot{\mathbf{S}}_2 = \mathbf{s}_2 \times \left(\gamma H_{an}(\mathbf{e}_x \cdot \mathbf{S}_2)\mathbf{e}_x - \alpha\dot{\mathbf{S}}_2 - \frac{GJ_e}{|e|}(\mathbf{s}_1 \times \mathbf{s}_2)\right). \tag{B.1}$$

Here we very briefly show the procedure of converting equation (A.13) into the familiar form (equation (2.18)) we have used in this thesis. Equation (A.13) refers to a free layer subject to anisotropy effects. This can be generalized to the case of generic effective field $\mathbf{H}_{eff}$ by observing that the anisotropy field involved in equation (A.13) is $\mathbf{H}_{an} = -H_{an}(\mathbf{e}_x \cdot \mathbf{s}_2)\mathbf{e}_x$. The minus sign is due to the fact that the spin direction $\mathbf{s}_2$ is opposite to that of the magnetization. So in order to generalize equation (A.13), replace $-H_{an}(\mathbf{e}_x \cdot \mathbf{s}_2)\mathbf{e}_x$ with $\mathbf{H}_{eff} = \mathbf{H}_{exchange} + \mathbf{H}_{an} + \mathbf{H}_{demag} + \mathbf{H}_{ext}$ (equation (2.6)). This allows one to account for external fields and magnetostatic fields, both important for thin film magnets, in the generalized LLG equation. Now one can express equation (A.13) in terms of the average magnetization $\mathbf{M}$ in the free layer by using the relation between $\mathbf{S}_2$ and $\mathbf{M}$. The total magnetic moment of the free layer is equal to $-\gamma\hbar\mathbf{S}_2 A_s/\mu_0$, and its volume is $A_s d$, d being the free-layer thickness. Therefore:

$$\mathbf{M} = -\gamma\hbar\mathbf{S}_2/\mu_0 d. \tag{B.2}$$

Also since in our studies, the magnetization of F1 layer is fixed and we are only interested in the dynamical behaviour of the free layer. So we can as well define $\mathbf{s}_2 \equiv -\mathbf{m} = -\mathbf{M}/M_s$, where $\mathbf{m}$ is the unit vector along $\mathbf{M}$ and M_s is the saturation magnetization. Putting back these equation into (A.13) we have:

$$\dot{\mathbf{m}} = -\gamma M_s \mathbf{m} \times \left(\mathbf{h}_{eff} - \frac{\alpha}{\gamma M_s}\dot{\mathbf{m}} - \frac{GJ_e}{J_p}(\mathbf{e}_p \times \mathbf{m})\right), \tag{B.3}$$

where $\mathbf{h}_{eff} = \mathbf{H}_{eff}/M_s$, $\mathbf{e}_p \equiv -\mathbf{s}_1$ identifies the magnetization direction in the free layer, and the current density parameter J_p is:

$$J_p = \mu_0 M_s^2 \frac{|e|d}{\hbar}. \tag{B.4}$$

Finally, we do the time rescaling; $t \to \gamma M_s t$ implying time measured in picoseconds as shown in Chapter 2. Making use of equation (A.12) in equation (B.3) we get the dimensionless form of the LLGS equation as given in Chapter 2 and Chapter 3(refer (2.18)):

$$\frac{\partial \mathbf{m}}{\partial t} - \alpha \mathbf{m} \times \frac{\partial \mathbf{m}}{\partial t} = \mathbf{m} \times \left(\mathbf{h}_{eff} - \beta \frac{\mathbf{m} \times \mathbf{e}_p}{1 + c_p \mathbf{m} \cdot \mathbf{e}_p} \right), \tag{B.5}$$

where the new parameters are defined as follows:

$$\beta = b_p \frac{J_e}{J_p}, \tag{B.6}$$

$$b_p = \frac{4P^{3/2}}{3(1+P)^3 - 16P^{3/2}}, \tag{B.7}$$

$$c_p = \frac{(1+P)^3}{3(1+P)^3 - 16P^{3/2}}. \tag{B.8}$$

REFERENCES

1. Acremann, Y., Strachan, J. P., Chembrolu, V., Andrews, S. D., Tyliszczak, T., Katine, J. A., Carey, M. J., Clemens, B. M., Siegmann, H. C., and Stöhr, J. (2006). Time-resolved imaging of spin transfer switching: Beyond the macrospin concept. *Phys. Rev. Lett.*, *96*, 217202.

2. Albert, F. J., Emley, N. C., Myers, E. B., Ralph, D. C., and Buhrman, R. A. (2002). Quantitative study of magnetization reversal by spin-polarized current in magnetic multilayer nanopillars. *Phys. Rev. Lett.*, *89*, 226802.

3. Albert, F. J., Katine, J. A., Buhrman, R. A., and Ralph, D. C. (2000). Spin-polarized current switching of a co thin film nanomagnet. *Applied Physics Letters*, *77*, 3809–3811.

4. Baibich, M. N., Broto, J. M., Fert, A., Van Dau, F. N., Petroff, F., Etienne, P., Creuzet, G., Friederich, A., and Chazelas, J. (1988). Giant magnetoresistance of (001)fe/(001)cr magnetic superlattices. *Phys. Rev. Lett.*, *61*, 2472–2475.

5. Bass, J., and Jr., W. P. (1999). Current-perpendicular (cpp) magnetoresistance in magnetic metallic multilayers. *Journal of Magnetism and Magnetic Materials*, *200*, 274 – 289.

6. Battye, R. A., and Sutcliffe, P. M. (1998). Knots as stable soliton solutions in a three-dimensional classical field theory. *Phys. Rev. Lett.*, *81*, 4798–4801.

7. Bazaliy, Y., Jones, B., and Zhang, S.-C. (2004). Current-induced magnetization switching in small domains of different anisotropies. *Physical Review B*, *69*, 094421.

8. Belavin, A., and Polyakov, A. M. (1975). Metastable states of two-dimensional isotropic ferromagnets. *JETP Letters*, *22*, 245.

9. Berger, L. (1996). Emission of spin waves by a magentic multilayer traversed by a current. *Physical Review B*, *54*, 9353–9358.

10. Berger, L. (2001). Effect of interfaces on Gilbert damping and ferromagnetic resonance linewidth in magnetic multilayers. *Journal of Applied Physics*, *90*, 4632.

11. Berkov, D., and Miltat, J. (2008). Spin-torque driven magnetization dynamics: Micromagnetic modeling. *Journal of Magnetism and Magnetic Materials*, *320*, 1238 – 1259.

12. Bertotti, G., Mayergoyz, I., and Serpico, C. (2009). *Nonlinear Magnetization Dynamics in Nanosystems*. Elsevier, UK.

13. Bertotti, G., Serpico, C., Mayergoyz, I. D., Magni, A., d'Aquino, M., and Bonin, R. (2005). Magnetization switching and microwave oscillations in nanomagnets driven by spin-polarized currents. *Phys. Rev. Lett.*, *94*, 127206.

14. Binasch, G., Grünberg, P., Saurenbach, F., and Zinn, W. (1989). Enhanced magnetoresistance in layered magnetic structures with antiferromagnetic interlayer exchange. *Phys. Rev. B*, *39*, 4828–4830.

15. Bonin, R., Bertotti, G., Bortolotti, P., Serpico, C., D'Aquino, M., and Mayergoyz, I. D. (2010). Analytical study of synchronization in spin-transfer-driven magnetization dynamics. *J. Phys.: Conf. Ser.*, *200*, 042005.

16. Braganca, P. M., Krivorotov, I. N., Ozatay, O., Garcia, a. G. F., Emley, N. C., Sankey, J. C., Ralph, D. C., and Buhrman, R. a. (2005). Reducing the critical current for short-pulse spin-transfer switching of nanomagnets. *Applied Physics Letters*, *87*, 112507.

17. Caputo, J.-G., Gaididei, Y., Mertens, F. G., and Sheka, D. D. (2007). Vortex polarity switching by a spin-polarized current. *Phys. Rev. Lett.*, *98*, 056604.

18. Chappert, C., Fert, A., and Van Dau, F. N. (2007). The emergence of spin electronics in data storage. *Nature materials*, *6*, 813–23.

19. Chen, X., and Victora, R. (2009). Phase locking of spin-torque oscillators by spin-wave interactions. *Physical Review B*, *79*, 180402.

20. Cros, V., Boulle, O., Grollier, J., Hamzić, A., Muñoz, M., Pereira, L. G., and Petroff, F. (2005). Spin Transfer Torque: a new method to excite or reverse a magnetization. *Comptes Rendus Physique*, *6*, 956–965.

21. Daughton, J. M. (1997). Magnetic tunneling applied to memory (invited). *Journal of Applied Physics*, *81*, 3758.

22. Dery, H., Dalal, P., Cywiński, Ł., and Sham, L. J. (2007). Spin-based logic in semiconductors for reconfigurable large-scale circuits. *Nature*, *447*, 573–6.

23. Dieny, B., Sousa, R. C., Herault, J., Papusoi, C., Prenat, G., Ebels, U., Houssameddine, D., Rodmacq, B., Auffret, S., Buda-Prejbeanu, L. D., Cyrille, M. C., Delaet, B., Redon, O., Ducruet, C., Nozieres, J. P., and Prejbeanu, I. L. (2010). Spin-transfer effect and its use in spintronic components. *International Journal of Nanotechnology*, *7*, 591–614.

24. Donahue, M. J., and Porter, D. G. (Sept 1999). *OOMMF User's Guide, Version 1.0, Interagency Report NISTIR 6376*. Technical Report National Institute of Standards and Technology, Gaithersburg, MD. Available at `http://math.nist.gov/oommf`.

25. Dussaux, a., Khvalkovskiy, a. V., Grollier, J., Cros, V., Fukushima, a., Konoto, M., Kubota, H., Yakushiji, K., Yuasa, S., Ando, K., and Fert, a. (2011). Phase locking of vortex based spin transfer oscillators to a microwave current. *Applied Physics Letters*, *98*, 132506.

26. Engel, B. N., Akerman, J., Butcher, B., Dave, R., DeHerrera, M., Durlam, M., Grynkewich, G., Janesky, J., Pietambaram, S., Rizzo, N., Slaughter, J., Smith, K., Sun, J. J., and Tehrani, S. (2005). A 4-mb toggle mram based on a novel bit and switching method. *IEEE Transactions on Magnetics*, *41*, 132–136.

27. Faddeev, L. (1979). In M. Pantaleo, and F. De Finis (Eds.), *Relativity, Quanta and Cosmology* (pp. 185–192). Johnson Reprint Corp.

28. Faddeev, L., and Niemi, A. J. (1997). Stable knot-like structures in classical field theory. *Nature*, *387*, 58–61.

29. Farmer, J. D. (1982). Chaotic attractors of an infinite-dimensional dynamical system. *Physica D: Nonlinear Phenomena*, *4*, 366 – 393.

30. Fischbacher, T., Franchin, M., Bordignon, G., and Fangohr, H. (2007). A systematic approach to multiphysics extensions of finite-element-based micromagnetic simulations: Nmag. *Magnetics, IEEE Transactions on*, *43*, 2896–2898.

31. Georges, B., Grollier, J., Cros, V., and Fert, a. (2008). Impact of the electrical connection of spin transfer nano-oscillators on their synchronization: an analytical study. *Applied Physics Letters*, *92*, 232504.

32. Gilbert, T. (2004). Classics in Magnetics A Phenomenological Theory of Damping in Ferromagnetic Materials. *IEEE Transactions on Magnetics*, *40*, 3443–3449.

33. Grollier, J., Boulenc, P., Cros, V., Hamzi?, A., Vaurès, A., Fert, A., and Faini, G. (2003). Switching a spin valve back and forth by current-induced domain wall motion. *Applied Physics Letters*, *83*, 509–511.

34. Grollier, J., Cros, V., and Fert, a. (2006). Synchronization of spin-transfer oscillators driven by stimulated microwave currents. *Physical Review B*, *73*, 060409.

35. Grollier, J., Cros, V., Hamzic, A., George, J. M., Jaffrès, H., Fert, A., Faini, G., Ben Youssef, J., and Legall, H. (2001). Spin-polarized current induced switching in co/cu/co pillars. *Applied Physics Letters*, *78*, 3663–3665.

36. Grollier, J., Lacour, D., Cros, V., Hamzic, A., Vaurès, A., Fert, A., Adam, D., and Faini, G. (2002). Switching the magnetic configuration of a spin valve by current-induced domain wall motion. *Journal of Applied Physics*, *92*, 4825–4827.

37. Hassoun, M. M., Black, W. C., Lee, E. K. F., Geiger, R. L., and Hurst, A. (1997). Field Programmable Logic Gates Using GMR Devices. *IEEE Transactions on Magnetics*, *33*, 3307–3309.

38. Hayashi, M., Thomas, L., Rettner, C., Moriya, R., Bazaliy, Y. B., and Parkin, S. S. P. (2007). Current driven domain wall velocities exceeding the spin angular momentum transfer rate in permalloy nanowires. *Phys. Rev. Lett.*, *98*, 037204.

39. Hoefer, M., and Sommacal, M. (2012). Propagating two-dimensional magnetic droplets. *Physica D: Nonlinear Phenomena*, *241*, 890 – 901.

40. Hoefer, M. A., Silva, T. J., and Keller, M. W. (2010). Theory for a dissipative droplet soliton excited by a spin torque nanocontact. *Phys. Rev. B*, *82*, 054432.

41. Hoefer, M. A., Sommacal, M., and Silva, T. J. (2012). Propagation and control of nanoscale magnetic-droplet solitons. *Phys. Rev. B*, *85*, 214433.

42. Huber, D. L. (1982). Dynamics of spin vortices in two-dimensional planar magnets. *Phys. Rev. B, 26,* 3758–3765.

43. Jones, R. O., and Gunnarsson, O. (1989). The density functional formalism, its applications and prospects. *Rev. Mod. Phys., 61,* 689–746.

44. Kaka, S., Pufall, M. R., Rippard, W. H., Silva, T. J., Russek, S. E., and Katine, J. a. (2005). Mutual phase-locking of microwave spin torque nano-oscillators. *Nature, 437,* 389–92.

45. Kalitsov, A., Chshiev, M., Theodonis, I., Kioussis, N., and Butler, W. H. (2009). Spin-transfer torque in magnetic tunnel junctions. *Phys. Rev. B, 79,* 174416.

46. Kiselev, S. I., Sankey, J. C., Krivorotov, I. N., Emley, N. C., Schoelkopf, R. J., Buhrman, R. a., and Ralph, D. C. (2003). Microwave oscillations of a nanomagnet driven by a spin-polarized current. *Nature, 425,* 380–3.

47. Kläui, M., Vaz, C. A. F., Bland, J. A. C., Wernsdorfer, W., Faini, G., Cambril, E., and Heyderman, L. J. (2003). Domain wall motion induced by spin polarized currents in ferromagnetic ring structures. *Applied Physics Letters, 83,* 105–107.

48. Kleckner, D., and Irvine, W. T. M. (2013). Creation and dynamics of knotted vortices. *Nature Physics, 9,* 253 – 258.

49. Krivorotov, I. N., Emley, N. C., Garcia, A. G. F., Sankey, J. C., Kiselev, S. I., Ralph, D. C., and Buhrman, R. A. (2004). Temperature dependence of spin-transfer-induced switching of nanomagnets. *Phys. Rev. Lett., 93,* 166603.

50. Lakshmanan, M. (1977). Continuum spin system as an exactly solvable dynamical system. *Physics Letters A, 61,* 53 – 54.

51. Lakshmanan, M., and Senthilkumar, D. V. (2010). *Dynamics of Nonlinear Time-Delay Systems*. Springer-Verlag, Berlin.

52. Landau, L., and Lifshitz, E. (1935). On the theory of the dispersion of magnetic permeability in ferromagnetic bodies. *Physik. Zeits. Sowjetunion, 8,* 153–169.

53. Lee, K.-J., and Dieny, B. (2006). Micromagnetic investigation of the dynamics of magnetization switching induced by a spin polarized current. *Applied Physics Letters*, *88*, 132506.

54. Lee, S., Choa, S., Member, S., and Lee, S. (2007). Magneto-Logic Device Based on a Single-Layer Magnetic Tunnel Junction. *IEEE Transactions on Electron Devices*, *54*, 2040–2044.

55. Li, D., Zhou, Y., Hu, B., Å kerman, J., and Zhou, C. (2012). Multiple synchronization attractors of serially connected spin-torque nanooscillators. *Physical Review B*, *86*, 014418.

56. Li, Z., Li, Y. C., and Zhang, S. (2006). Dynamic magnetization states of a spin valve in the presence of dc and ac currents: Synchronization, modification, and chaos. *Phys. Rev. B*, *74*, 054417.

57. Li, Z., and Zhang, S. (2003). Magnetization dynamics with a spin-transfer torque. *Phys. Rev. B*, *68*, 024404.

58. Liu, Y., Zhang, Z., Wang, J., Freitas, P. P., and Martins, J. L. (2003). Current-induced switching in low resistance magnetic tunnel junctions. *Journal of Applied Physics*, *93*, 8385–8387.

59. Mancoff, F. B., Rizzo, N. D., Engel, B. N., and Tehrani, S. (2005). Phase-locking in double-point-contact spin-transfer devices. *Nature*, *437*, 393–5.

60. Mangin, S., Ravelosona, D., Katine, J. a., Carey, M. J., Terris, B. D., and Fullerton, E. E. (2006). Current-induced magnetization reversal in nanopillars with perpendicular anisotropy. *Nature Materials*, *5*, 210–215.

61. Mistral, Q., van Kampen, M., Hrkac, G., Kim, J.-V., Devolder, T., Crozat, P., Chappert, C., Lagae, L., and Schrefl, T. (2008). Current-driven vortex oscillations in metallic nanocontacts. *Phys. Rev. Lett.*, *100*, 257201.

62. Mohseni, S. M., Sani, S. R., Persson, J., Nguyen, T. N. A., Chung, S., Pogoryelov, Y., Muduli, P. K., Iacocca, E., Eklund, A., Dumas, R. K., Bonetti, S., Deac, A., Hoefer, M. A., and Åkerman, J. (2013). Spin torque?generated magnetic droplet solitons. *Science*, *339*, 1295–1298.

63. Moodera, J. S., Kinder, L. R., Wong, T. M., and Meservey, R. (1995). Large magnetoresistance at room temperature in ferromagnetic thin film tunnel junctions. *Phys. Rev. Lett.*, *74*, 3273–3276.

64. Moodera, J. S., Nowak, J., and van de Veerdonk, R. J. M. (1998). Interface magnetism and spin wave scattering in ferromagnet-insulator-ferromagnet tunnel junctions. *Phys. Rev. Lett.*, *80*, 2941–2944.

65. Moore, G. E. (1965). Cramming more components onto integrated circuits. *Electronics*, *38*, 114–117.

66. Murugesh, S., and Lakshmanan, M. (2009). Spin-transfer torque induced reversal in magnetic domains. *Chaos, Solitons & Fractals*, *41*, 2773–2781.

67. Myers, E. B., Ralph, D. C., Katine, J. A., Louie, R. N., and Buhrman, R. A. (1999). Current-induced switching of domains in magnetic multilayer devices. *Science*, *285*, 867–870.

68. Ney, A., and Harris, J. S. (2005). Reconfigurable magnetologic computing using the spin flop switching of a magnetic random access memory cell. *Applied Physics Letters*, *86*, 013502.

69. Ney, A., Pampuch, C., Koch, R., and Ploog, K. H. (2003). Programmable computing with a single magnetoresistive element. *Nature*, *425*, 485–487.

70. Parkin, S., Jiang, X., Kaiser, C., Panchula, A., Roche, K., and Samant, M. (2003). Magnetically engineered spintronic sensors and memory. *Proceedings of the IEEE*, *91*, 661–680.

71. Parkin, S. S. P., Hayashi, M., and Thomas, L. (2008). Magnetic domain-wall racetrack memory. *Science*, *320*, 190–194.

72. Parkin, S. S. P., Kaiser, C., Panchula, A., Rice, P. M., Hughes, B., Samant, M., and Yang, S.-H. (2004). Giant tunnelling magnetoresistance at room temperature with MgO (100) tunnel barriers. *Nature materials*, *3*, 862–7.

73. Persson, J., Zhou, Y., and Akerman, J. (2007). Phase-locked spin torque oscillators: Impact of device variability and time delay. *Journal of Applied Physics*, *101*, 09A503.

74. Pizzini, S., Uhlíř, V., Vogel, J., Rougemaille, N., Laribi, S., Cros, V., Jiménez, E., Camarero, J., Tieg, C., Bonet, E., Bonfim, M., Mattana, R., Deranlot, C., Petroff, F., Ulysse, C., Faini, G., and Fert, A. (2009). High domain wall velocity at zero magnetic field induced by low current densities in spin valve nanostripes. *Applied Physics Express*, *2*, 023003.

75. Pribiag, V. S., Krivorotov, I. N., Fuchs, G. D., Braganca, P. M., Ozatay, O., Sankey, J. C., Ralph, D. C., and Buhrman, R. a. (2007). Magnetic vortex oscillator driven by d.c. spin-polarized current. *Nature Physics*, *3*, 498–503.

76. Pufall, M. R., Rippard, W. H., Russek, S. E., Kaka, S., and Katine, J. A. (2006). Electrical measurement of spin-wave interactions of proximate spin transfer nanooscillators. *Phys. Rev. Lett.*, *97*, 087206.

77. Rajaraman, R. (1987). *An Introduction to Solitons and Instantons in Quantum Field Theory*. Elesevier, Amsterdam.

78. Ralph, D., and Stiles, M. (2008). Spin transfer torques. *Journal of Magnetism and Magnetic Materials*, *320*, 1190–1216.

79. Rezende, S., de Aguiar, F., Rodríguez-Suárez, R., and Azevedo, a. (2007). Mode Locking of Spin Waves Excited by Direct Currents in Microwave Nano-oscillators. *Physical Review Letters, 98,* 087202.

80. Richter, R., Boeve, H., Bär, L., Bangert, J., Rupp, G., Reiss, G., and Wecker, J. (2002). Field programmable spin-logic realized with tunnelling-magnetoresistance devices. *Solid-State Electronics*, *46*, 639–643.

81. Rippard, W., Pufall, M., Kaka, S., Russek, S., and Silva, T. (2004). Direct-Current Induced Dynamics in Co90Fe10/Ni80Fe20 Point Contacts. *Physical Review Letters*, *92*, 027201.

82. Rippard, W., Pufall, M., Kaka, S., Silva, T., Russek, S., and Katine, J. (2005). Injection Locking and Phase Control of Spin Transfer Nano-oscillators. *Physical Review Letters*, *95*, 067203.

83. Sanid, C., and Murugesh, S. (2012). Spin-Transfer-Torque Driven Magneto-Logic Gates Using Nano Spin-Valve Pillars. *Japanese Journal of Applied Physics*, *51*, 063001.

84. Sanid, C., and Murugesh, S. (2013). Spin-Transfer-Torque driven magneto-logic OR, AND and NOT gates. *The European Physical Journal Special Topics*, *222*, 711–719.

85. Sanid, C., and Murugesh, S. (2014). Synchronization and chaos in spin-transfer-torque nano-oscillators coupled via a high-speed operational amplifier. *Journal of Physics D: Applied Physics*, *47*, 065005.

86. Shibata, J., Nakatani, Y., Tatara, G., Kohno, H., and Otani, Y. (2006). Current-induced magnetic vortex motion by spin-transfer torque. *Phys. Rev. B*, *73*, 020403.

87. Shibata, J., Nakatani, Y., Tatara, G., Kohno, H., and Otani, Y. (2007). Magnetic vortex dynamics induced by spin-transfer torque. *Journal of Magnetism and Magnetic Materials*, *310*, 2041 – 2042. Proceedings of the 17th International Conference on Magnetism The International Conference on Magnetism.

88. Shinjo, T., Okuno, T., Hassdorf, R., Shigeto, . K., and Ono, T. (2000). Magnetic vortex core observation in circular dots of permalloy. *Science*, *289*, 930–932.

89. Slonczewski, J. (1996). Current-driven excitation of magnetic multilayers. *Journal of Magnetism and Magnetic Materials*, *159*, L1–L7.

90. Slonczewski, J. (1999). Excitation of spin waves by an electric current. *Journal of Magnetism and Magnetic Materials*, *195*, L261–L268.

91. Stiles, M., and Miltat, J. (2006). Spin-transfer torque and dynamics. In B. Hillebrands, and A. Thiaville (Eds.), *Spin Dynamics in Confined Magnetic Structures III* (pp. 225–308). Springer Berlin Heidelberg volume 101 of *Topics in Applied Physics*.

92. Subash, B., Chandrasekar, V. K., and Lakshmanan, M. (2013). Synchronization of an array of spin torque nano oscillators in periodic applied external magnetic field. *EPL (Europhysics Letters)*, *102*, 17010.

93. Takhtajan, L. A. (1977). Integration of the continuous Heisenberg spin chain through the inverse scattering method. *Physics Letters A*, *64*, 235 – 237.

94. Thiaville, A., Nakatani, Y., Miltat, J., and Vernier, N. (2004). Domain wall motion by spin-polarized current: a micromagnetic study. *Journal of Applied Physics*, *95*, 7049–7051.

95. Thiele, A. A. (1973). Steady-state motion of magnetic domains. *Phys. Rev. Lett., 30*, 230–233.

96. Tiberkevich, V., Slavin, A., Bankowski, E., and Gerhart, G. (2009). Phase-locking and frustration in an array of nonlinear spin-torque nano-oscillators. *Applied Physics Letters*, *95*, 262505.

97. Tjon, J., and Wright, J. (1977). Solitons in the continuous Heisenberg spin chain. *Phys. Rev. B*, *15*, 3470–3476.

98. Urazhdin, S., Tabor, P., Tiberkevich, V., and Slavin, A. (2010). Fractional Synchronization of Spin-Torque Nano-Oscillators. *Physical Review Letters*, *105*, 104101.

99. Vouille, C., Barthélémy, A., Elokan Mpondo, F., Fert, A., Schroeder, P. A., Hsu, S. Y., Reilly, A., and Loloee, R. (1999). Microscopic mechanisms of giant magnetoresistance. *Phys. Rev. B, 60*, 6710–6722.

100. Wachowiak, A., Wiebe, J., Bode, M., Pietzsch, O., Morgenstern, M., and Wiesendanger, R. (2002). Direct observation of internal spin structure of magnetic vortex cores. *Science, 298*, 577–580.

101. Wang, J., Meng, H., and Wang, J.-P. (2005). Programmable spintronics logic device based on a magnetic tunnel junction element. *Journal of Applied Physics, 97*, 10D509.

102. Wolf, A., Swift, J. B., Swinney, H. L., and Vastano, J. A. (1985). DETERMINING LYAPUNOV EXPONENTS FROM A TIME SERIES. *Physica*, *16D*, 285–317.

103. Wolf, S., Chtchelkanova, A. Y., and Treger, D. (2006). Spintronics—a retrospective and perspective. *IBM Journal of Research and Development*, *50*, 101–110.

104. Yuasa, S., Nagahama, T., Fukushima, A., Suzuki, Y., and Ando, K. (2004). Giant room-temperature magnetoresistance in single-crystal Fe/MgO/Fe magnetic tunnel junctions. *Nature materials*, *3*, 868–71.

105. Zhang, S., and Li, Z. (2004). Roles of nonequilibrium conduction electrons on the magnetization dynamics of ferromagnets. *Phys. Rev. Lett., 93*, 127204.

106. Zhao, W., Member, S., Belhaire, E., and Chappert, C. (2007). Spin-MTJ based Non-Volatile Flip-Flop. In *7th IEEE International Conference on Nanotechnology* (pp. 399–402).

107. Zhou, Y., Bonetti, S., Persson, J., and Å kerman, J. (2009). Capacitance Enhanced Synchronization of Pairs of Spin-Transfer Oscillators. *IEEE Transactions on Magnetics, 45*, 2421–2423.

LIST OF PAPERS BASED ON THESIS

Papers in Refereed International Journals

1. Synchronization and chaos in spin-transfer-torque nano-oscillators coupled via a high speed operational amplifier
   C Sanid and S Murugesh
   Journal of Physics D: Applied Physics, **47**, 065005 (2014)

2. Spin-Transfer-Torque driven magneto-logic OR, AND and NOT gates
   C Sanid and S Murugesh
   The European Physical Journal Special Topics, **222**, 711 (2013)

3. Spin-Transfer-Torque Driven Magneto-Logic Gates Using Nano Spin-Valve Pillars
   C Sanid and S Murugesh
   Japanese Journal of Applied Physics, **51**, 063001 (2012)

Presentations in Conferences

1. Presented a poster titled *Spin-transfer torque driven magneto-logic gates using spin-valve pillars* at the **International School on Non-linear Dynamics in Complex Systems** at Yaoundè, Cameroon on November 01, 2011.

2. Presented a poster titled *Dynamical regions in coupled spin torque nano oscillators: A drive-response system using a high speed Op Amp* at the **Perspectives in Nonlinear Dynamics (PNLD-2013), A satellite to STATPHYS-25, Korea** at Hyderabad on July 16, 2013.

3. Presented a poster titled *Theory and design of spin-transfer-torque driven universal and non-universal magneto-logic gates* at the **International Conference on Magnetic Materials and Applications(MagMA-2013)** at Guwahati on December 06, 2013.

4. Presented a paper titled *Augmenting microwave power through electrically coupling spin-torque nano-oscillators: Synchronization in a master-slave model* at the **NMI Workshop on Nonlinear Integrable Systems and their Applications** at Tiruchirappalli on February 25, 2014.